Theory of spin-orbit interactions in electronic transport and light scattering at the mesoscale

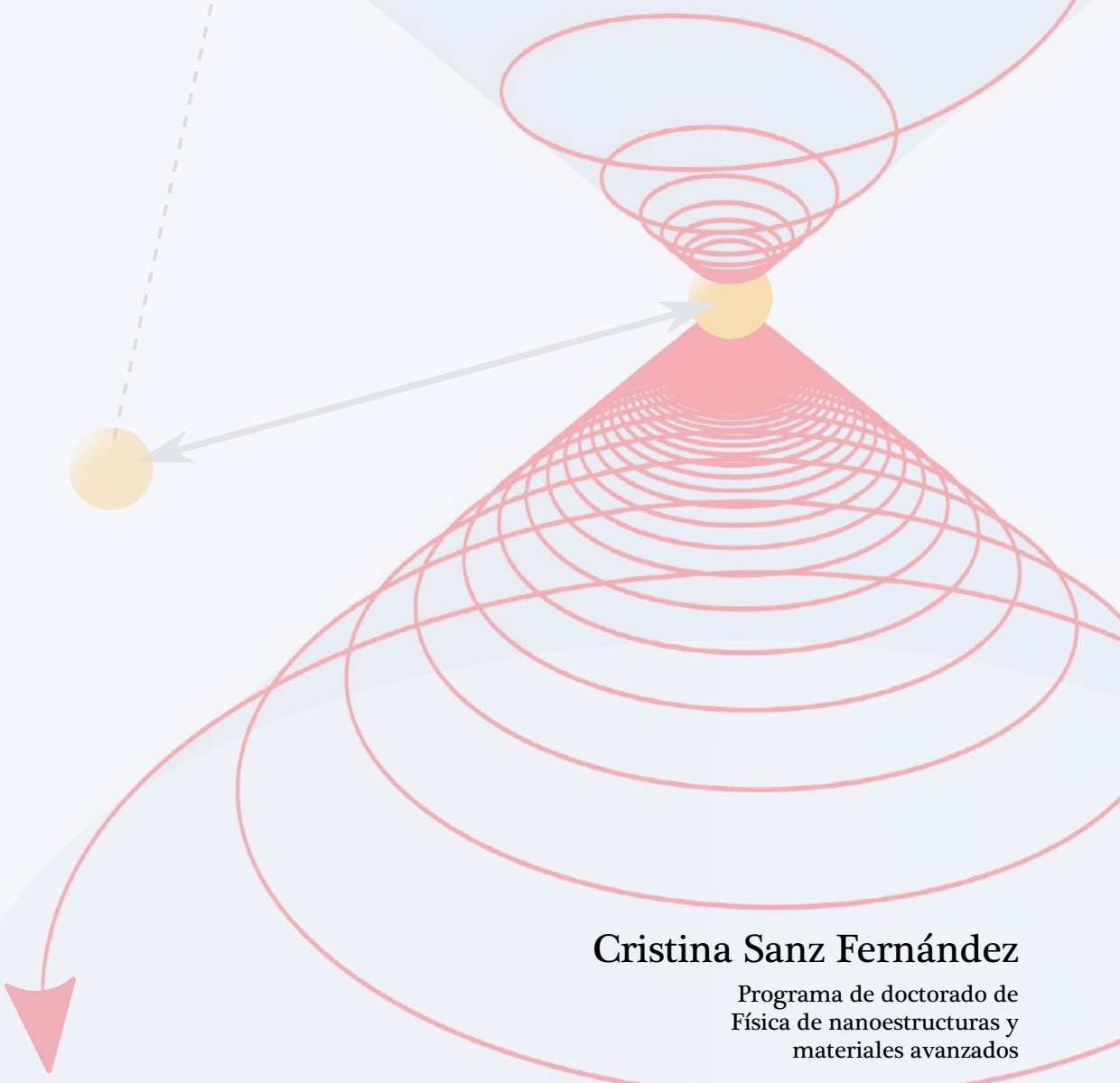

Cristina Sanz Fernández

Programa de doctorado de
Física de nanoestructuras y
materiales avanzados

eman ta zabal zazu
Universidad del País Vasco
Euskal Herriko Unibertsitatea

NAZIOARTEKO BIKAINTASUN CAMPUSA
CAMPUS DE EXCELENCIA INTERNACIONAL

CFM Materialen Fisika Zentroa
Centro de Física de Materiales
Materials Physics Center

Theory of spin-orbit interactions in electronic transport and light scattering at the mesoscale

Cristina Sanz Fernández

Supervised by Dr. F. Sebastián Bergeret and Prof. Juan José Sáenz

January 2021

A Mole.

Agradecimientos

We'll be washed and buried one day my girl,
and the time we were given will be left for the world.
The flesh that lived and loved will be eaten by plague,
so let the memories be good for those who stay.

Cuanto más escucho esta estrofa, más pienso que tú lo conseguiste Mole, nos dejaste a todos llenos de buenos recuerdos. Ya empiezo llorando. Desde el primer día que nos diste clase en la Autónoma sabíamos que no nos ibas a dejar indiferentes: un catedrático que parecía un bajista de Rosendo y que, a diferencia de muchos otros profesores, nos trataba como iguales, sin darse ínfulas. Tu obsesión por la física, de científico de verdad, de los que emocionan, fue la que nos llevó a hacer el doctorado y la que durante estos años nos siguió emocionando. Aunque es cierto que esa pasión, que te llevaba a estar semanas enfrascado en algo sin apenas hacernos caso a Jorge y a mí, ni a nadie, también nos llevó a veces por la calle de la amargura. Siento una infinita tristeza al pensar que nos dejaste. La ilusión que ponías cuando te hablaba de empezar a escribir la tesis me ha dado fuerzas para hacerlo, aunque te reconozco que ha sido difícil. Siento que me faltaba muchísimo aún por aprender contigo, y es que eras jodidamente inteligente, tanto en física como en la vida. Te quería mucho y llegaste a nuestras vidas, de Jorge y mía, para quedarte. Tranquilo, seguirás estando siempre con nosotros, porque no te olvidaremos nunca. Como tanto usabas tú, qué hijoputa fuiste al dejarnos. Y es que va a ser verdad eso de que siempre se van los mejores.

Gracias a Mole también tuvimos la oportunidad de conocer gente buena con la que currar, tanto en física como en la "penúltima". Manuel, Luis, José, Antonio y Aitzol, entre otros. Nuno, gigante amigo, de tamaño y de corazón. Nunca olvidaré lo que me has ayudado estos meses, de verdad. Desde el primer momento en el que nos quedamos sin Mole, no dudaste en llamarnos y ofrecernos toda tu ayuda. Obrigado. Y Diego, inquilino eterno. Tu "abrumadora" empatía nos pone los pies en la tierra. Espero seguir aprendiendo de ella muchos años más.

También gracias a Mole comenzó nuestra etapa en Donosti. El mismito primer día que llegamos nos llevó de pintxo-pote con la increíble, la maravillosa, Chiki. Gracias por todo Chiki. Siempre nos has hecho sentir como en casa, nos has cuidado, sobretodo con tu exquisita cocina (aunque a veces picara nada, un poquitín), y nos has hecho reír como ninguna. Eres una mujer increíble, definición de buena gente y un referente para mí, alejada de estereotipos y con las ideas muy claras. Qué suerte tenéis Carlos y Edurne. Habéis heredado esa cercanía infinita de vuestros padres. Edurne, eres una máquina, tendremos suerte si decides dedicarte a la ciencia.

En Donosti, la primera parada fue el DIPC. Gracias a sus contratos predoctorales pudimos tener sueldo hasta conseguir una beca. Qué pena que en lo público no se puedan dar esas oportunidades y muchos desistan de seguir en ciencia y otros tengan que currar gratis los primeros meses. Gracias a "los del DIPC" por acogernos y sacarnos de sidras, sobretodo al principio, y hacernos la vida en Donosti más fácil. Miri e Irene, sois maravillosas, cualquiera que os tenga cerca es afortunado/a, us trobo a faltar petita i gran amiga. Ion, titán, super hombre. Debajo de esa fachada, eres un tío increíble, sincero como nadie y más bueno que el pan. Sí, sí, que el pan. Mi amigo navarro. Sof, no sé qué sería de mí sin ti, estás a la altura de la sidra. De verdad, gracias por tanto amiga. Estuvisteis conmigo, a mi ladito, siempre, en lo bueno y en lo menos bueno. Ojalá tener siempre un cartel de "Aquí duerme Cris". Os quiero mucho bikote, incluso más que a las patatas.

Pasé después al CFM con beca, para comenzar el proyecto que hoy en día es mi tesis con la ayuda de Sebas, además de Mole. Gracias Sebas por la oportunidad que me diste. Gracias por todos los consejos que me has ido dando estos años de cara a un futuro en ciencia. Creo haber aprendido a moverme mejor en este mundo, sobretodo en las partes menos utópicas. Has intentado hacer de mí una científica con todas las letras. Aún alguna me falta. Además de las muchas horas y esfuerzo puestos en pedir proyectos y demás burocracia, has sido un jefe de grupo con tiempo para todos nosotros y nosotras, gracias. También gracias por la oportunidad de colaborar con otros científicos. Entre ellos querría destacar a Fèlix Casanova, Juan Borge e Ilya Tokatly. Fèlix, gracias por atender a mis preguntas siempre y darme ese toque de realidad experimental que todo teórico necesita. Juan, poder hablar de tú a tú con alguien y sin miedo a fallar o decir alguna tontería me ayudó mucho en nuestros papers, gracias. And Ilya, it was always surprising for me how you make Physics look easy. Thank you for the opportunity to work and learn with you.

I would also like to take this opportunity to thank Vitaly Golovach for his help at the beginning of my PhD. My work behind Section 1.3, the original motivation of this thesis, was partly thanks to your help. Thank you too, of course, for your assistance in my last month as a PhD student.

Y ahora voy a "los del CFM". Fer, bruto en apariencia, pero con una sensibilidad que envidiar. Carmen, desde el principio me hiciste sentir como parte de un grupo, gracias. Ese toque gaditano nos deja a todos locos. Marina, maja, hermosa, vale(mo)s un montón, que nadie te(nos) haga pensar lo contrario. Miguel, pero qué taconazos. Quién pudiera andar así de bien, sobretodo con la cabeza bien alta, como tú. Martín, compi de despacho, gracias por ese viaje Galicia-Donosti y las noches turbulentas. Ojalá que os vaya a todos bonito. Ah y, por supuesto, Idoia. Simplemente quiero decir que de mayor quiero ser como tú.

En esta parte final quiero agradecer a los míos, los de siempre, el simple hecho de estar ahí. Me siento tremendamente afortunada de tener los amigos y familia que tengo, de verdad, creedme. Las primeras, mis amigas, las que siempre están y estarán, las del cole, Irene, Rebe, Noe y Carolain, esas cuatro maravillas que me dejan siempre los pelos de punta. Os quiero mucho. Mis vecinas, intermitentes amigas que por más tiempo que pase, parece que aún podríamos coger los patines y jugar en la urba. Ro, amiga por narices, no te quedó otra opción al nacer, y amigas para siempre. Los de la uni, esta tesis también es en parte vuestra, con el apoyo logístico en la carrera y moral en todo momento. Sergio, pero qué orgullosa estoy de ti grandullón, de verdad. Guille, te quiero muchísimo, aunque creo que tú preferieres a Lía. Álvaro, allá donde te lleve tu mente maravillosa,

llévanos contigo, porfa. Aunque sea por Zoom. Pablo, no me quites nunca de tu estantería, ni de tu lado. Mario, te quiero hermano, somos una piña. Melek, mis halagos se quedan cortos, porque eres bonita por fuera y por dentro. Raquel, cuanto más te conozco, más feliz me siento de tenerte. Gudín, escuchando la radio marroquí en Cádiz, supe que te querría en este grupo para siempre. Rial, el primero, el que siempre ha estado y que, espero, siempre esté. Darío, Javi Sanz y Ocampos, formáis parte de los recuerdos más graciosos que tengo con este grupo, ojalá poder veros más.

Por el lado de la familia, mención de honor a las mamás (lo que hacéis por todos no está pagado, tantas gracias merecéis que no ceben aquí) y tatas, todas sois el pegamento indestructible de la familia, mi núcleo y a quienes acudo para cualquier cosa. Porque ohana significa familia y familia que estaremos siempre juntos. Irene, mi sis, es que no eres ni medio normal. Mi wonder woman siempre protegiéndome y queriéndome como nadie. Siendo honestas, si me casara algún día, tendría que ser contigo, porque estás en lo bueno y en lo malo, en la salud y en la enfermedad, y estarás hasta que la muerte nos separe. Santi, bro, coulant de chocolate, firme por fuera y muy blandito por dentro. No me hace falta ser tan lista como tú, porque sé que siempre podré acudir a ti para ayudarme. Koke, siempre estaremos aquí, que no se te olvide. Papás, qué deciros, sois mi faro cuando estoy perdida y cuando no. Es imposible que me pase nada si estáis ahí. Siempre que me dicen lo trabajadora que soy y las ganas que le pongo a todo, me siento orgullosa de parecerme a ti papá, por dentro y por fuera. Mami, volviendo del cole un día en bachiller, tiempos difíciles para una empollona, me dijiste que lo más difícil ya lo había conseguido: ser buena persona. No te haces una idea de lo importante que fue para mi. Y de lo importante que eres tú para mí. Mis abuelos, que tanto me cuidaron de pequeña y a los que ahora me toca a veces cuidar. Abuelito, sin ti esta familia no sería lo que es, gracias en especial por ello. Mis cinco enanos, tenéis clases gratis para siempre y mi ayuda para cualquier, cualquier, cosa. No prometo amabilidad, pero sí eficacia. Gracias en especial a mi tío Ángel, encargado de imprimir esta tesis, repetiremos el finde de tamborrada algún año. Todos los demás, tíos y primos y demás familia, os quiero. Familia lejana de Vilches, qué cerquita os siento siempre. Cuidadnos mucho los que nos veis desde arriba. Familias postizas, lideradas por Juana y Mari Carmen, no os alejéis nunca.

Ahora, el más importante en estos últimos años. Y el más guapo, claro. No sé ni qué escribir. Ojalá tener la maestría de Robe o Sabina para hacerte entender lo que siento. Decirte que sin ti no sería nada (no al menos lo que soy) se queda muy corto. Deberte tanto y, a la vez, sentir que no te debo nada. El que no sabe de amores no sabe lo que es el martirio, llorona, ¿verdad?. I need you, I don't need you. Estoy orgullosa de lo que eres, de tu fortaleza para sacar a otros del pozo. Sigue volando siempre hacia arriba, y pensando que no puedes perder. Nunca te entregues ni te apartes, junto al camino nunca digas no puedo más y aquí me quedo. Con que lo que nos quede, poco creo, signifique para mí la mitad de lo que estos años lo han hecho, me merecerá la pena vivirlo. Yo no quiero domingos por la tarde, yo no quiero columpio en el jardín. Lo que yo quiero, corazón cobarde, es que mueras por mí. No en plan mal, tú ya me entiendes. I just want to travel with you and I want to travel blind. Y bueno, gracias por traer a mi vida a Adri y Marta. Y mil gracias también a Inma, José y Ana, me hacéis sentir como en casa.

GRACIAS,
Cris

I see the past of the time passing fast.
The present's over and gone.
So know I'm ready, I trust my soul,
I'm hoping to fly with style, we shall know.

Resumen

En física, la separación del momento de un cuerpo entre sus componentes lineal y angular nos ayuda a entender la dinámica del problema. Además, en el momento angular, tradicionalmente distinguimos entre sus componentes orbital, como el movimiento de la Tierra alrededor del Sol, e intrínseco o de espín, como una pelota de baloncesto girando sobre el dedo de un jugador. Formalmente, podemos separar el momento angular (MA), por un lado, según sus propiedades de transformación bajo rotación de un sistema de coordenadas externo (MAO) y, por el otro, según la proyección de su MA intrínseco en una determinada dirección del espacio (MAE).

Esta separación no solo tiene sentido en el mundo macroscópico gobernado por la física clásica, sino también en el mundo microscópico. Seguramente, de hecho, hablar de espín y órbita nos lleva como físicos a pensar casi instantáneamente en el espín y el movimiento del electrón en un átomo. Más aún, esta separación no solo es útil para el movimiento de partículas, sino que podemos usarlo para describir ondas electromagnéticas, por ejemplo. En ese caso, podemos identificar de forma intuitiva la componente de espín con su polarización, es decir, con la rotación del campo eléctrico con respecto a la dirección de propagación. Si, además, tenemos en cuenta que la energía transportada no tiene por qué seguir un movimiento paralelo a la dirección de propagación, podremos identificar una componente orbital también. Aún así, los métodos de estudio de sistemas electrónicos y fotónicos suelen ser muy diferentes, alejándonos de un entendimiento global de la dinámica de estos sistemas.

Con esta tesis, nuestra intención es contribuir a esa visión global de la separación entre MAO y MAE y las posibles interacciones entre ambas, i.e., interacciones de espín-órbita (IEO). En concreto, analizamos dos de las ramas más prometedoras de la física de hoy en día, la espintrónica, con la supervisión del Dr. F. Sebastián Bergeret, y la nanofotónica, de la mano del Prof. Juan José Sáenz. En espintrónica, estas IEO aparecen al tener en cuenta la corrección relativista de acoplo espín-órbita (AEO) en el Hamiltoniano. En nanofotónica, en cambio, el estudio de las IEO es más reciente y aún se siguen estudiando sus orígenes. Por tanto, una introducción teórico-histórica de las IEO en ambas ramas por separado podría ser útil para el lector, sea cual sea su especialidad, como ofrecemos en el capítulo 1.

Hemos querido también incluir la motivación original de esta tesis en la Sección 1.3. Se trata de la posible similitud entre dos conocidos conceptos, y aparentemente diferentes, en el problema de dispersión de una sola impureza de un electrón y de una onda electromagnética. En el

caso electrónico, Berger propuso en 1970 [19] como explicación del efecto Hall anómalo, i.e., el efecto Hall que desvía electrones en direcciones opuestas dependiendo de su espín en materiales ferromagnéticos, lo que llamó el "side-jump". Este se trata de un salto lateral de la función de onda del electrón tras su dispersión con un potencial central y aparece cuando se tiene en cuenta el término relativista de acoplo espín-órbita en el Hamiltoniano. Aunque no es instantáneo, en ese trabajo Berger obvia el origen de este desplazamiento. En el caso fotónico, también se estudia un desplazamiento aparente en campo lejano que surge en la dispersión de onda plana electromagnética con dipolo eléctrico, al que nos referiremos también como espejismo óptico. Al contrario que Berger, Arnoldus et al. (2008) [10] usan su origen físico para demostrar que realmente existen esos desplazamientos, a saber, la trayectoria en espiral del vector de transferencia de energía, i.e., vector de Poynting, dispersada [9]. Nuestra contribución consiste en usar el método de la Ref. [10] para demostrar que el origen de ambos desplazamientos, tanto en dispersión de electrones como de luz, es el mismo: la trayectoria en espiral del vector de transferencia de energía, es decir, la corriente de probabilidad de la función de onda en el caso electrónico y el vector de Poynting en el caso fotónico. En ambos casos, esta estructura en espiral cerca de la impureza, pasa a ser prácticamente rectilínea cuando lo vemos desde lejos, lo que se traduce en un desplazamiento aparente como está representado en la Fig. 1.4.

Sin embargo, como suele ocurrir en la investigación fundamental, a medida que fuimos profundizando en el estudio de las IEO tanto en sistemas electrónicos como en luz, aparecieron dudas aún sin resolver. Más aún, el creciente interés de los últimos años en las IEO tanto en espintrónica (ver, e.g., [42, 18, 157]) como en nanofotónica (ver, e.g., [8, 27, 16]) formó parte de la motivación de esta tesis, como detallamos en la Sección 1.4. En este sentido, los objetivos principales de la tesis pasaron a centrarse en investigar muchas de esas dudas y, algunas de ellas, acabaron convirtiéndose en las publicaciones que están compiladas en esta tesis como capítulos 4–7. Pasamos ahora a resumir estos objetivos.

En espintrónica, los detalles del AEO relativista están bien establecidos en la literatura. Hoy en día, por tanto, podemos estudiar las IEO en transporte electrónico, analizando las consecuencias de los efectos de AEO acumulados, como por ejemplo el efecto acumulado de impurezas en las que los electrones experimentan un "side-jump". La consecuencia principal de las IEO en transporte es que ofrecen la posibilidad de generar, controlar y medir corrientes de espín mediante corrientes eléctricas. Uno de los problemas que aparecen es que los materiales que tienen un AEO fuerte inevitablemente conllevan una relajación o pérdida del espín fuerte también (cf. Sec. 2.1). La solución hoy en día se basa en elaborar dispositivos espintrónicos híbridos, combinando materiales con AEO, donde generar y manipular el espín, y sin AEO, donde transportarlo hasta un detector. En esta tesis ofrecemos una descripción de este tipo de dispositivos híbridos, a partir de las ecuaciones de difusión de la carga y el espín, definiendo las condiciones de frontera necesarias. Por un lado, en el capítulo 4 ponemos el foco en dispositivos con un material con AEO de carácter intrínseco, e.g., Rashba AEO, que aparece debido a la ausencia de simetría de inversión en el material (cf. Sec. 1.1). Por otro, en el capítulo 5 nos centramos en la descripción de sistemas híbridos de dos materiales sin AEO en cuya interfaz aparece AEO. Este acoplo se puede deber a

la acción conjunta de la rotura de simetría espacial en la interfaz y de fuentes extrínsecas, como impurezas. El modelo y métodos usados en ambos casos pueden encontrarse en el capítulo 2.

En nanofotónica, en cambio, todavía existe la necesidad de un estudio detallado de las IEO. Esto, sumado a la accesibilidad experimental de dispersión en impurezas individuales, hace que hoy en día sigan siendo objeto de intensa investigación [27]. Hasta ahora, los estudios teóricos se centraban en dispersión de dipolos puramente eléctricos, con la aparición de los espejismo ópticos que mencionábamos arriba. En esta tesis, ofrecemos una descripción de las IEO en dispersión de luz en partículas que se comportan como un dipolo eléctrico *y* magnético. El modelo y métodos usados están resumidos en el capítulo 2. Debido a la ausencia de materiales magnéticos a frecuencias ópticas, las partículas de materiales dieléctricos con índice de refracción alto (IRE), en los que la circulación de corrientes eléctricas internas es el origen de la respuesta magnética además de eléctrica, son los candidatos preferenciales para este tipo de estudios en gran parte debido a su baja absorción [15]. Dependiendo de la interacción entre esas dos respuestas, podemos conseguir una marcada direccionalidad o asimetría en la dispersión debido a las llamadas condiciones de Kerker [88, 115]. Esto, conlleva la aparición de desplazamientos aparentes que sobrepasan los anteriormente estudiados, incluso llegando a desplazamiento divergentes como demostramos en el capítulo 6. Basándonos en la direccionalidad que aparece en la dispersión, en el capítulo 7 ofrecemos un estudio de las IEO basándonos tan solo en simetría. En este sentido, la helicidad, que en campo lejano coincide con el grado de polarización circular de las ondas, demuestra ser clave para entender los problemas de dispersión [57, 175].

Como conclusión, para poder llegar a entender las posibles analogías y buscar un modelo común entre ambos mundos, hemos tenido que comenzar con un estudio profundo de las IEO en espintrónica y nanofotónica por separado. Gracias a ese estudio, hemos tenido la oportunidad de contribuir con diferentes publicaciones, no solo las compiladas aquí como capítulos 4–7, sino también las correspondientes a las Refs. [121, 120, 118, 119, 151, 69]. Realmente creemos que con esta tesis ofrecemos una visión global de dos de las ramas más prometedoras de la nanofísica, así como una base teórica sólida con la que seguir trabajando para alcanzar ese objetivo original de ofrecer un lenguaje y modelo común para estudiar las IEO en ambas ramas.

Table of contents

List of figures

Nomenclature

Symbols

(I,Q,U,V)	Stokes parameters
α	Rashba strength coefficient
$\alpha_{\mathrm{E,M}}$	electric and magnetic polarizabilities
$\mathbf{\Psi}^{\sigma}_{lm}$	vector spherical harmonic, eigenvector of the helicity operator
$\mathbf{\Delta}$	optical mirage vector
$\boldsymbol{\sigma}$	Pauli matrices vector
$\chi_{e,m}$	electric and magnetic susceptibilities
ℓ	electron's mean free path
$\varepsilon,\ \mu$	permittivity and permeability of a medium
$\varepsilon_0,\ \mu_0$	permittivity and permeability of free space
ε_{ijk}	Levi-Civita symbol
γ^{ab}	*ab* spin-component of the Dyakonov-Perel spin relaxation tensor
$\hat{\mathbf{F}}$	SU(2) Lorentz force
$\hat{\mathscr{A}_0}$	0 component of the SU(2) four-potential
$\hat{\mathscr{A}_k}$	*k* component of the SU(2) four-potential
$\hat{\mathscr{B}_k}$	*k* component of the SU(2) magnetic field
$\hat{\mathscr{E}_k}$	*k* component of the SU(2) electric field
$\hat{\mathscr{F}}_{\mu\nu}$	$\mu\nu$ component of the SU(2) field tensor
$\hat{\Omega}(\mathbf{p})$	effective magnetic field from intrinsic spin-orbit coupling

$\hat{\mathrm{L}}$	light orbital angular momentum operator
$\hat{\mathrm{S}}_{ij}^{\mathrm{spin}}$	light spin angular momentum operator
$\hat{j}_k$	k component of the spin current density
$\hbar$	reduced Planck constant
λ_{N}	spin diffusion length of a normal (without spin-orbit coupling) conductor
Λ_θ	helicity density
$\lambda\!\!\!^{-}$	reduced Compton wavelength
$\mu, \hat{\mu}$	charga and spin electrochemical potentials
μ_{B}	Bohr magneton
ω	angular frequency of electromagnetic fields
ϕ	U(1) scalar potential
ψ_{scatt}	electronic scattered wave function
ρ	charge density
$\sigma_{(0),\mathrm{scat,ext,abs}}$	incident, scattered, extinct, and absorbed electromagnetic cross sections
σ_{D}	Drude conductivity
$\sigma_{\mathrm{sc,cs}}$	spin-to-charge and charge-to-spin interfacial conductivities
τ	momentum relaxation time
τ_{ext}	extrinsic relaxation time
a	scatterer radius
$a_l,\ b_l,\ c_l,\ d_l$	Mie coefficients
$C_{lm}^{\sigma\sigma'}$	plane wave shape coefficients
D	diffusion coefficient
$D_{lm}^{\sigma\sigma'}$	scattered wave shape coefficients
e	electron's elementary charge
E_0	strength of the incident electric field
$F_{\mu\nu}^0$	$\mu\nu$ component of the U(1) field tensor

g asymmetry parameter

g_s dimensionless electron's magnetic moment

$G_{\parallel,\perp}$ interfacial spin-loss conductances for parallel and perpendicular to the interface spin polarizations

H Hamiltonian

$h_l^{(1)}(z)$ spherical Hankel function of the first kind

H_0 kinetic term of the Hamiltonian

H_{SOC} spin-orbit coupling term of the Hamiltonian

$j_l(z)$ spherical Bessel function

m electronic mass

P_k^{ab} ab spin-component and k spatial component of the spin precession tensor

P_0 incident electromagnetic power

$Q_{(0),\mathrm{scat,ext,abs}}$ incident, scattered, extinct, and absorbed electromagnetic efficiencies

$S_l(z),\ C_l(z)$ Riccati-Bessel functions

V averaged voltage drop

v_{F} Fermi velocity

V_{sc} averaged voltage drop induced by spin-to-charge conversion

$W_{(0),\mathrm{scat,ext,abs}}$ incident, scattered, extinct, and absorbed electromagnetic power

$x,\ y$ size parameters

$Y_l^m(\theta,\varphi)$ scalar spherical harmonics

Z medium electromagnetic impedance

$\mathbf{A}$ U(1) vector potential

$\mathbf{A}^0$ U(1) four-potential

$\mathbf{B}$ magnetic strength or induction

$\mathbf{D}$ electric displacement

$\mathbf{E}$ electric field

$\mathbf{F}$ U(1) Lorentz force

$\mathbf{H}$ magnetic field

$\mathbf{J}$ charge current density

$\mathbf{J}^e$ electronic probability current

$\mathbf{J}^{\mathrm{AM}}$ time-averaged total angular momentum

$\mathbf{j}_{\mathrm{c}}$ externally applied charge density current

$\mathbf{j}_{\mathrm{I}}$ interfacial charge density current

$\mathbf{k}$ wave vector

$\mathbf{M}_{(e/o)ml}$ even and odd magnetic vector harmonics

$\mathbf{N}_{(e/o)ml}$ even and odd electric vector harmonics

$\mathbf{p}$, $\mathbf{m}$ electric and magnetic dipole moments

$\mathbf{S}$ time-averaged Poynting vector

$\mathbf{X}_{lm}$ vector spherical harmonic

$\boldsymbol{\mu}_s$ electron's spin magnetic moment

$\boldsymbol{\partial}$ U(1) four-derivative

$\hat{\Lambda}$ helicity operator

$\hat{\mathrm{J}}$ light total angular momentum operator

$\hat{S}$ spin density

j_i i-th component of the total angular momentum density

l_i i-th component of the orbital angular momentum density

s_i i-th component of the spin angular momentum density

Acronyms / Abbreviations

AM Angular momentum

BC Boundary conditions

DoCP Degree of circular polarization

DP Dyakonov-Perel

ECP Electrochemical potential

ESR Extrinsic spin relaxation

EY Elliot-Yafet

HRI High refractive index

ISGE Inverse spin galvanic effect

ISHE Inverse spin Hall effect

ISOC Interfacial spin-orbit coupling

LRI Low refractive index

OAM Orbital angular momentum

SAM Spin angular momentum

SGE Spin galvanic effect

SHE Spin Hall effect

SOC Spin-orbit coupling

SOI Spin-orbit interactions

SQUID Superconducting quantum interference device

Chapter 1

Introduction

Linear and angular momenta are present in our day to day as macroscopic and tangible components of any body's motion. Probably, one of the best examples is a pool table. Complete control of the almost ideal conservation of momentum, with the interaction between linear and possible angular components when balls collide, is the only requirement to win any pool game. Generally speaking, within the angular momentum (AM) of a pool ball, we can distinguish between the so-called spin and swerve effects, i.e., the classical spin (SAM) and orbital (OAM) components. The intrinsic AM or SAM of a body is the rotational motion about its own center of mass axis, such as a basketball's spinning motion on a player finger. In contrast, the OAM component measures the rotational motion about a chosen external axis, such as the Earth in its orbit about the Sun.

However, as a physicist, maybe the first idea that comes to mind when talking about spins and orbits is an atom and the quantum version of AM. In the microscopic world, the most relevant example of spin and orbital AM distinction is the one describing the motion of an electron inside the atom. As early as 1911, Rutherford had already proposed a (classic) atomic model in which the light electrons orbit around the massic nucleus formed by protons and neutrons, a few years before the arrival of the well-known (quantum) Bohr model. In 1925, the concept of an intrinsic AM of the electron was proposed by two of the PhD students of Ehrenfest, Uhlenbeck and Goudsmit [161], being later Pauli (1927) [126] who introduced the concept of spin into quantum mechanics via the spin matrices modifying the Schrödinger equation.

Indeed, classical electrodynamics' applicability fails when interpreting both the orbits as classical paths or the spin as an actual spinning of the electron; we inevitably need to introduce quantum mechanics. Nevertheless, as explained in the textbook by Landau and Lifshitz (2013) [96]:

"...However, with the preceding understanding of the concept of angular momentum, the [quantum] *origin of it becomes unimportant, and we naturally arrive at the concept of an "intrinsic" angular momentum which must be ascribed to the particle regardless of whether it is "composite" or "elementary".*

...The intrinsic angular momentum of a particle is called its spin*, as distinct from the angular momentum due to the motion of the particle in space, called the* orbital angular momentum [...] *For particles having spin, the description of the state by means of the wave function must determine the probability not only of its different positions in space but also of the possible orientations of the spin."*

From this explanation, we can furthermore understand that the applicability of the concepts of spin and orbital AM is entirely general, *"the origin of it becomes unimportant"*, allowing us to analyze under this picture almost every physical phenomena involving the motion, transport, or

dynamics of any particle. Indeed, as explained in the following sections, the distinction between spin and orbital components of the AM can also be introduced for electromagnetic radiation, i.e., light. The common basis is the general classification of the states of the system according to, on the one hand, their transformation properties under rotation of the coordinate system (OAM) and, on the other, the projection of the internal AM on some chosen direction in space (SAM). Applied to an electromagnetic wave, this distinction can be made between the deviation of the energy flow vector (Poynting vector) with respect to the propagation direction and the wave's polarization, related respectively to the OAM and SAM of light.

The main research line of the present doctoral Thesis is the study of SAM and OAM and their possible interactions, i.e., the spin-orbit interactions (SOI), in two different fields of Physics, spintronics and nanophotonics. Through this binary research work, the fundamental aim is to understand the concept and effects of SOI in a general and profound manner, understanding both fields' potential analogies. Whereas the concept of spin-orbit coupling (SOC) in quantum mechanics and its consequences in the field of spintronics is well-established, for light, it is a more recent research field and, consequently, still with open questions.

Indeed, the original plan of this Thesis was to find analogies between SOC in electrons and light. The primary motivation was particularly the study of a single scattering problem of both a free electron and a circularly polarized electromagnetic plane waves, further explained in Sec. 1.3. These scattering problems involve two well-established SOI-related concepts in each of the two fields, the side-jump and the displacement of the far-field image of a radiating dipole, which were first introduced by Berger (1970) [19] and Arnoldus et al. (2008) [10], respectively. In particular, applying the same framework, we show that the side-jump's origin is the spiraling trajectory of the energy flux near the scatterer, as analogous to the origin of the apparent displacement in the work by Arnoldus et al..

However, as is often the case in fundamental research, by deepening the understanding of the SOC in both electronic systems and light, we found novel effects that derived in several publications that form the basis of this Thesis. Indeed, the first two published works derived from this Thesis, "Enhanced spin-orbit optical mirages from dual nanospheres" and "Asymmetry and spin-orbit coupling of light scattered from subwavelength particles", compiled as Chapters 6 and 7, respectively, originate directly from going beyond the electric dipolar regime assumed in the work of Arnoldus et al. [10]. In the case of electronics, experiments are based on transport measurements. The systems are more complex, and we need to consider different effects for their description, such as disorder, different sources of SOC, and the effect of hybrid interfaces between different materials. All these concepts are necessary to understand electronic transport. Our research studies in this field led to two other publications, "Nonlocal magnetoelectric effects in diffusive conductors with spatially inhomogeneous spin-orbit coupling" and "Quantification of interfacial spin-charge conversion in hybrid devices with a metal/insulator interface", compiled as Chapters 4 and 5. In short, this PhD Thesis's research led, on the one hand, to several contributions in these two fields and, on the other, to some hints toward an analogy between SOC in solid-state physics and photonics.

In the rest of this chapter, we provide a theoretical introduction into the main concepts and effects addressed in this Thesis, in both fields, Spintronics and Nanophotonics. This brief review contains the needed physical background for understanding the concept of SOI in each field, and it serves as a starting point for the works that originated from this Thesis. Each of these introductions maybe thus useful for non-experts but elementary for expert readers. Based on these background concepts, in Sec. 1.3 we discuss the original motivation of the Thesis. The final part of this chapter,

Sec. 1.4, outlines the general motivations and specific objectives in each of the fields, spintronics and nanophotonics.

Based on these objectives, we develop an in-depth theoretical study in the present Thesis. For that purpose, we first need to establish the models and methods applied, as we summarize in Chapter 2. The main conclusions of this theoretical work are presented in Chapter 3. Finally, the publications derived from the work done during these four years are compiled as Chapters 4–7.

1.1 Spintronics

In the atomic case, SOC is related to the relativistic interaction between the intrinsic spin of the electrons and the experienced magnetic field in the electron rest frame due to the Lorentz transformation of the electric field from the positive nucleus. Since this interaction thus scales with the atomic or proton number, it is especially notable in crystalline lattices with heavy atoms. In the last decades, such coupling has given rise to a new and intensively studied branch of Physics, spintronics. We further summarize the numerous manifestations and applications of this field in Sec. 1.4.

At the electronic Hamiltonian, SOC removes the spin degeneracy without the action of an external magnetic field. Namely, this coupling enters as an effective Zeeman interaction between the electron SAM and OAM, i.e., between its spin and the orbital motion:

$$H_{\mathrm{SOC}} = -\boldsymbol{\mu}_s \cdot \mathbf{B}_{\mathrm{eff}} \,. \tag{1.1}$$

Here, $\boldsymbol{\mu}_s = -g_s \mu_{\mathrm{B}} \mathbf{S}/\hbar$ is the spin magnetic moment of the electron, with $g_s \approx 2$ the dimensionless electron's spin moment or g-factor, $\mu_{\mathrm{B}} = e\hbar/(2m)$ the Bohr magneton, and $\mathbf{S} = \hbar\boldsymbol{\sigma}/2$ the SAM operator, with $\boldsymbol{\sigma}$ the Pauli matrices. The perceived magnetic field by the moving electron due to the nucleus electric field, $\mathbf{E} = -e^{-1}\boldsymbol{\nabla} U$, with U the electric potential energy, is:

$$\mathbf{B}_{\mathrm{eff}} = \frac{\hbar}{emc^2}\, \mathbf{k} \times \boldsymbol{\nabla} U \,, \tag{1.2}$$

with $\mathbf{k}$ the wave vector describing the motion of the electron. Therefore, the SOC term reads:

$$H_{\mathrm{SOC}} \propto \frac{\hbar^2}{2m^2c^2} \boldsymbol{\sigma} \cdot (\mathbf{k} \times \boldsymbol{\nabla} U) \,. \tag{1.3}$$

Even though this naive derivation is qualitatively correct, we need to take what is known as *Thomas half*, due to the correction to the energy shown by Thomas (1926) [154]. Finally, the relativistic SOC term in the Hamiltonian has the following well-known form:

$$H_{\mathrm{SOC}} = \frac{\lambda\!\!\!^{-2}}{4} \boldsymbol{\sigma} \cdot (\mathbf{k} \times \boldsymbol{\nabla} U) \,, \tag{1.4}$$

with $\lambda\!\!\!^{-} = \hbar/(mc)$ the reduced Compton wavelength. Equation (1.4) can be seen as the starting point for any effective Hamiltonian describing systems with SOC of any kind [166]. As can be inferred from this generic term, the coupling between electron's spin and momentum could not only be generated by the nucleus potential, but by any effective magnetic field affecting the electronic transport. In this regard, a distinction can be made based on the dominant influence of either "extrinsic" or "intrinsic" SOC. The former refers to the asymmetric deflection after scattering from SOC interaction with extrinsic potential impurities [19, 146, 145, 116]. Examples of extrinsic

potentials are (non-magnetic) impurity scattering (analyzed in Sec. 1.3), phonons, surfaces or interfaces, grain boundaries, etc.

On the other hand, the lack of inversion symmetry in a system can also lead to spin-split degeneration of the electronic energy bands. This phenomenon is referred to as intrinsic SOC. In this regard, Dresselhaus (1955) [44] was the first to introduce an intrinsic cubic-in-momentum SOC Hamiltonian describing bulk zincblende semiconductors, which was later shown to be reduced to a linear-in-momentum term for two-dimensional electronic transport [49]. Few decades later, Vas'ko (1979) [164] and Bychkov and Rashba (1984) [34] applied this concept to non-centrosymmetric quantum wells at which the two-dimensional transport is described by the well-known linear-in-momentum Rashba SOC term. Generally speaking, any intrinsic SOC term can be included in the electronic Hamiltonian as follows (see, e.g. [20]):

$$H = H_0 + H_{\mathrm{SOC}} = \frac{p_k p_k}{2m} + \hat{\Omega}(\mathbf{p}) = \frac{p_k p_k}{2m} + \frac{\Omega^a(\mathbf{p})\sigma^a}{2} \,. \tag{1.5}$$

Here, we introduce the Einstein summation notation, useful for the spintronics analysis of this Thesis. Upper indices correspond to spin components, $a = x, y, z$, and lower indices to spatial ones, $k = x, y, z$. Spin structure is denoted by hat symbol and $\sigma^{x,y,z}$ are the Pauli matrices. Similarly to the Zeeman effect, moving electrons will precess around the direction of the momentum-dependent effective magnetic field $\Omega^a(\mathbf{p})$.

In the particular case of Rashba SOC, addressed in Chapter 4, a naive derivation of $\Omega^a(\mathbf{p})$ can be obtained. Let us assume a two-dimensional electron gas in the x–y plane, with a constant, homogeneous electric field in the z direction, generated by the symmetry breaking. In Eq. (1.4), we can thus substitute $\mathbf{k} = \hbar^{-1}(p_x, p_y, 0)$ and $\mathbf{E} = 4\hbar(e\lambda\!\!\!^{-})^{-1}\alpha\ \hat{\mathbf{e}}_z$, with α the so-called Rashba strength coefficient. Comparing with Eq. (1.5), we can see that the only finite components of the Rashba linear-in-momentum effective field are $\Omega^x = 2\alpha p_y$ and $\Omega^y = -2\alpha p_x$. This shall serve for any system at which an effective electric field arises due to the absence of inversion symmetry such as non-centrosymmetric bulk materials, interfaces, or surface states. Hence, the Rashba Hamiltonian reads as follows:

$$H = H_0 + H_{\mathrm{SOC}} = \frac{p_k p_k}{2m} + \alpha(p_x\sigma^y - p_y\sigma^x) \,. \tag{1.6}$$

Linear-in-momentum SOC and, specifically, Rashba SOC are reviewed in Sec. 2.

In practice, at systems with sufficiently strong SOC, either extrinsic or intrinsic, the opposite coupling to the charged electrons depending on its spin direction, and vice versa, lead to the interconversion between spin (or magnetic) and charge (or electric) degrees of freedom. Consequently, SOC is related to a variety of magnetoelectric effects that appear in the absence of an external magnetic field. For that reason, conductors with sizable SOC are used for the creation and control of spin currents and spin densities by applying electric fields. Reciprocally, magnetoelectric effects allow for detecting spin by measuring electric signals [177, 145].

It is customary to distinguish between two kinds of magnetoelectric effects mediated by SOC: those relating spin and charge currents (spin Hall effect and its inverse) and those relating spin polarization and charge current (spin-galvanic effect and its inverse). These two phenomena are illustrated in Fig. 1.1. The spin Hall effect (SHE) is the generation of a spin current, transverse to the applied charge current [73, 50, 166, 145]. The inverse effect, commonly known as the inverse SHE (ISHE) [145], corresponds to the spin-to-charge counterpart and consists of a charge current,

or a Hall voltage, induced by a given spin current. Both SHE and ISHE have been measured in several experiments and different materials [86, 143, 162, 92, 140, 137].

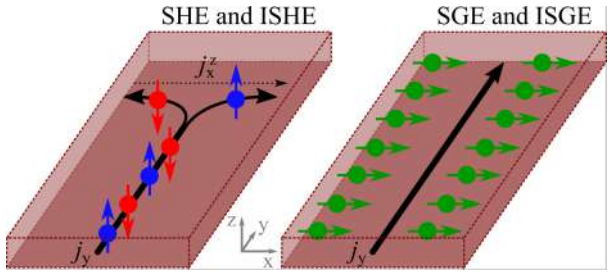

Fig. 1.1 Left panel illustrates the spin Hall effect and its inverse, relating a charge current, j_y, with a spin current in the perpendicular direction and polarized perpendicular to both currents, j_x^z. Right panel illustrates the spin galvanic effect and its inverse, relating a charge current, j_y, with a spin density polarized perpendicular to it.

The spin-galvanic effect (SGE), also known as the inverse Edelstein effect (IEE), refers to the generation of a charge current by creating a non-equilibrium spin polarization in the material. Conversely, the inverse SGE (ISGE) corresponds to the spin polarization induced by applying an electric field/current [48, 103, 11, 176, 17, 64, 102, 68] and is also known as the Edelstein effect (EE) [53, 141]. In contrast to the SHE, the induced spin is homogeneous in space and, in principle, in the stationary case, no spin currents are generated [112, 130, 78, 129, 122]. Observation of SGE and ISGE has been reported in Refs. [143, 149, 60, 138, 85, 79].

In a symmetry framework, the SHE and ISHE are universally present in all conductors with non-negligible SOC without any symmetry restriction, i.e., originates from either extrinsic or intrinsic mechanisms. In contrast, the SGE and ISGE, require the absence of inversion symmetry and, more precisely, gyrotropic systems [160, 30], i.e., originates only from intrinsic SOC. Consequently, two-dimensional systems such as surfaces or interfaces represent ideal candidates for the theoretical and experimental study of magnetoelectric effects, as they are always locally gyrotropic. Significantly, SOC effects are greatly enhanced in such systems since the resultant electric field from the broken inversion symmetry couples to the electron spin effectively via Eq. (1.4), affecting the electronic transport even in conventional conductors such as Cu or Au.

1.2 Nanophotonics

The fundamental particle in the field of photonics is the photon, which can only be described under quantum considerations. Fortunately, light seen as electromagnetic radiation, only dealing with the photon wave character, was accurately described by the classical theory of fields developed by Maxwell in 1873 [109]. The use of Maxwell's equations as the photon's quantum motion equations indeed yields the conclusion that photons' wave properties coincide with those of the electromagnetic fields.

However, since the wave picture may not be sufficient in all scenarios involving light-matter interaction, it is necessary to clarify the scales this Thesis deals with. How light-matter interaction is addressed fully depends on the relation between the incident wavelength and the object scales considered. The description of the interaction ranges from geometrical optics, in which the wavelength is much larger than the object dimensions, to Rayleigh optics, in which the opposite limit is assumed. This Thesis is halfway between these two limits and is focused on the light-matter interactions that arise when the incident wavelength and matter scales are of the same order of magnitude. Specifically, the present work studies light-matter interactions at the nanometer scale, a field commonly known as nanophotonics. The incident wavelength typically ranges from the ultraviolet to the near-infrared, passing through the visible range. Nanophotonics thus studies the interaction of light with nano-sized particles as biological cells or nanospheres made of silicon within this band spectrum. At these scales, the physical effects studied require the description of light as an electromagnetic wave, and the classical Maxwell's equations are suitable to describe the fields. Furthermore, we consider weak enough radiation to avoid possible thermodynamical effects.

Maxwell's equations encompass the major laws of electricity and magnetism, which is one of the great unifications in physics until the date. Namely, they encode the four differential equations describing electric and magnetic fields, the relations between them, and their relation with their possible sources, i.e., charge densities and currents. These consist of the Gauss's law for both electric and magnetic fields, stating that only static electric fields can be related to a source, whereas no magnetic monopoles exist. In addition, the third equation describes the possible generation of an electric field from a time varying magnetic one, known as the Maxwell-Faraday's law. Finally, the Maxwell-Ampère's law conclude the set of equations describing how a magnetic field can be built from both an time-varying electric field or an electric current. Their differential form reads:

$$\boldsymbol{\nabla}\cdot\mathbf{D}=\rho\,, \tag{1.7}$$

$$\boldsymbol{\nabla}\cdot\mathbf{B}=0\,, \tag{1.8}$$

$$\boldsymbol{\nabla}\times\mathbf{E}+\frac{\partial\mathbf{B}}{\partial t}=0\,, \tag{1.9}$$

$$\boldsymbol{\nabla}\times\mathbf{H}=\mathbf{J}+\frac{\partial\mathbf{D}}{\partial t}\,, \tag{1.10}$$

where, respectively, $\mathbf{E}$ and $\mathbf{H}$ are the electric and magnetic fields, and ρ and $\mathbf{J}$ are the charge density and current associated with "free" charges. The electric displacement $\mathbf{D}$ and magnetic strength or induction $\mathbf{B}$ are:

$$\mathbf{D}=\varepsilon_0\mathbf{E}+\mathbf{P}\,,\quad \mathbf{B}=\mu_0\left(\mathbf{H}+\mathbf{M}\right)\,, \tag{1.11}$$

where $\mathbf{P}$ is the electric polarization, $\mathbf{M}$ the magnetization, and ε_0 and μ_0 are the vacuum permitivity and permeability, respectively. Maxwell's equations are not sufficient in themselves, but need to be supplemented with the *constitutive relations*. Here, we assume the following relations [28]:

$$\mathbf{J} = \sigma\mathbf{E}\,, \quad \mathbf{P} = \varepsilon_0\chi_e\mathbf{E}\,, \quad \mathbf{M} = \chi_m\mathbf{H}\,, \tag{1.12}$$

where σ is the conductivity and $\chi_{e/m}$ is the electric/magnetic susceptibility. These coefficients will be assumed to be independent of the fields, position or direction, i.e., the materials studied here are linear, homogeneous, and isotropic. In addition, we assume harmonic time-dependence of the fields, i.e., $e^{-\mathrm{i}\omega t}$. In *complex representation* [81], $\mathbf{E}(\mathbf{r},t) = \Re\left\{\mathbf{E}(\mathbf{r})e^{-\mathrm{i}\omega t}\right\}$ and $\mathbf{H}(\mathbf{r},t) = \Re\left\{\mathbf{H}(\mathbf{r})e^{-\mathrm{i}\omega t}\right\}$ and, therefore, we can rewrite Maxwell's equations as follows:

$$\boldsymbol{\nabla}\cdot(\varepsilon\mathbf{E}(\mathbf{r})) = 0\,, \tag{1.13}$$

$$\boldsymbol{\nabla}\cdot\mathbf{H}(\mathbf{r}) = 0\,, \tag{1.14}$$

$$\boldsymbol{\nabla}\times\mathbf{E}(\mathbf{r}) = \mathrm{i}\omega\mu\mathbf{H}(\mathbf{r})\,, \tag{1.15}$$

$$\boldsymbol{\nabla}\times\mathbf{H}(\mathbf{r}) = -\mathrm{i}\omega\varepsilon\mathbf{E}(\mathbf{r})\,, \tag{1.16}$$

with $\mu = \mu_0(1+\chi_m)$ the medium permeability and $\varepsilon = \varepsilon_0(1+\chi_e)+\mathrm{i}\sigma/\omega$ the medium permittivity.

However, in most scenarios, Maxwell's equations' exact solution is tough to obtain, at least, in an analytical form. Furthermore, given its vectorial nature, an unambiguous distinction between the spin and orbital AM components of light, i.e., between SAM and OAM, and its formal definition is not straightforward at all (see, e.g., [27, 25, 168, 108]).

Nevertheless, in many optical problems, the electromagnetic fields can be assumed to propagate mostly along a particular straight direction, e.g., z direction as chosen in this Thesis. This limit is known as paraxial approximation [117] and, when light is considered within this approximation, the distinction between SAM and OAM becomes meaningful and convenient [172, 27, 4]. The first quantification of SAM of a circularly polarized light paraxial beam was done by Beth (1936) [22] following the seminal work of Poynting (1909) [128], observing transfer of light SAM to a birefringent plate. The explicit value of the OAM, on the other hand, was firstly calculated by Allen et al. (1992) [3] for a realizable paraxial light beam, namely, a Laguerre-Gaussian beam.

Let us assume a paraxial beam propagating along the z direction. In this framework, the electromagnetic field's SAM or "intrinsic" AM component can be related to the polarization of light, depicted in Fig. 1.2(a). Light with well-defined SAM corresponds to electromagnetic waves with right- or left-handed polarization, corresponding to $s_z = \pm 1$. In contrast, the OAM is the AM contribution due to the motion of the wave in space, which in the paraxial case, reduces to the possible revolution around the propagation direction of the energy transfer rate vector, as illustrated in Fig. 1.2(b). This revolution traduces in a certain helical phase front with corresponding value of the OAM l_z, which can take infinite (discrete) values, $l_z = (-\infty, \infty)$. Since the energy orbits around the propagation axis, this axis corresponds to a zero intensity direction. Hence, light beams carrying this kind of OAM are also called optical vortices. However, if we assume that the propagation direction is shifted with respect to the coordinate origin, another contribution to the OAM arises. This corresponds to the so-called "extrinsic" OAM [27], depicted in Figure 1.3. Even though this component can be neglected for incident beams, in scattering problems, where the energy transfer vector may be non-radially scattered, this component of the OAM contributes (see Sec. 1.3).

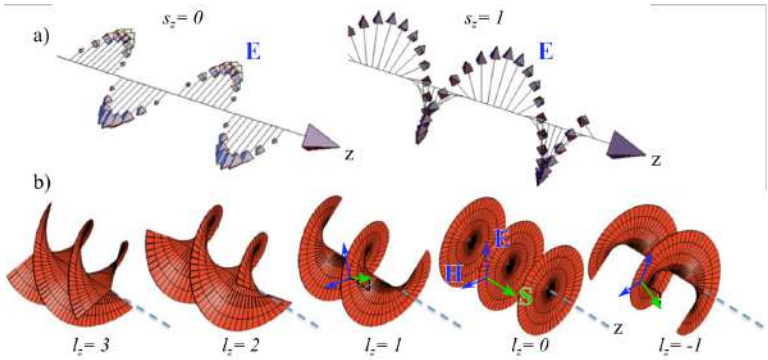

Fig. 1.2 (a) The spin angular momentum (SAM) of light is connected to its polarization, i.e., the revolution of the electric field, **E**, around the propagation direction, z in this case. An electromagnetic wave carries no SAM if the polarization is linear (left panel), whereas its extreme values correspond to right or left circular polarization (right panel). (b) The orbital angular momentum (OAM) corresponds to the revolution of the energy transfer rate vector, i.e., Poynting vector **S**, around the propagation direction z. These figures are adapted from Ref. [172].

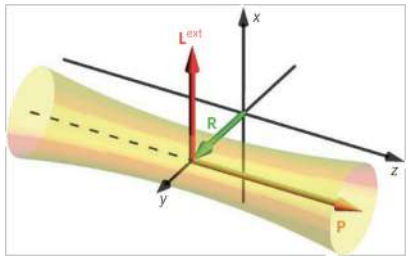

Fig. 1.3 Extrinsic orbital angular momentum (in red) of a paraxial beam. It arises when the propagation direction (in yellow) is not aligned with the coordinate origin. Figure adapted from Ref. [27].

In this Thesis, we analyze the scattering of circularly polarized plane waves. The distinction between SAM and OAM is straightforward for the plane wave case. Since, by definition, the energy transport in a plane wave is parallel to the propagation direction, its OAM is zero. In contrast, its circular polarization leads to $s_z = \pm 1$, depending on the direction of rotation of the electric field. However, SAM and OAM values need to be calculated for scattering waves and depend on the scattering angle.

Formally, we can calculate the SAM and OAM contributions from the corresponding operators. We can identify these operators within the definition of the total AM. First, the energy transfer rate vector, i.e., energy per unit area and unit second, is but the Poynting vector entering the Poynting or energy conservation theorem [81] and it is defined as follows:

$$\mathbf{S} = \mathbf{E}(\mathbf{r},t) \times \mathbf{H}(\mathbf{r},t)\,. \tag{1.17}$$

The time-average of the Poynting vector assuming harmonic time-dependence reads [28]:

$$\langle \mathbf{S} \rangle = \frac{1}{2} \Re \{ \mathbf{E}(\mathbf{r}) \times \mathbf{H}^*(\mathbf{r}) \} \ . \tag{1.18}$$

From here on, $\langle \mathbf{S} \rangle$ is directly represented by $\mathbf{S}$ and the fields $\mathbf{E} = \mathbf{E}(\mathbf{r})$, and $\mathbf{H} = \mathbf{H}(\mathbf{r})$ correspond to the spatial part in complex representation. The definition of the (time-averaged) total AM (AM per unit volume, $J \cdot s/m^3$) of the beam can be calculated from the Poynting vector as follows [81, 38]:

$$\mathbf{J}^{\mathrm{AM}} = \frac{\mathbf{r} \times \mathbf{S}}{c^2} \ . \tag{1.19}$$

From this equation, the formal separation of the AM of light into its OAM and SAM components was firstly suggested by Humblet (1943) [77]. For a monochromatic time-harmonic wave in a non-absorbing medium, the Poynting vector reads as $\mathbf{S} = (1/(2\omega\mu))\Re\{\mathbf{E} \times (-\mathrm{i}\boldsymbol{\nabla} \times \mathbf{E}^*)\}$ (see Eq. (1.15)). We can then split the latter into two different terms and identify each one with the OAM and SAM parts in Eq. (1.19) as follows [38]:

$$J_i^{\mathrm{AM}} = \frac{1}{c^2} \frac{1}{2\omega\mu} \Re\{ E_j^* [-\mathrm{i}(\mathbf{r} \times \boldsymbol{\nabla})]_i E_j + E_j^* (-\mathrm{i}\varepsilon_{ijk}) E_k \} \ , \tag{1.20}$$

where Einstein notation is assumed, Latin letters run over the spatial components, (x, y, z), and ε_{ijk} is the Levi-Civita symbol. Within this equation, we can therefore identify the OAM operator, $\hat{\mathrm{L}} = [(\mathbf{r} \times \hat{\mathrm{P}})]$ with $\hat{\mathrm{P}} = -\mathrm{i}\boldsymbol{\nabla}$ the linear momentum operator, and SAM operator, $\hat{\mathrm{S}}_{jk}^{\mathrm{spin}} = -\mathrm{i}\varepsilon_{ijk}$ [57]. Accordingly, the total AM operator reads $\hat{\mathrm{J}} = \hat{\mathrm{L}} + \hat{\mathrm{S}}_{jk}^{\mathrm{spin}}$. Analogous to quantum mechanics, each of the spatial components of the density *per photon* of these operators can be computed as follows [38, 26]:

$$l_i = \frac{\Re\{ E_j^* [-\mathrm{i}(\mathbf{r} \times \boldsymbol{\nabla})]_i E_j \}}{E_j^* \cdot E_j} \ , \tag{1.21}$$

$$s_i = \frac{\Re\{ E_j^* (-\mathrm{i}\varepsilon_{ijk}) E_k \}}{E_j^* \cdot E_j} = \frac{-\mathrm{i}(\mathbf{E}^* \times \mathbf{E})_i}{E_j^* \cdot E_j} \ , \tag{1.22}$$

and the components of the total AM density are thus $j_i = l_i + s_i$.

In this Thesis, the SOC interaction that is analyzed relies on the conservation of the total AM in the wave propagation direction, j_z, in the scattering of light of azimuthally-symmetric particles, which is introduced in Chapter 2. This conservation leads to the mutual transformation between s_z and l_z in the scattering process. The scattering problem is particularized for spheres, which constitutes one of the most studied electromagnetic systems with an exact solution of Maxwell's equations: the scattering of a homogeneous and isotropic sphere in a non-absorbing medium under plane wave illumination. Thereupon, the history of the origin of this electromagnetic scattering problem is below briefly introduced.

The electromagnetic scattering by a homogeneous and isotropic sphere embedded in a lossless medium under plane wave illumination is commonly referred to as Mie scattering, although Mie was not the first to address this problem 1908 [110]. Almost twenty years before Mie, Lorenz solved this scattering problem independently [101]. Furthermore, Debye solved the related problem of radiation pressure on a spherical particle [41]. Hence, the scattering by a homogeneous and isotropic sphere embedded in a non-absorbing host medium under plane wave illumination has also

been referred to as Lorenz-Mie theory, or even Lorenz-Mie-Debye theory. However, Mie's name has predominantly stuck in the literature [100]. Notably, this recognition did not arrive immediately after publishing his work "*Contributions to the optics of turbid media, particularly colloidal metal suspensions*" [110]. This paper aims for a fundamental theoretical explanation of the coloration of metals in a colloidal state. At that time, Mie, and the scientific community, considered his treatise to be a rather trivial application of Maxwell's contribution. Moreover, the interest in colloidal suspensions was clearly not comparable to the one nowadays. Due to this fact, Mie's contribution remained almost inconspicuous for over fifty years. Interestingly, this paper is sometimes referred to as Dornröschen (Sleeping Beauty) because of its late recognition considering both the increasing interest in the field and the actual number of citations. The recognition doubtless arrived after the book of Stratton (1941) [152]. In the latter, the Mie theory was reformulated in terms of the vector spherical harmonics making the so-called Mie theory more accessible and understandable for a broad scientific audience. Besides Stratton's book, a crucial role in the dissemination and popularization of the Mie theory has been played by the monographs by Hulst and van de Hulst (1981) [76], Born and Wolf (2013) [31], Kerker (1969) [87], and Bohren and Huffman (2008) [28].

1.3 Original motivation of this Thesis

Originally, this doctoral Thesis stemmed from the idea of deeply understanding the concept of spin-orbit coupling and the possible connection between the branches of nanophotonics, with the supervision of Prof. Juan José Sáenz, and spintronics, with Dr. F. Sebastián Bergeret. In particular, the starting point was the scattering from a spherical impurity of electromagnetic and free-electron plane waves, respectively, when taking into account the respective SOI. Firstly, in spintronics, the well-known work by Berger (1970) [19] proposed an explanation for the anomalous Hall effect in ferromagnets as an apparent discontinuous shift of the wave function of the electron after scattering from a central potential. Berger called this apparent shift "side-jump", which is nowadays accepted as one of the extrinsic contributions, together with the skew scattering, of both the anomalous and spin Hall effects (for a review see, e.g., Ref. [145]). In Berger's work, this effect's dynamical origin is rather neglected, stated as follows "*Of course, the side jump is not instantaneous, but the details of electron motion inside the scattering potential are irrelevant for our purpose*". In sharp contrast, the work by Arnoldus et al. (2008) [10] focuses on the geometrical origin of the apparent shift found in the scattering of an electric dipole, shift already predicted by Darwin in 1932 [39] and previously studied for other geometries (see, e.g., Ref. [123, 27]). In the spherical case, this shift is indeed the far-field effect of the scattered Poynting vector's spiraling spatial trajectory.

In order to find a possible analogy, we should thus use the same framework in solving both scattering problems, e.g., the geometrical argument from which the origin of both effects could also be analyzed. In the following, the work of Arnoldus et al. [10] is first summarized, then applied to the electron scattering from a central potential, and finally compared to the result of Berger [19].

In the work of Arnoldus et al., the problem of a circularly polarized plane wave, $\mathbf{E} = E_0 e^{ikz}(\hat{\mathbf{e}}_\mathbf{x} + i\sigma\hat{\mathbf{e}}_\mathbf{y}/\sqrt{2})$ with $\sigma = \pm 1$ for left-/right-handed incident circular polarization, scattered by a small spherical particle, i.e., an electric dipole, is solved. In this case, the only finite component of the SAM calculated using Eq. (1.22) is therefore $s_z = \pm\sigma$. The resulting scattered Poynting vector has the following form [9]:

$$\mathbf{S} = \frac{3P_0}{8\pi r^2}\left[\left(1 - \frac{\sin^2\theta}{2}\right)\hat{\mathbf{e}}_\mathbf{r} + \frac{\sigma}{kr}\left(1 + \frac{1}{(kr)^2}\right)\sin\theta\hat{\mathbf{e}}_\varphi\right], \tag{1.23}$$

where the chosen coordinate system is $z = r\cos\theta$, $x + \mathrm{i}y = r\sin\theta e^{\mathrm{i}\varphi}$, and P_0 is the incident power. Directly from this equation, it can be seen that the Poynting vector has an angular component that traduces in a spiraling trajectory in the near/medium-field. In far-field, the Poynting vector would practically follow a straight line, and, therefore, we can assume the paraxial approximation. However, this straight line is slightly displaced from the external coordinate origin, i.e., the particle's center. This far-field displacement translates into an extrinsic contribution to the OAM (see Fig. 1.3). As illustrated in Fig. 1.4, this leads at the far-field to an apparent shift of the particle, an effect also referred to as *optical mirage* throughout this Thesis.

The value of this shift can be calculated from the sine of the angle between the scattered Poynting vector and the radial vector. Using for example $\mathbf{S_1}$ in Fig. 1.4 and its angle with S_r in the far-field, the sine is equal to both $\boldsymbol{\Delta}_1/r$ and $-\mathbf{S}_\perp/|\mathbf{S}\cdot\hat{\mathbf{e}}_\mathbf{r}|$, where $\mathbf{S}_\perp$ is the perpendicular to the radial component of $\mathbf{S}$. Therefore, the value of the apparent shift can be calculated as [70]:

$$\boldsymbol{\Delta} = \lim_{kr\to\infty} -r\frac{\mathbf{S}_\perp}{|\mathbf{S}\cdot\hat{\mathbf{e}}_\mathbf{r}|} = \frac{\sigma}{k}\frac{2\sin\theta}{\sin^2\theta - 2}\,\hat{\mathbf{e}}_\varphi\,. \tag{1.24}$$

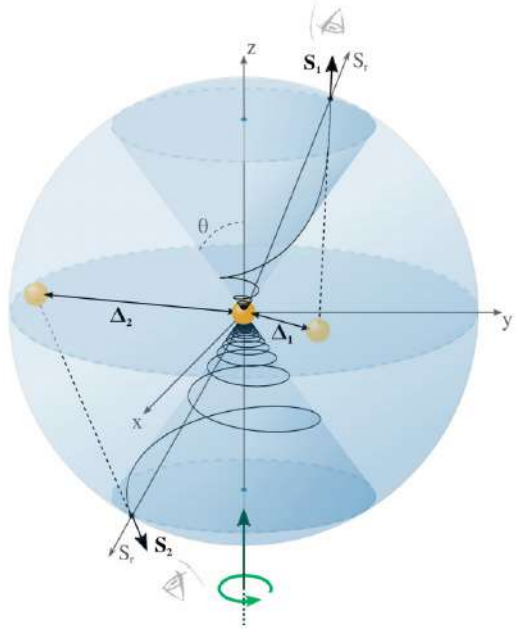

Fig. 1.4 Schematic representation of the optical mirage vector when considering a clockwise circularly polarized incoming wave (thick green straight arrow lying on the z axis). The observer, represented by an eye, perceives a non-radial scattered Poynting vector ($\mathbf{S_1}$, $\mathbf{S_2}$) that leads to an apparent shift ($\boldsymbol{\Delta}_1$, $\boldsymbol{\Delta}_2$) of the dipole localization, both lying on the x–y plane.

Secondly, in the work of Berger [19], the scattering of a free electron plane wave by a short-range square-well potential in the presence of SOC is reviewed. The free electron is incident in the x direction, with spin perpendicular to it and eigenstate of the S_z component [146]. The scattered wave function reads as follows:

$$\psi_\mathrm{scatt} = b_0 h_0(kr) + \sigma q_1 h_1(kr)\sin\theta\sin\varphi\,. \tag{1.25}$$

Here, the chosen coordinate system is $x = r\cos\theta$, $z + \mathrm{i}y = r\sin\theta e^{\mathrm{i}\varphi}$, k is the incident wavenumber, $\sigma = \pm 1$ as the eigenvalues of the spin, b_0 and q_1 the scattering coefficients. The limit $ka \ll 1$, with a the scatterer radius, is assumed. Analogous to the Poynting vector in photonics, the probability current, $\mathbf{J}^e = \frac{\hbar}{m}\{\psi^*_{\mathrm{scatt}}\boldsymbol{\nabla}\psi_{\mathrm{scatt}}\}$, is the vector that describes the magnitude and direction of the energy transfer rate of the wave function. Since this calculation intends to demonstrate that the side-jump can be explained via the corresponding version of the geometrical argument illustrated in Fig. 1.4, the short-range and Born approximations can be taken for simplicity. The probability current in spherical coordinates for this case reads as follows:

$$\mathbf{J}^e \approx \frac{\hbar}{mkr^2}\left[|b_0|^2\,\hat{\mathbf{e}}_{\mathbf{r}} - \frac{\sigma}{kr}\Re\{b_0^* q_1\}\left(\cos\theta\sin\varphi\;\hat{\mathbf{e}}_\theta + \cos\varphi\;\hat{\mathbf{e}}_\varphi\right)\right], \tag{1.26}$$

revealing the near/medium-field angular components that provide a spiraling trajectory to the probability current of the electron in the scattering process. This spiraling trajectory can be understood as the geometrical origin of the so-called side-jump, illustrated as well in Fig. 1.4 if substituting the incident circularly polarized plane wave, subwavelength particle, and Poynting vector by an incident (spin-structured) free electron plane wave, central potential, and probability current, respectively.

Applying the corresponding form of Eq. (1.24), using $\mathbf{J}^e$ instead of $\mathbf{S}$, yields the following expression for the apparent shift:

$$\boldsymbol{\Delta} = \lim_{kr\to\infty} -r\frac{\mathbf{J}^e_\perp}{|\mathbf{J}^e\cdot\hat{\mathbf{e}}_{\mathbf{r}}|} = \frac{\sigma}{k}\frac{\Re\left\{b_0^* q_1\right\}\left(\cos\theta\sin\varphi\;\hat{\mathbf{e}}_\theta + \cos\varphi\;\hat{\mathbf{e}}_\varphi\right)}{|b_0|^2}\,. \tag{1.27}$$

Finally, this expression in the forward direction, $\theta = 0$, can be reduced to:

$$\boldsymbol{\Delta} = \frac{\sigma}{k}\frac{\Re\left\{b_0^* q_1\right\}}{|b_0|^2}\,\hat{\mathbf{e}}_{\mathbf{y}} = \frac{\sigma}{6}k\lambda\!\!\!^{-2}\,\hat{\mathbf{e}}_{\mathbf{y}}\,, \tag{1.28}$$

coinciding with the well-known result for the side-jump of Berger [19].

It is important to notice that in Berger's paper, the incident plane wave is spin-polarized perpendicular to the propagation direction, whereas in the work of Arnoldus et al. the incident SAM is parallel to it. This is why in Eqs. (1.26) and (1.27) there is an additional angular component $\hat{\mathbf{e}}_\theta$. Nevertheless, in both cases, the geometrical analysis demonstrates that the spiraling structure of the energy flux near the scatterer is responsible for the possible apparent displacements after scattering.

In conclusion, this first comparative analysis would appear to open the door to understanding impurity (extrinsic) scattering SOC effects from the same point of view in both spintronics and nanophotonics: a scattering angular-dependent apparent shift originated from the spiraling trajectory of the energy flow after scattering. Furthermore, this effect depends on the particle's spin or the electromagnetic wave's circular polarization, being opposite for spins up and down or left- and right-handed polarization. That is why in both fields, this deflection SOC effect is referred to as spin Hall effect: opposite deflection, and displacements, due to the SOI depending on the spin of the incoming wave. However, although this may be a strong and beautiful common starting point, it is only related to the extrinsic character of the origin of the spin Hall effect. As explained below, scattering experiments are nowadays deeply investigated in nanophotonics, but in spintronics, the accessible measurements are transport experiments, in which disorder and intrinsic SOC need to be taken into account.

In nanophotonics, the study of single impurity scattering involving SOI is still a matter of intense research. It follows from the fact that it is experimentally accessible since the related effects such as the optical mirage are of the order of the incident wavelength. The optical mirage effect is particularly significant when greater accuracy in measurements is needed since any apparent shift seen by the detector yields localization errors (see Sec. 1.4.2). In this Thesis, this problem is further analyzed. Particularly, the consequences of going beyond the electric dipolar regime, with the interaction between the electric and magnetic dipolar orders, are deeply investigated.

In contrast, the SOC's relativistic character in spintronics translates into challenging to measure effects, such as the side-jump of Eq. (1.28), which is much smaller than the Compton wavelength. Consequently, SOC is studied from the point of view of electronic transport in mesoscopic conducting systems. SOC links electron's charge and spin degrees of freedom, which, in transport, translates into mutual interconversion of charge and spin currents and, therefore, electric voltage drop measurements are the usual SOC signature used in spintronics. Besides, experiments are usually carried out in conductive systems such as ferromagnets or semiconductors, in which disorder plays a role. The latter affects spin and charge transport, even in spin-independent disorder, e.g., randomly distributed lattice defects, boundaries, or thermal fluctuations. In spin transport, disorder can yield modification of the spin direction, i.e., spin relaxation. The comparison between the mean free path of the electrons in the system, ℓ, with the spin relaxation length, λ_s, is therefore used as a signature of the transport regime present in the system. In this regard, electronic transport most frequently occurs in the diffusive regime, in which the mean free path is the smallest length scale considered in the system, i.e., $\ell \ll \lambda_s$.

Concerning SOC's origin in mesoscopic transport, within the extrinsic potential scattering, in addition to the side-jump briefly explained above, there also appears the so-called skew-scattering contribution [145]. Furthermore, there is also an intrinsic contribution to the magnetoelectric effects, to the SHE, and the SGE, as mentioned in Sec. 1.1. Consequently, this Thesis is developed not only to the study of SOC in impurity scattering but also of the SOC intrinsic origin to acquire a complete theoretical basis in SOC in spintronics. In particular, intrinsic SOC can be understood as effective magnetic and electric fields within the SU(2) formalism, finding a useful analogy with the Lorentz force in electromagnetism. This analogy is further presented in Chapter 2.

1.4 General objectives

Hitherto, a general theoretical, historical introduction to the main concepts studied in this doctoral Thesis has been presented. Even though the beauty of the physical concepts studied and discussed is in itself worth it, this Thesis's usefulness is also linked with the actual or experimental applicability of those concepts. Indeed, part of the motivation of this Thesis relies on the existing interest and intense research on the topics addressed here, in both spintronics and nanophotonics fields. The combination of the original motivation presented in Sec. 1.3, the possible applicability, and research on the state-of-the-art published works allowed us to settle the main objectives of this Thesis. In particular, the general objectives undertaken during these four years are outlined below separately for the spintronics part, Sec. 1.4.1, and nanophotonics part, Sec. 1.4.2.

1.4.1 Spintronics

In addition to the charge, spintronics benefits from the additional electronic degree of freedom, the spin. One of the main branches of spintronics is the use of spin-orbit coupling to control the coupling between spin densities and currents by electric means, rather than external magnetic

fields [177, 166]. The coupling between the spin and the electron's momentum leads to the possible use of a charge current as a source of spin polarization, i.e., magnetoelectric effects without external magnetic fields. This all-electrical spin manipulation entails development possibilities in modern computing technologies based on writing, storing, and recovering information encoded as magnetic bits [42, 37, 177, 56, 170].

Two of the most studied magnetoelectric effects are those introduced in this chapter and further studied in Chapters 4 and 5: the spin Hall (SHE) and spin galvanic (SGE) effects. Spin generation at a given location and then spin transport between different locations are needed for the corresponding spin detection. On the one hand, this requires materials with large SOC for efficient charge-to-spin conversion and, on the other, with large enough spin diffusion lengths to transport the spin information across the device. The problem is, however, that strong SOC in a diffusive system will inevitably lead to a strong spin relaxation [48] as we further explain in Chapter 2.1. From an experimental perspective, we can tackle this problem by using hybrid structures combining different materials. For instance, we can combine one material with a strong SOC, in which the spin generation and manipulation occur, adjacent to another region with a weak SOC where the spin information can be transported over long distances. Another option is to combine two materials with weak SOC at whose shared interface an interfacial SOC is induced. Indeed, within state-of-the-art experimental research, hybrid devices for spin generation, manipulation, and detection based on SHE and SGE constitute a promising base for developing nonvolatile spin-orbit torque memories [111, 99, 135] and spin-based logic devices [127, 106, 107].

Consequently, a thorough theoretical description of these magnetoelectric effects is crucial for the development of spintronics devices. This, in addition to the necessity of a complete understanding of SOC effects, beyond single impurity scattering, in electronic transport, lead this Thesis to deviate from its original motivation, Sec. 1.3. Indeed, given the intense research activity in the field, the opportunity to contribute to understanding SOC in hybrid structures became one of the key objectives of this Thesis.

A widely used spintronics device is the so-called non-local lateral spin valve (see, e.g., Refs. [116, 91, 153, 83, 82]). This device can be seen as a modern-day upgraded version of the firstly proposed spintronic device for Rashba SOC measurements in a two-dimensional electron gas, the Datta-Das spin transistor [40]. We focus on lateral spin valves that can be described by diffusive electronic transport and with intrinsic linear-in-momentum SOC (see, e.g., [162, 134, 136, 62, 98, 18, 74, 89, 13]). Figure 1.5 illustrates a typical device combining a normal region, graphene in this case, and a central region with Rashba-like SOC, induced by deposition of a non-magnetic insulator on top of graphene, Bi_2O_3 in this case. By applying external electric currents, spin densities induced by magnetoelectric effects can be detected. In principle, the spin and charge transport in each region can be described with the well-known drift-diffusion model. However, sometimes it is not trivial to describe the spin-charge coupling within this framework. One of this Thesis's main objectives is the description of the boundary conditions right at the interface between normal and SOC regions. These boundary conditions are straightforward for the charge density and currents due to the principle of charge conservation: continuity at the interface. However, since the spin is not a conserved physical quantity, the corresponding boundary conditions have to be derived with care. This research line is followed in Chapter 4.

SOC can also be induced right at the interface between different non-magnetic materials. The magnetoelectric generation of the spin densities occurs at the interface. Such spin can then diffuses into the normal bulk conductors. In this case, different experimental devices are typically used for the measurements (see e.g. [85, 157, 97]). In this Thesis, we mainly focus on lateral spin valves (see e.g. [90, 80, 79, 158]) and multilayered Hall bars (see e.g. [138, 113]). Figure 1.6 illustrates these two devices. In both cases, the SOC particularly occurs at the interface between copper

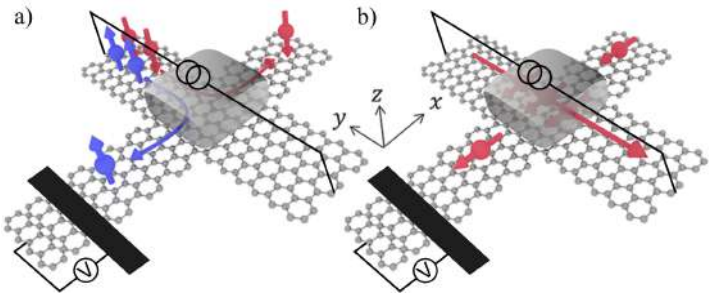

Fig. 1.5 Non-local measurements in graphene/Bi_2O_3 lateral spin valve. By applying an electric current in y direction, an out-of-plane polarized spin current is generated via SHE (a) and an in-plane homogeneous polarization is induced via EE (b). Both can be non-locally detected at, e.g., ferromagnetic detectors (black wires). Figure adapted from Ref. [136].

(Cu) and a non-magnetic insulator (BiO_x). Further details of these experimental devices can be found in Chapter 5. The other main objective of this Thesis is thus to give a complete and general formalism for quantifying the magnetoelectric effects at these heterostructures. This objective is also motivated by the possible description of the ISOC by effective boundary conditions at the interface, based only on symmetry arguments, predicted in Refs. [30, 5–7]. This other objective of the Thesis is addressed in Chapter 5.

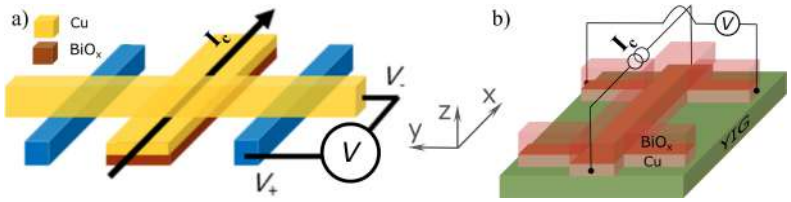

Fig. 1.6 Typical spintronics devices with ISOC, in this case with a Cu/BiO_x interface. (a) Lateral spin valve for non-local measurements at ferromagnetic wires (blue wire). Figure adapted from Ref. [80]. (b) Multilayered structure for spin Hall magnetoresistance measurements. Figure adapted from Chapter 5.

1.4.2 Nanophotonics

Light beams carrying AM have been applied to different branches of optics since the first observation of SAM transfer by Beth (1936) [22]. From this pioneer experiment, transfer of both OAM and SAM have been used for micromanipulation of optically trapped particles (see, e.g., [72, 144, 124, 104, 125]), new kinds of spectroscopy analysis, or information encoding for optical communications (see, e.g., [139, 169, 63]).

Specifically, this Thesis focuses on SOI arising in scattering problems [70, 27]. In this regard, a recent work has pointed out spin-orbit optical mirages as a possible source of optical localization errors when imaging emitters or scatterers [8]. As revised in Sec. 1.3, these SOI lead to a spiraling structure of the Poynting vector, which, in turn, traduces into apparent displacements of the order of the incident wavelength for particles behaving as electric dipoles. These optical mirages have a

direct consequence in the image of the scatterer at the detector's screen, as depicted in Fig. 1.7. Note that these localization errors can thus affect measurements of scatterers of any kind, such as electron wave scattering as shown in Sec. 1.3 or astronomical objects emitting gravitational waves [23].

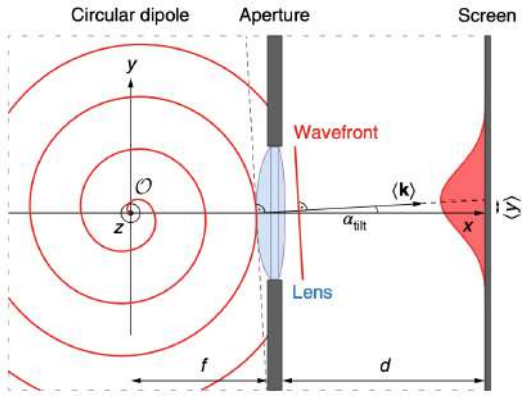

Fig. 1.7 The spiraling structure of the Poynting vector traduces in localization errors, $\langle y \rangle$, in far-field measurements at the screen of a hypothetical detector, with characteristic focal length, f Figure taken from [8].

These varied possible implications encouraged us to get some insight into the understanding of SAM and OAM and the possible interactions between them. Considering also the possible analogies with spintronics suggested in Sec. 1.3, the general objective of this Thesis was established. Namely, an in-depth analysis of SOC interactions in scattering problems when going beyond the pure electric dipolar regime—in other words, exploring possible effects of the interplay between electric *and* magnetic dipolar modes.

From the experimental perspective, we need thus scatterers with an electric and magnetic response under incident electromagnetic radiation. The electric permittivity of materials is in general different to that of the vacuum, $\varepsilon \neq \varepsilon_0$, and, therefore, materials have an effective electric response to light. However, for naturally occurring materials, the magnetic permittivity is always close to that of the vacuum, $\mu \simeq \mu_0$. This inevitably traduces in a negligible magnetic response in Nature at the wavelength range used in nanophotonics, i.e., on the nanometer scale, commonly referred to as optical range [35, 96].

In this regard, the generation of magnetic moments induced from the internal electric fields may be the solution. When a particle couples to an incident electric field, internal charge currents due to conducting electrons are directly generated. In insulating (or semiconducting) dielectric materials, an internal electric polarization may appear instead. In both cases, an effective magnetic moment is induced in the material through Maxwell-Ampère's law (1.10). In Chapter 2, we further explain how different electric modes or distributions induce different electric and magnetic moments (see Figure 2.5).

Within all the possible candidates, high refractive index (HRI) dielectric particles have received increasing interest during the past decade (see, e.g., [61, 95, 65, 15, 174, 29]). In contrast to metallic particles, dielectric particles do not present optical losses in the optical range. These losses can be understood since, according to Drude theory, losses within a metallic system are related to the scattering of moving electrons with impurities, phonons, etc. On the other hand, the unique optical properties of HRI nanoparticles are also linked with the excitation of single dipolar modes,

in contrast to low refractive index (LRI) dielectric particles. Figure 1.8 shows two examples of the scattering response efficiency of LRI and HRI spheres under plane wave illumination (for further details, see Chapter 2). The dipole and quadrupole modes barely have a structure for LRI particles. In contrast, HRI particles have well-defined, thinner resonances for each mode, and, therefore, we can work within a wide range of the spectra dominated by an electric and magnetic dipolar response.

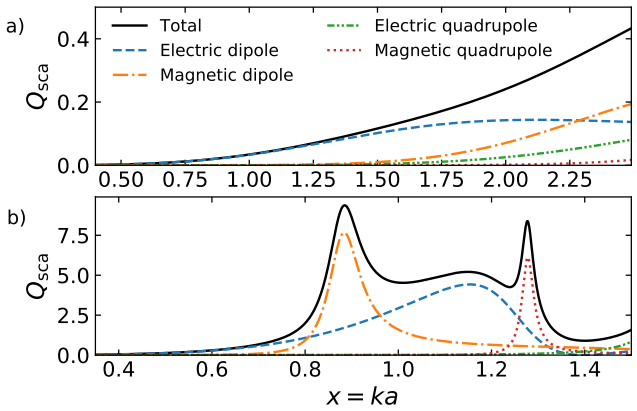

Fig. 1.8 Scattering efficiency of two spheres of radius $a = 230nm$ under plane wave illumination vs. the so-called size parameter $x = ka$, with $k = 2\pi/\lambda$ and λ the incident wavelength. Namely, we show a LRI particle with refractive index $m = 1.2$ (a) and a HRI particle with $m = 3.4$ (b). Dipolar and quadrupolar contributions to the total efficiency are also included, particularly well-defined in panel (b).

Furthermore, due to the interplay between electric and magnetic responses, light's strong directionality may be achieved under certain circumstances. This effect was theoretically predicted by Kerker et al. (1983) [88] for magnetodielectric spheres, i.e., spheres with $\mu \neq \mu_0$. The so-called first, $\varepsilon = \mu$, and second, $\varepsilon = (4-\mu)/(2\mu+1)$, Kerker conditions correspond to suppression of the scattered light in backward and forward directions, respectively. Kerker conditions, firstly quoted as anomalous light-scattering conditions, remained largely overlooked due to the lack of a fundamental explanation. The latter arrived roughly thirty years later by Fernandez-Corbaton et al. (2012) [57], with the aid of a light non-geometrical symmetry, duality symmetry [36], generalized for scattering problems. This work demonstrated that the first and second Kerker conditions correspond, respectively, to dual and antidual scatterers for which the incident helicity is conserved or completely reversed after scattering [57, 175] [1]. As previously suggested, Kerker conditions and duality restoration phenomena can be generalized for non-magnetic scatterers, namely, HRI spheres in the dipolar regime. This generalization was firstly done by Nieto-Vesperinas et al. (2011) [115] in their work entitled "*Angle-suppressed scattering and optical forces on submicrometer dielectric particles*". As a result of these theoretical analyses, different applications were studied. Particularly, full control of the scattering directionality can be useful for multiple applications, such as light trapping applications or improving solar cells' performance (see, e.g., [15, 163, 142, 16]).

[1] The helicity arises from the projection of the SAM onto the linear momentum of the wave and, in far-field, the helicity density correspond to the degree of circular polarization of the scattered waves, as further reviewed in Chapter 2.

Based on all these previous research works and the possible applications, we further specified the details of the main objective of the nanophotonics part of this Thesis. Namely, the study of the spin-orbit optical mirages arising from the scattering of a HRI particle with an electric and magnetic dipolar response. It is addressed in Chapter 6, whereas Chapter 7 arise as a natural consequence of the previous work, focusing on the possibility of describing SOI in the dipolar regime from scattering symmetry considerations.

Chapter 2

Models, methods, and results

The fundamental equations behind the two main topics of this Thesis are the Schrödinger and Maxwell's equations. The wave function describing the electron in spintronics and the electric and magnetic fields in photonics can be obtained from them. Besides, charge conservation, implicit in both theories, is described by the continuity equation:

$$\frac{\partial \rho}{\partial t} = -\partial_k j_k \,, \tag{2.1}$$

where j_k is the k-th component of the charge current density $\mathbf{J}$. Equation (2.1) illustrates the physical fact that any variation of the charge density ρ at some small volume in a certain time must correspond to a flow of charge or charge current density $\mathbf{J}$ in- or outgoing through the volume surface.

There are different contributions to the current in Eq. (2.1). For example, in analyzing light-matter interactions, the incident electric field generates a (drift) charge current inside the target which, in turn, scatters light, i.e., $\mathbf{J} \propto \mathbf{E}^{\text{int}}$, with $\mathbf{E}^{\text{int}}$ the electric field induced inside the volume. Another example: when studying electron transport in metals additional contributions to the charge current appears such as diffusive currents, as explained later in this chapter.

In electrodynamics problems, the charge and current densities are the electromagnetic fields' sources, whereas, in electronics and spintronics, one usually assumes a given external electromagnetic field and compute the densities. In both situations, it is convenient to introduce the vector, $\mathbf{A}$, and scalar, ϕ, potentials to describe the electromagnetic fields. Specifically, for the present Thesis, the introduction of these potentials simplifies the relationship between sources and fields in Maxwell's equations. As a matter of fact, a direct relation can be obtained between the gauge fields and sources, i.e., $\mathbf{J}$ as the source of $\mathbf{A}$ and ρ as the source of ϕ (see Eq. (2.3)). It is also customary to introduce the electromagnetic fields in the Hamiltonian via the scalar and vector potentials in the study of quantum transport. This results in a displacement in the linear momentum of the electron and potential energy (see Eq. (2.6)). Interestingly, the linear-in-momentum SOC term in the Hamiltonian of Eq. (2.7) can be written in the Hamiltonian as a non-abelian (or non-commutative) vector potential, describing an effective background SU(2) electromagnetic field. As we discuss in this chapter, this representation has several advantages and provides an interesting connection between charge and spin-related phenomena.

Let us start reviewing the electromagnetic potentials in the U(1) case. From the Gauss' law, Eq. (1.8), the magnetic induction $\mathbf{B}$ can always be expressed as the rotational of a vector potential,

namely, $\mathbf{B} = \boldsymbol{\nabla} \times \mathbf{A}$. By combining this expression with Faraday's law, Eq. (1.9), the electric field can be expressed as $\mathbf{E} = -\boldsymbol{\nabla}\phi - \partial_t \mathbf{A}$. It is useful to define a four-potential and four-derivative as $\mathbf{A}^0 = (A_0^0, A_x^0, A_y^0, A_z^0) = (\phi/c, \mathbf{A})$ and $\boldsymbol{\partial} = (\partial_0, \partial_x, \partial_y, \partial_z) = (-\partial_t/c, \boldsymbol{\nabla})$, respectively. From that, we can construct a field tensor as $\mathbf{F}^0$ and each of the components of the electric and magnetic fields can be calculated from the field tensor components as follows:

$$F_{\mu\nu}^0 = \partial_\mu A_\nu^0 - \partial_\nu A_\mu^0 \quad \longrightarrow \quad B_i = \frac{1}{2}\varepsilon_{ijk} F_{jk}^0 \,, \quad E_i = c F_{0i}^0 \tag{2.2}$$

where Greek letters run over $(0, x, y, z)$, Latin letters run over the cartesian components (x, y, z), following Einstein summation criteria. Including these expressions in the inhomogeneous Maxwell's equations, Eqs. (1.7) and (1.10), reduces the set of four equations to a second order equation for the four-potential. Specifically using the Lorenz gauge [1], the following wave equation is obtained [81]:

$$\Box A_\nu^0 = \left(\boldsymbol{\nabla}^2 - \frac{1}{c^2}\partial_t^2\right) A_\nu^0 = J_\nu^0 \,, \tag{2.3}$$

where $\mathbf{J}^0 = -(\rho/\varepsilon_0, \mu_0 \mathbf{J})$ is the four-current and $\Box$ is the d'Alembert operator. In Eq. (2.3), the scalar potential depends only on static charge distributions, whereas the vector potential depends only on currents. If harmonic time-dependence, $e^{-\mathrm{i}\omega t}$, is assumed, the previous equation simplifies to a inhomogeneous Helmholtz equation, i.e., the d'Alembert operator reduces to $\Box = \partial_k \partial_k + k^2$, with the dispersion relation $\omega = kc$. The solution of Eq. (2.3) can be therefore expressed as follows:

$$A_\nu^0 = -\int_{V'} G J_\nu^0 = -\int_{V'} \frac{e^{\mathrm{i}k|\mathbf{r}-\mathbf{r}'|}}{|\mathbf{r}-\mathbf{r}'|} J_\nu^0(\mathbf{r}')\, dV' \,, \tag{2.4}$$

where G is the Green's function for the Helmholtz operator and $\mathbf{J}^0$ the source function. In the part on photonics of this Thesis, where single scattering processes are analyzed, the charge distributions excited by the incident radiation are enclosed inside the particle's volume. Therefore, the scattered electromagnetic fields are calculated from Eq. (2.4) with V being the scatterer's volume. In Sec. 2.3, the advantage of performing a *multipole* expansion of the previous equation is presented. In this Taylor expansion in cartesian coordinates, the scattered fields can be calculated as those generated by the infinite sum of the multipolar expansion: electric and magnetic dipoles, quadrupoles, octopoles, and so on.

We now turn our attention to the other main topic of this Thesis: spin transport in systems with SOC. In electronic systems, we study how the external electromagnetic fields affect the system via the Lorentz force:

$$F_k = qE_k + q\frac{p_i B_j \varepsilon_{ijk}}{m} \,. \tag{2.5}$$

The first term corresponds to the drift force, whereas the second term is the cause of the Hall effect [71], illustrated in Fig. 2.1. In this figure, we show a two-dimensional conductor, e.g., in the x–y plane, in an external magnetic field perpendicular to it, e.g., in the z direction. If a charge current $\mathbf{j}_c$ is applied in, e.g. y direction, the particles with charge q will be deflected to opposite directions via the Lorentz force depending on the sign of the charge, $F_x = q p_y B_z / m$.

The response of the electrons described in Eq. (2.5) is usually included in the Hamiltonian through the gauge fields $\mathbf{A^0}$ and ϕ using the minimal coupling. This well-known transformation is done under U(1)-covariant formalism, which implies that all physical results must be invariant

[1] Considering a gauge-transformation is made to the potentials, $A_\nu^0 \to A_\nu^0 + \partial_\nu f$, the Lorenz gauge is the gauge in which the four-potential satisfies the Lorenz condition, $\partial_\mu A_\mu^0 = 0$, and $\partial_\mu \partial_\mu f = 0$.

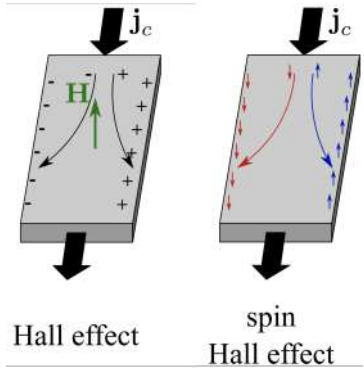

Fig. 2.1 Caption

under local U(1) transformations. In this formalism, the (gauge-invariant) kinetic momentum also takes account of the effect of the external magnetic field and, therefore, the Hamiltonian reads:

$$H = \frac{(p_k - eA_k^0)^2}{2m} - eA_0^0 \,, \tag{2.6}$$

where the SOC term is not yet introduced. In this regard, as mentioned in Chapter 1, part of the theoretical work presented in this Thesis is related to intrinsic SOC as it appears in Eq. (1.5). The focus is on linear-in-momentum intrinsic SOC, related to two-dimensional transport, since an interesting analogy with the four-vector notation can be found. In general, the effective magnetic field of Eq. (1.5) can be expressed for linear-in-momentum SOC as $\Omega^a(\mathbf{p}) = \mathscr{A}_k^a p_k/m$, with $\hat{\mathscr{A}}_k$ a spin-structured vector potential. Equation (1.5) can be thus written as:

$$H = \frac{p_k p_k}{2m} + \frac{\mathscr{A}_k^a p_k \sigma^a}{2m} \,, \tag{2.7}$$

which up to a constant factor can be rewritten as:

$$H = \frac{(p_k - \hat{\mathscr{A}}_k)^2}{2m} - \hat{\mathscr{A}}_0 \,, \tag{2.8}$$

We have added a second term, which stands for the other possible linear coupling with the electron's spin, i.e., a Zeeman or exchange field with the generic form of Eq. (1.1). In Eq. (2.8), the components of the scalar and vector potentials are expressed in terms of Pauli matrices, $\hat{\mathscr{A}}_k = \frac{1}{2}\mathscr{A}_k^a \sigma^a$ and $\hat{\mathscr{A}}_0 = \frac{1}{2}\mathscr{A}_0^a \sigma^a$, and therefore are non-commutative. We recall that lower indices correspond to spatial coordinates and upper indices to spin components in our notation. In analogy with usual U(1) fields, the SU(2)-four-potential notation yields a field SU(2)-tensor from which the electric and magnetic SU(2)-fields can be constructed (cf. Eq. (2.2)):

$$\mathscr{F}_{\mu\nu}^a = \tilde{\partial}_\mu \mathscr{A}_\nu^a - \tilde{\partial}_\nu \mathscr{A}_\mu^a \quad \longrightarrow \quad \mathscr{B}_i^a = \frac{1}{2}\varepsilon_{ijk}\mathscr{F}_{jk}^a \,, \quad \mathscr{E}_i^a = c\mathscr{F}_{0i}^a \,, \tag{2.9}$$

where the four-derivative becomes SU(2)-covariant, with $\tilde{\partial}_t = \partial_t - \mathrm{i}\hbar^{-1}[\hat{\mathscr{A}}_0, \cdot]$ and $\tilde{\partial}_k = \partial_k - \mathrm{i}\hbar^{-1}[\hat{\mathscr{A}}_k, \cdot]$. Within this formalism, the intrinsic SOC can be thus understood as an effective SU(2) electromagnetic field affecting the charge and spin transport. Namely, the SU(2) analogous to the

Lorentz force of Eq. (2.5) is defined as:

$$\hat{F}_k = \hat{\mathscr{E}}_k + \frac{p_i \hat{\mathscr{B}}_j \varepsilon_{ijk}}{m} \,. \tag{2.10}$$

where the first term correspond to the SU(2) drift term and the second is the cause of the spin Hall effect (SHE). Similarly to the charge-dependent deflection in the Hall effect, the SHE is the asymmetric deflection of opposite spins, as shown in Fig. 2.1. In that figure, we assume a particular example of the SHE for simplicity, namely, a two-dimensional system in the x–y plane with Rashba SOC. By comparison between Eq. (1.6) and (2.7), Rashba SOC corresponds to $\mathscr{A}_y^x = -\mathscr{A}_x^y = 2m\alpha$. If α is spatially homogeneous, only the covariant terms contribute to $\mathscr{F}_{\mu\nu}^a$ and $\mathscr{B}_i^a$. Namely, Rashba SOC induces an effective SU(2) magnetic field $\mathscr{B}_z^z$. Consequently, if a charge current $\mathbf{j}_c$ is applied in y direction, the eigenstates of σ^z will be deflected to opposite directions via the SU(2) Lorentz force depending on the direction of the spin, $F_x^z = p_y B_z^z/m$. In electronic transport, this asymmetry traduces in the generation of a transversal spin current.

Interestingly, the above SU(2) formulation allows writing a SU(2)-covariant continuity equation for the spin [155]. In other words, within this formalism the spin is covariantly conserved when only intrinsic linear-in-momentum SOC is considered. The corresponding spin continuity equation reads:

$$\tilde{\partial}_t \hat{S} + \tilde{\partial}_k \hat{j}_k = 0 \,, \tag{2.11}$$

where $\hat{S} = S^a(\sigma^a/2)$ is the spin density and $\hat{j}_k = j_k^a(\sigma^a/2)$ is the spin current density flowing in k-direction, defined as the average of the spin current operator, $j_k^a = (1/2)\{\partial H/\partial p_k, \sigma^a/2\}$. In this formulation, the spin and charge continuity equations have the same form as Eq. (2.1), but with the derivatives substituted by the covariant ones. Since the charge density and current have no spin structure, $\tilde{\partial}_t \rho = \partial_t \rho$ and $\tilde{\partial}_k \rho = \partial_k \rho$. The charge continuity equation, therefore, is identical to Eq. (2.1). In contrast, the covariant term of the derivatives acts on the spin density and current, describing the possible spin relaxation. In particular, as it can be read out from Eq. (2.11), the relaxation in a system with intrinsic SOC is due to the SOC itself. We study this in more detail in the next section.

In summary, by writing the electromagnetic and spin-dependent fields in terms of vector and scalar potentials, an excellent analogy arises between two hitherto unconnected fields: spintronics and photonics. In the next sections, we review details of the models and methods applied in the two parts of this Thesis and a summary of the main results. This is done in Secs. 2.1 and 2.2 for spintronics, and in in Secs. 2.3 and 2.4 for photonics.

2.1 Spintronics: models and methods

In this section, we review the main concepts in the field of spintronics which are behind the main results presented in the two published works, Chapters 4 and 5. We begin with a general description of the spin-charge transport phenomena in materials with SOC. In subsequent sections, we address more specific scenarios and summarize the main results in Secs. 2.2.1 and 2.2.2. The complete works are provided in Chapters 4 and 5.

Spintronics is the study of electronic transport associated with the electronic spin. In particular, systems with SOC exhibit coupling between the charge and spin degrees of freedom. Whereas the charge conservation principle is always fulfilled, spin relaxation may occur, i.e., the disappearance of initial non-equilibrium spin polarization. Charge conservation and spin relaxation constitute the physical bases for all the spintronics effects.

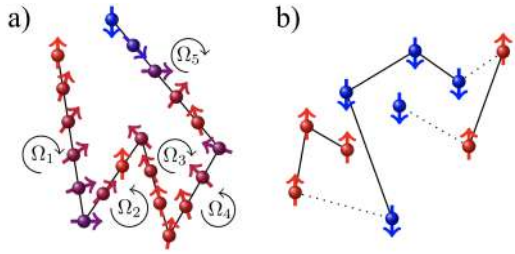

Fig. 2.2 Dyakonov-Perel (a) and extrinsic (b) spin relaxation mechanisms. In both cases, after a certain number of such steps, the initial spin direction is completely lost. This figure is taken from Ref. [32].

There are different mechanisms responsible for the spin relaxation [50]: spin-orbital (Dyakonov-Perel and Elliott-Yafet), magnetic impurities, electron-hole spin-exchange interaction (Bir-Aronov-Pikus) [24], hyperfine interaction with nuclear spins, and spin relaxation of holes in the valance band [47]. In this Thesis, specifically in Chapter 4, we focus on spin relaxation due to the Dyakonov-Perel and Elliott-Yafet mechanisms and from extrinsic magnetic impurities.

The Dyakonov–Perel (DP) mechanism is an intrinsic mechanism of spin relaxation [48, 51, 52]. It arises when intrinsic SOC is present in the system, which is described by Eq. (1.5) or (2.8), and it is related to the spin-orbit splitting of the conduction band in non-centrosymmetric systems. The splitting acts on the electrons as if an effective momentum-dependent magnetic field would be present at the whole system. Figure 2.2(a) illustrates the DP mechanism: the electron's spin precesses around the magnetic field vector, $\Omega^a(\mathrm{p})$ in Eq. (1.5), which changes after each collision due to the change in momentum direction. Accordingly, the spin polarization changes not during, but *between* collisions. If the scattering rate is such that electrons scatter before they can complete a single precession about the SU(2) effective magnetic field, the DP mechanism becomes inoperative. Therefore, the DP mechanism influence is stronger in systems with lower impurity concentrations [50].

In systems with an extrinsic SOC source (see Sec. 1.1), as SOC impurities, the so-called Elliott–Yafet (EY) mechanism is the main spin relaxation mechanism[55, 171]. This effect can be thus present in all conductors without any symmetry restriction. EY mechanism is illustrated in Fig. 2.2(b): when the electron collides with some impurity, beside the change in momentum direction, the spin polarization can change if there is SOC between the electrons spin and the impurity. The accumulated effect traduces in spin relaxation, and the corresponding relaxation rate is, in this case, proportional to the impurity concentration.

Similarly to the EY mechanism, scattering from extrinsic magnetic impurities leads to a change in both momentum direction and spin polarization, see Fig. 2.2(b). We refer to both EY and scattering from magnetic impurities as extrinsic spin relaxation (ESR). In isotropic systems, both mechanisms can be described by an effective relaxation time τ_{ext}.

The effect of the DP and ESR mechanisms in the spin transport must be included in the spin continuity equations [132, 75, 141]. Equation (2.11) already includes the DP relaxation via the covariant derivatives, and the spin is covariantly (but not actually!) conserved. In the presence of any kind of ESR, Eq. (2.11) acquires an additional term:

$$\tilde{\partial}_t \hat{S} + \tilde{\partial}_k \hat{j}_k = -\frac{1}{\tau_{\mathrm{ext}}} \hat{S} \,. \tag{2.12}$$

Here, we assume that the spin relaxation is isotropic in space and neglect the interference term between extrinsic and intrinsic SOC [68]. The right-hand side of this equation clearly shows that the ESR breaks the SU(2) symmetry and, hence, the spin is no longer covariantly conserved.

We now focus on the systems analyzed in detail in this Thesis. Measuring the SOC related effects in spintronics devices usually involves transporting electron spins between different locations [177, 166, 105, 148]. However, strong SOC translates into strong spin relaxation via the DP and ESR mechanisms. Consequently, it is customary to use hybrid spintronics devices, combining a region with strong SOC in which the spin is manipulated and a normal region in which the spin is transported. Figure 2.3 shows typical heterostructures. Panels (a, b) correspond to structures with Rashba SOC studied in Chapter 4. Panel (c) shows a conductor/insulator system with SOC at the

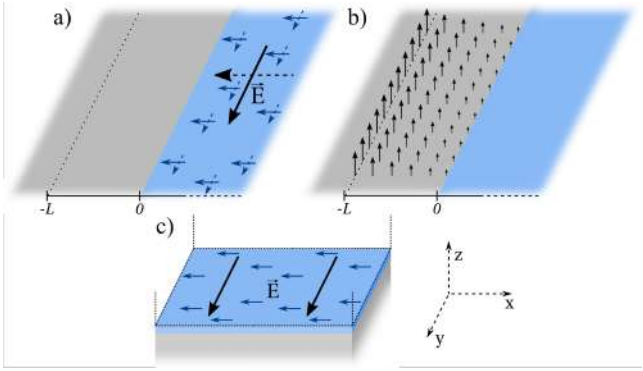

Fig. 2.3 Schematical view of different setups considered in this Thesis. (a,b) Adjacent Rashba (blue region) and normal (grey region) semi-infinite systems in which the ISGE (a) and the SGE (b) are studied in Chapter 4. (c) Heterostructure with a localized SOC at the interface (blue region) between a normal conductor (grey bottom region) and an insulator (transparent top region). This system is addressed in Chapter 5.

interface, studied in Chapter 5 (c). At the interface between different materials, we need to supply the charge and spin continuity equations, Eqs. (2.1) and (2.12), with boundary conditions (BC). Specifically, we study two type of systems: Chapter 4 focuses in adjacent two-dimensional conductors with different linear-in-momentum intrinsic SOC, whereas Chapter 5 deals with adjacent bulk normal (i.e., without SOC) systems at which interfacial SOC (ISOC) is induced. As further explained in Sec. 2.1.2, at interfaces between different materials, the strong inversion symmetry breaking may lead to spin-splitting of the (possible) interfacial states. In addition, there exist the possibility of a mixing region near the interface, leading to SOC impurity scattering. Independently of the source of SOC, the BC at such interfaces can be written in terms of a set of interfacial parameters obtained from symmetry considerations [30, 5–7].

In both, Chapters 4 and 5, we assume that the conductors are in the diffusive limit. In this regime, the electrons' mean free path is much smaller than any other characteristic length scale, as the system's spin diffusion length or dimensions. Therefore, charge and spin densities follow the well-known drift-diffusion equations [50, 141, 67, 155, 156, 129]. The drift-diffusion model for systems with intrinsic linear-in-momentum SOC is reviewed in Sec. 2.1.1 within the SU(2) formalism, including the possible presence of ESR. Besides, we present the needed BC at the interface between two-dimensional systems with different linear-in-momentum SOC, derived in Chapter 4.

On the other hand, in Chapter 5, we apply the drift-diffusion model at the normal bulks. Because we consider interfacial SOC, different BC are needed [30]. The specific model is discussed in Sec. 2.1.2.

Finally, in Secs. 2.2.1 and 2.2.2, we summarize the main results of the works compiled as Chapters 4 and 5, respectively.

2.1.1 Hybrid systems with linear-in-momentum SOC: drift-diffusion theory within the SU(2) formalism

Electronic transport in conductors is usually studied within the free-electron model [147, 45, 46, 12]. Transport properties are characterized by the mean free path of the electrons, $\ell = v_{\rm F}\tau$, with $v_{\rm F}$ the Fermi velocity and τ the momentum relaxation time. Depending on the ratio between the mean free path and the other characteristic lengths, such as the dimensions or the spin relaxation lengths, one distinguishes between ballistic or diffusive electronic transport. Here, we focus on the diffusive regime.

Derivation of drift-diffusion theory in systems with SOC is extensively analyzed in the literature [67, 66, 156, 94, 141, 50]. Therefore, here we limit ourselves to provide a brief review.

In a diffusive system, the charge current is given by [66, 156, 141]:

$$j_k = -D\partial_k\rho - \sigma_{\rm D}E_k - \gamma\mathscr{F}^a_{ki}j^a_i \,, \tag{2.13}$$

where $\sigma_{\rm D}$ the Drude conductivity and E_k the k-th component of the electric field. The first term is the diffusion term, where $D = v_{\rm F}^2\tau/d$ is the diffusion coefficient, and d the dimension of the system. The third term, where $\gamma = \tau/(2m)$ and proportional to the spin current density j^a_i, describes the spin-to-charge conversion via the inverse SHE (ISHE), i.e., the inverse to the effect shown in Fig. 2.1. The proportionality factor contains the field strength tensor defined in Eq. (2.9). On the other hand, the spin current density in the diffusive limit is given by [66, 156, 141]:

$$\hat{j}_k = -D\tilde{\partial}_k\hat{S} - \gamma\hat{\mathscr{F}}_{ki}j_i \,. \tag{2.14}$$

The first term corresponds to the SU(2)-covariant spin counterpart of the first term of Eq. (2.13). The second term is the reciprocal to the second term in Eq. (2.14). It describes the charge-to-spin conversion under the action of the SU(2) field and, therefore, is related to the SHE, see Fig. 2.1.

Once we have the expressions for the currents, Eqs. (2.13) and (2.14), the charge and spin continuity equations can be obtained. We focus here in the *stationary* case and assume the absence of a Zeeman field, i.e., $\tilde{\partial}_t\rho = \partial_t\rho = 0$ and $\tilde{\partial}_t\hat{S} = 0$. Therefore, the charge and spin drift-diffusion equations have, respectively, the following form:

$$\tilde{\partial}_k j_k = \partial_k j_k = 0 \quad \longrightarrow \quad \partial_k D\partial_k\rho + \partial_k(\sigma_{\rm D}E_k) + \gamma(\tilde{\partial}_k\hat{\mathscr{F}}_{ki})^a j^a_i = 0 \,, \tag{2.15}$$

$$(\tilde{\partial}_k\hat{j}_k)^a = -\frac{S^a}{\tau_{\rm ext}} \quad \longrightarrow \quad \tilde{\partial}_k D\tilde{\partial}_k S^a + \gamma(\tilde{\partial}_k\hat{\mathscr{F}}_{ki})^a j_i = \frac{S^a}{\tau_{\rm ext}} \,. \tag{2.16}$$

The second term in Eq. (2.15) vanishes for spatially homogeneous conductivity and electric field, case that is considered in this Thesis. The covariant Laplace operator of Eq. (2.16) can be written explicitly by expanding the covariant derivatives [20]:

$$(\tilde{\partial}_k D\tilde{\partial}_k)^{ab} = \partial_k D\partial_k\delta^{ab} + 2P^{ab}_k\partial_k + \partial_k P^{ab}_k - \Gamma^{ab} \,, \tag{2.17}$$

where we define the following operators:

$$\Gamma^{ab} = D[\hat{\mathscr{A}}_k, [\hat{\mathscr{A}}_k, \cdot]] = -D^{-1} P_k^{ac} P_k^{cb} , \tag{2.18}$$

$$P_k^{ab} = -iD[\hat{\mathscr{A}}_k, \cdot] = D\mathscr{A}_k^c \varepsilon^{cba} . \tag{2.19}$$

Here, Γ^{ab} is the general DP relaxation tensor that describes the DP spin relaxation reviewed in the introduction of Sec. 2.1, whereas the term proportional to P_k^{ab} in Eq. (2.16) describes the spin precession [112, 20].

As explained in the introduction, Sec. 1.1, linear-in-momentum SOC arises in systems with a gyrotropic symmetry, e.g., two-dimensional electron gases. In such systems, the asymmetry in one of the directions, e.g., z direction, traduces in a SOC that affects the two-dimensional transport in the perpendicular directions, e.g., x and y directions. In addition to the SHE shown in Fig. 2.1, this lack of symmetry allows for another type of magnetoelectric effects, namely, the spin galvanic effects (SGE). As mentioned in Sec. 1.1, SGE and its inverse (ISGE) are related to the interconversion between charge current and spin density, in contrast to SHE and ISHE, relating charge current and spin current.

Accordingly, we can homogeneously polarize a system by applying an external charge current via the ISGE. This effect can be easily derived from the drift-diffusion equation in an isotropic system. Indeed, let us assume an infinite plane with generic linear-in-momentum SOC and without ESR. If a charge current flows in i direction (induced by an applied electric field), according to Eq. (2.16):

$$-\Gamma^{ab} S^b + \gamma \mathscr{A}_k^b \mathscr{F}_{ki}^c \varepsilon^{bca} j_i = 0 . \tag{2.20}$$

This equation predicts the appearance of a homogeneous spin density, proportional to the external electric field. In the particular case of the widely studied Rashba SOC of Eq. (1.6), in which the focus is on in Chapter 4, this effect is commonly known as Edelstein effect (EE). The latter is illustrated in Fig. 2.3(a): a (in-plane) homogeneous spin polarization is induced perpendicular to the (in-plane) external electric field. If we introduce this spatially homogeneous result into Eq. (2.14), a compensation between covariant diffusive and the charge-to-spin conversion terms leads to $\hat{j}_k = 0$, i.e., no spin Hall currents appear. However, as further explained in Chapter 4, if we take into account ESR, the SU(2)-covariant spin conservation is broken, yielding finite spin currents.

Therefore, the ISGE can be used as a useful spin injection tool from SOC regions to normal systems in spintronics devices, merely applying an external charge current. This possible injection is deeply analyzed in Chapter 4, for which we develop the needed BC at the interface between different regions.

Boundary conditions

Here, we briefly review the BC derived in Chapter 4 for two-dimensional spintronics hybrid devices with an interface between two regions with different linear-in-momentum SOC. These BC are obtained by integrating the drift-diffusion equations over an infinitesimal region across the interface.

On the one hand, the spin current's continuity across the interface is obtained by integration of the spin continuity equation [33, 1, 159]. This result can be naively understood since we assume that the interface is much smaller than the spin diffusion length of either of the adjacent systems. Hence, the SOC "does not have enough space" to relax or change the spin.

On the other hand, the BC for the spin density is obtained integrating the spin current, Eq. (2.14), across the interface, taking into account the continuity of the current. This integration leads

to the continuity of the spin density when no external electric field is applied. However, a electric field applied parallel to the interface yields a jump across the interface of the spin density induced at the SOC region via the ISGE. The explicit form of this BC is:

$$S^a\big|_{0^-}^{0^+} = \frac{1}{2}\left(\frac{\gamma\sigma_{\rm D}}{D}\Big|_{0^+} + \frac{\gamma\sigma_{\rm D}}{D}\Big|_{0^-}\right)(\delta_{ij} - n_i n_j)\left(\mathscr{A}_j^a|_{0^+} - \mathscr{A}_j^a|_{0^-}\right)E_i \,. \tag{2.21}$$

This is one of the main results of Chapter 4, which generalizes previous results for any strength and type of linear-in-momentum SOC at the adjacent regions.

This BC can be physically understood as follows. Let us assume that the heterostructure consists of a normal and a Rashba adjacent two-dimensional regions, as in Fig. 2.3(a). We can thus describe the system with $\mathscr{A}_y^x = -\mathscr{A}_x^y \approx 2m\alpha\Theta(x)$. If we apply an electric field in y direction, an homogeneous spin density polarized in x direction will be induced at the Rashba region via the ISGE (see Eq. (2.20)). At the interface, the Rashba coefficient α abruptly becomes zero and, therefore, a SU(2) field tensor and corresponding magnetic field appear with form $\mathscr{F}_{xy}^x = -\mathscr{F}_{yx}^x = \partial_x \mathscr{A}_y^x \approx 2m\alpha\delta(x)$ and $\mathscr{B}_z^x = 2m\alpha\delta(x)$. Therefore, right at the interface, an effective magnetic field in z direction deflects the x-polarized spins, that are moving parallel to the electric field, via the SU(2) Lorentz force, $F_x^x = p_y B_z^x/m$ (see Eq. (2.10)). This force in x direction prevents the spin density from diffusing into the normal region [159].

2.1.2 Hybrid conductor/insulator systems with interfacial SOC: drift-diffusion theory with generalized boundary conditions

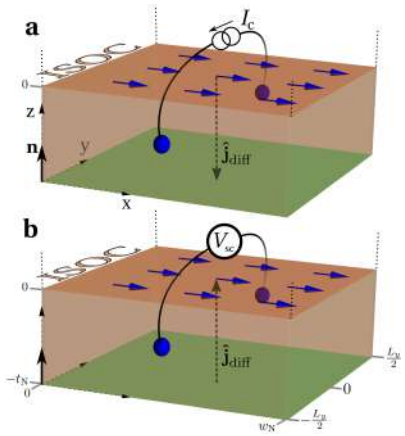

Fig. 2.4 Caption

In this section, we review the model and methods used in Chapter 5. The non-magnetic hybrid devices described here consist of two normal diffusive bulk materials: a conductor (N) and an insulator (I). Figure 2.4 depicts this kind of system. The N bulk is located at $z < 0$, the insulator at $z > 0$, and the ISOC is induced at $z = 0$.

In the N layer, the spin and charge densities follow the drift-diffusion equations (2.15) and (2.16) for the normal case, i.e., when the SU(2) vector potential is zero. Since in Chapter 5, we calculate voltage drops in different spintronics devices, it is convenient to use charge and spin electrochemical potentials (ECP), in energy units, rather than spin and charge densities, in units of

charge per unit volume. Substituting $D\rho = e^{-1}\sigma_D\mu$ and $D\hat{S} = e^{-1}\sigma_D\hat{\mu}$ in Eqs. (2.15) and (2.16), with μ and $\hat{\mu}$ the charge and spin ECP, yields:

$$\partial_k\partial_k\mu = 0\,, \tag{2.22}$$

$$\partial_k\partial_k\hat{\mu} = \frac{\hat{\mu}}{\lambda_N^2}\,. \tag{2.23}$$

It is assumed that N has inversion symmetry with an isotropic ESR [167] described by the spin diffusion length $\lambda_N = \sqrt{D\tau_{ext}}$. The diffusive charge and spin currents, Eqs. (2.13) and (2.14), are reduced to $e\hat{j}_k = -\sigma_D\partial_k\hat{\mu}$ and $ej_k = -\sigma_D\partial_k\mu$, respectively, with $e = -|e|$.

As explained in the previous section, Chapter 4 addresses heterostructures in which the SOC is present at the adjacent diffusive systems. In contrast, the interfacial SOC (ISOC) studied in Chapter 5 occurs right at the interface, i.e., at microscopic scales much smaller than the mean free path of the electrons. Therefore, the inclusion of the interconversion between the (diffusive) bulk and interfacial densities is kind of subtle within the drift-diffusion model. Some works use an intuitive picture based on an idealized two-dimensional electron gas with Rashba SOC at the interface [90, 113, 157]. Such description is valid for systems in which an evident two-dimensional electronic transport is present, such as conductive surface states in (e.g. topological) insulators [133, 93] or two-dimensional electron gases [97, 165]. However, it requires additional microscopic parameters to model the coupling between interface states and the diffusive motion of electrons in the metal in metallic systems. Moreover, the very fact that the SOC induced at the interface has an intrinsic origin only may be senseless since realistic structures are frequently polycrystalline and disordered. In this regard, one could also contemplate the possibility of an extrinsic origin. For instance, the insulating material's heavy atoms could have diffused into the normal conductor in the region near the interface, acting on the electrons as extrinsic SOC impurities. Indeed, each of these scenarios will invoke different sets of microscopic parameters to be inferred from the experiments, i.e., macroscopic transport measurements.

Here, we present the solution proposed in Chapter 5 to this problem: inclusion of the ISOC effects as effective BC at the interface between the adjacent systems without SOC. These BC are derived [5–7] and generalized for non-magnetic hybrid normal systems with ISOC in Ref. [30]. The latter reference approaches the ISOC from a phenomenological perspective since all the SOC effects can be derived from pure symmetry considerations. In an isotropic bulk media with inversion symmetry, the only building block is the unit antisymmetric tensor ε_{ijk}, describing the SHE due to effective Lorentz forces acting on the spins [50]. For lower symmetries, as the interfaces considered here, other tensors appear related to all possible SOC effects, e.g., the intrinsic SHE or SGE. Figure summarizes the SOC effects that we take account of. Namely, we consider interconversion between spin (charge) bulk and charge (spin) interfacial currents via an interfacial ISHE (SHE), interconversion between interfacial spin polarization and charge current via ISGE and SGE, and, implicitly, the possible spin relaxation or loss at the interface. This symmetry-based formalism is useful to quantify ISOC effects from experimental measurements, avoiding a rather troublesome microscopic analysis.

Namely, for the I/N system considered here (see Fig. 2.4), Eqs. (2.23) and (2.22) are complemented by the following BCs for the spin and charge densities at the I/N interface with ISOC [30]:

$$-\sigma_D(\nabla\cdot\mathbf{n})\hat{\mu}\big|_0 = G_\perp\,\hat{\mu}_\perp\big|_0 + G_\parallel\,\hat{\mu}_\parallel\big|_0 + \sigma_{cs}\,(\mathbf{n}\times\nabla)\,\mu\big|_0\,, \tag{2.24}$$

$$-\sigma_D(\nabla\cdot\mathbf{n})\mu\big|_0 = \sigma_{sc}\,(\mathbf{n}\times\nabla)\,\hat{\mu}\big|_0\,. \tag{2.25}$$

Here, $\mathbf{n}$ is the unitary vector normal to the interface, see Fig. 2.4a, and σ_D the conductivity of N. The last term in the r.h.s. of Eq. (2.24), describes the charge-to-spin conversion quantified by the conductivity σ_{cs}. As depicted in Fig. 2.4a, this term couples an effective electric field and the (outgoing) spin current density at the interface [7, 6, 5, 30] and can be interpreted as an interfacial SHE. Alternatively, it can be interpreted as if the electric field induces an homogeneous spin ECP via an interfacial EE, which in turn diffuses into N. Both interpretations are fully compatible within the present formalism. The second type of processes taking place at the interface are spin-losses (first two terms in the r.h.s. of Eq. (2.24)), quantified by the spin-loss conductances per area $G_{\perp/\parallel}$ for spins perpendicular/parallel ($\hat{\mu}_\perp/\hat{\mu}_\parallel$) to the interface.

The charge is obviously conserved and, therefore, the r.h.s. of Eq. (2.25) only contains the spin-to-charge conversion term. The latter is the reciprocal of the last term in Eq. (2.24) [2] so it can be interpreted as an interfacial inverse SHE. But again, an alternative interpretation is possible: from the conservation of the charge current at the interface, we can relate the bulk charge current to the divergence of an interfacial current as $\sigma_D(\nabla\cdot\mathbf{n})\mu\big|_0 = -e\nabla\cdot\mathbf{j}_I$. Comparing the latter with Eq. (2.25), we define $\mathbf{j}_I$ as: [3]

$$e\mathbf{j}_I = -\sigma_{sc}\left(\mathbf{n}\times\hat{\mu}\right)\big|_0 . \tag{2.26}$$

Written this way, BC (2.25) describes the conversion of a non-equilibrium spin into an interfacial charge current, which corresponds to an interfacial IEE, see Fig. 2.4b.

On the one hand, the charge-to-spin conversion is experimentally detected via ferromagnetic layers, at which a spin-dependent voltage drop appears when a spin current arrives from a conductive layer [153]. On the other, the spin-to-charge conversion is directly measured from the generated voltage drop from the induced charge current being confined in a finite system. In general, the voltage drop between two points located at $k = \pm L_k/2$, with $k = x, y, z$, is related to the spatial distribution of charge ECP in the k direction after averaging over the cross-sectional area of the device A_N:

$$V = -\frac{\iiint_{-\frac{L_k}{2}}^{\frac{L_k}{2}} \nabla\mu\cdot\mathbf{e}_k\, dk\, dS}{e\, A_N} . \tag{2.27}$$

Therefore, integrating the charge diffusion equation (2.22), applying BC (2.25), and assuming open circuit configuration in k direction, $j_k\big|_{\pm L_k/2} = 0$, it can be shown that the gradient of the charge ECP is directly proportional to the spin ECP. Finally, the averaged voltage drop in the k direction can be calculated as follows:

$$V_{sc} = \frac{\sigma_{sc}\iint_{-\frac{L_k}{2}}^{\frac{L_k}{2}} \left(\mathbf{n}\times\hat{\mu}\big|_0\right)\cdot\mathbf{e}_k\, dx\, dy}{e\sigma_N A_N} \tag{2.28}$$

where we denote V_{sc} as the ISOC-related voltage drop.

[2] Symmetry arguments alone cannot fix the relation between σ_{sc} and σ_{cs} [30]. However, we will see by contrasting theory with experiment, that reciprocity requires $\sigma_{sc} = \sigma_{cs}$.

[3] Notice that, in principle, an additional divergenceless term may appear in the r.h.s. of Eq. (2.26). Indeed, as demonstrated in Ref. [30], symmetry allows for a term proportional to the out-of-plane component of the spin ECP. In the present work, we only consider spin polarization parallel to the I/N interface and, hence, we neglect that term.

2.2 Spintronics: summary of the results

2.2.1 Non-local magnetoelectric effects in diffusive conductors with spatially inhomogeneous spin-orbit coupling

We summarize here the main results obtained in the published work compiled as Chapter 4. In this work, we study the charge and spin spatial distribution in hybrid devices with different strength or type of linear-in-momentum SOC. Importantly, we assume that the possible SOC arising right at the interface is negligible.

Specifically, we apply the general drift-diffusion model within the SU(2) formalism presented above, Eqs. (2.15) and (2.16), together with the derived BC shown in Sec. 2.1.1, to a system combining a region with Rashba SOC and another one without SOC. We describe non-local measurements of both the SGE and its inverse. The main phenomena can be explained from the SU(2)-covariant conservation of the spin. Interestingly, this conservation prevents the appearance of spin Hall currents in addition to the SGE or ISGE in homogeneous systems (see 2.1.1). As shown in Eq. (2.12), the introduction of an external spin relaxation mechanism, such as magnetic impurities and/or a random SOC at non-magnetic impurities, leads to a breaking in the spin covariant conservation, and hence to finite spin Hall currents.

We first explore the ISGE, i.e., applying an electric field to the system, spin polarization is induced in the Rashba region, which may diffuse into the normal conductor. Our results demonstrate that this diffusion depends on both the electric field's direction and the strength of the ESR rate. The dependence in the direction of the electric field is directly shown in Eq. (2.21), which is the BC that we derive in Chapter 4 for the spin density. We also study the spin-to-charge conversion and compute the charge current and the distribution of electrochemical potential in the whole system when a spin current is injected into the normal region.

In addition, we present a general derivation of the reciprocity between the non-local SGE and ISGE results obtained. This relation explains the reciprocity found between the spin density injected (measured) at a given point in the normal region and the spatially integrated charge current measured (applied) in the adjacent Rashba region.

Finally, we compute the local currents and redistribution of the electrochemical potential induced by the SGE in a system of finite lateral dimensions without ESR.

2.2.2 Quantification of interfacial spin-charge conversion in hybrid devices with a metal/insulator interface

Here, we sum up the main results of the published work compiled as Chapter 5. In this work, we consider a hybrid system combining non-magnetic metal/insulator bulk structures without SOC, at which interface ISOC is induced. Applying the drift-diffusion equations (2.22) and (2.23) at the conductive layer and the effective BC (2.24) and (2.25) at the interface with the insulator, we compute the spin and charge spatial distribution at the system.

Indeed, based on symmetry arguments, we provide a universal theoretical description of spin-charge interconversion in I/N heterostructures with ISOC. Within this model, the interface is described by two type of processes: spin-losses, parameterized by the interfacial conductances $G_{\parallel/\perp}$, and spin-charge interconversion, quantified by σ_{sc} and σ_{cs}. These parameters are material specific. We furthermore demonstrate that the conversion efficiency depends solely on these interfacial parameters.

We apply this formalism to two typical spintronic devices that exploit ISOC: a lateral spin valve and a multilayer Hall bar, for which we calculate the non-local resistance and the spin

Hall magnetoresistance, respectively. The SOC is assumed to be present only at the interface between a copper and a bismuth oxide layers in both devices. In particular, we are able to explain the experimental non-local measurements in a Py/Cu lateral spin valve with a middle BiO_x/Cu wire and the spin magnetoresistance measurements in a multilayered BiO_x/Cu/YIG device (see Chapter 5 for further details), carried out by the group of Dr. Fèlix Casanova at CIC nanoGUNE (Donostia-San Sebastián, Gipuzkoa, Spain). It follows from the application of the theory to the experimental results that the Onsager reciprocity between the spin-charge interconversions is directly captured by $\sigma_{sc} = \sigma_{cs}$. Furthermore, we verify that the same set of interfacial parameters quantifies transport properties related to the ISOC even in different devices if the interface is made of the same materials.

2.3 Nanophotonics: models and methods

We shall now move to the review of the model and methods applied in the other two published works of this Thesis, compiled as Chapters 6 and 7. We focus on studying the spin-orbit interactions arising in light scattering problems, which can be approached from different perspectives. This section reviews two of the most studied models in nanophotonics, namely, the multipole expansion and the Mie theory.

When an electromagnetic wave impinges on a particle, it induces a local electronic disruption, i.e., a certain current density $\mathbf{J}(\mathbf{r})$. The later is the source of scattered electromagnetic radiation via Maxwell's equations (1.7) and (1.10) or, equivalently, via Eq. (2.4). Therefore, we can compute the scattered fields from the internal electric currents. For this, it is useful to expand the Green's function in Eq. (2.4), in *multipoles* [81, 114]. Every multipole moment is related to a charge current distribution or, equivalently, to a certain charge density distribution inside the particle. The exact multipole expansion in spherical waves for, e.g. the vector potential [4] in Eq. (2.4) is given by [81]:

$$\mathbf{A} = ik\mu_0 \sum_{l=0}^{\infty} \sum_{m=-l}^{l} h_l^{(1)}(kr) Y_l^m(\theta,\phi) \int_{V'} \mathbf{J}(\mathbf{r}') j_l(kr') Y_l^{*m}(\theta',\phi')\, dV' \,, \tag{2.29}$$

where μ_0 is the vacuum permeability, $h_l^{(1)}(kr)$ is the spherical Hankel function of the first kind, $j_l(kr)$ is the spherical Bessel function, and $Y_l^m(\theta,\phi)$ are the scalar spherical harmonics. The internal spherical coordinates are denoted by (r',θ',ϕ') and the scattered ones as (r,θ,ϕ). As an illustrative example, we show in Fig. 2.5 the dipolar moments of the expansion, addressed in Chapters 6 and 7. Namely, we consider a sufficiently small spherical scatterer compared with the incident wavelength that can be described only with the first multipolar order ($l = 0$), i.e., with the electric $\mathbf{p}$ and magnetic $\mathbf{m}$ dipole moments. The different distributions of the internal currents (a) and (b) traduce in electric (c) and magnetic (d) dipole moments. For this case, it can be demonstrated [117, 81, 114, 2, 173] that the magnitude of the dipolar moments for materials with linear response (see Eq. (1.12)) can be written as:

$$\mathbf{p} \approx \frac{i}{\omega} \int_{V'} \mathbf{J}(\mathbf{r}')\, dV' = \varepsilon_0 \alpha_E \mathbf{E}^{(0)}|_0 \,, \quad \mathbf{m} \approx \frac{1}{2} \int_{V'} (\mathbf{J}(\mathbf{r}') \times \mathbf{r}')\, dV' = \alpha_M \mathbf{H}^{(0)}|_0 \,, \tag{2.30}$$

[4] This expansion can also be done for the scalar potential, obtaining the multipole moments of the charge density ρ. Through the charge continuity equation (2.1), the multipole moments obtained from the expansion of the vector and scalar potentials are equivalent [81].

where $\mathbf{E}^{(0)}|_0, \mathbf{H}^{(0)}|_0$ are the incident fields evaluated at the particle's center, and $\alpha_{\mathrm{E}}, \alpha_{\mathrm{M}}$ denote, respectively, the electric and magnetic characteristic polarizabilities of the particle. The value of the polarizabilities depends on the scattering fundamental parameters: incident wavelength, particle's shape and dimensions, and refractive indices of host medium and particle. In other words, we need to calculate the internal electric currents to determine the value of the polarizabilities. This implies solving the complete scattering problem.

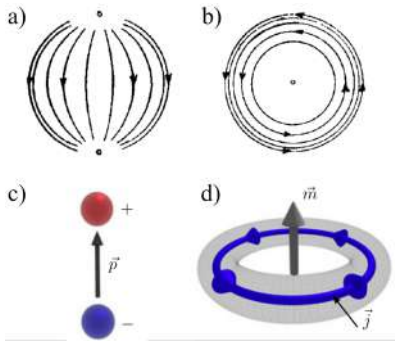

Fig. 2.5 (a, b) Distribution of the internal electric currents for the two first multipolar moments, from Ref. [28], which traduce in the electric (c) and magnetic (d) dipole moments, from Ref. [114].

This is where the second model, the Lorenz-Mie-Debye theory, commonly referred to as Mie theory in the literature, comes into play [152, 76, 28]. In a nutshell, Mie theory is the exact analytical solution of Maxwell's equations for the plane wave scattering problem of an isotropic, homogeneous sphere embedded in an isotropic, homogeneous non-absorbing host medium, using spherical expansions of the incident, $\mathbf{E}^{(0)}$, internal, $\mathbf{E}^{\mathrm{int}}$, and scattering, $\mathbf{E}^{\mathrm{scat}}$, electromagnetic fields [5]. In this three-dimensional problem, the vector spherical harmonics constitute a highly convenient basis for the expansions, though different spherical basis can be used [81, 57, 110]. Mie theory has been revised in several works (see, e.g. [152, 76]). Here, I follow the textbook written by Bohren and Huffman (2008) [28]. In the latter, the scattering problem solved is related to an incident *linearly* polarized plane wave, whose results for the expansion of the fields are here presented as an illustrative example of how Mie theory can be used. The incident wave can be decomposed as:

$$\mathbf{E}^{(0)} = \sum_{l}^{\infty} E_l \left(\mathbf{M}_{o1l}^{(1)} - i\mathbf{N}_{e1l}^{(1)} \right) , \tag{2.31}$$

where $E_l = E_0 \mathrm{i}^l (2l+1)/(l(l+1))$, $\mathbf{M}_{o1l} = \mathbf{M}_{o1l}(r,\theta,\phi)$ and $\mathbf{N}_{e1l} = \mathbf{N}_{e1l}(r,\theta,\phi)$ are the "electric" and "magnetic" vector spherical harmonics, respectively, and the superscript (1) denote vector spherical harmonics for which the radial dependence of the generating functions is specified by $j_l(kr)$ [28]. If the internal and scattered fields are also expanded, different coefficients arise. In Ref. [28] notation, a_l and b_l are the electric and magnetic scattering Mie coefficients, and c_l and d_l the internal Mie coefficients. The expansion of the fields can thus be written as:

$$\mathbf{E}^{\mathrm{scat}} = \sum_{l}^{\infty} E_l \left(\mathrm{i}a_l \mathbf{N}_{o1l}^{(3)} - b_l \mathbf{M}_{e1l}^{(3)} \right) , \tag{2.32}$$

[5] Further development and applications of the Mie theory to absorbing host media [59], [FALTAN]. Here, we focus on the original problem of Mie scattering.

$$\mathbf{E}^{\text{int}} = \sum_{l}^{\infty} E_l \left(c_l \mathbf{M}_{o1l}^{(1)} - \mathrm{i} d_l \mathbf{N}_{e1l}^{(1)} \right) , \tag{2.33}$$

where the superscript (3) in the vector spherical harmonics is now related to $h_l^{(1)}(kr)$ [28]. By imposing BC for the fields transverse components at the surface of the particle,

$$\hat{\mathbf{e}}_r \times \left(\mathbf{E}^{(0)} + \mathbf{E}^{\text{sca}} - \mathbf{E}^{\text{int}} \right) = 0, \tag{2.34}$$

$$\hat{\mathbf{e}}_r \times \left(\mathbf{H}^{(0)} + \mathbf{H}^{\text{sca}} - \mathbf{H}^{\text{int}} \right) = 0. \tag{2.35}$$

these coefficients can be calculated:

$$a_l = \frac{m S_l(y) S_l'(x) - S_l(x) S_l'(y)}{m S_l(y) C_l'(x) - C_l(x) S_l'(y)} , \tag{2.36}$$

$$b_l = \frac{S_l(y) S_l'(x) - m S_l(x) S_l'(y)}{S_l(y) C_l'(x) - m C_l(x) S_l'(y)} , \tag{2.37}$$

$$c_l = \frac{S_l(x) C_l'(x) - S_l'(x) C_l(x)}{m S_l(y) C_l'(x) - C_l(x) S_l'(y)} , \tag{2.38}$$

$$d_l = \frac{S_l(x) C_l'(x) - S_l'(x) C_l(x)}{S_l(y) C_l'(x) - m C_l(x) S_l'(y)} . \tag{2.39}$$

Here, the scatterer (and the host medium) is assumed to be non-magnetic, so the permeability contrast is $\mu = \mu_{\text{p}}/\mu_{\text{h}} = \mu_0/\mu_0 = 1$, where the subindices p and h refer to particle and host medium. The refractive index contrast is denoted by $m = m_{\text{p}}/m_{\text{h}}$. $S_l(z) = z j_l(z)$ and $C_l(z) = z h_l^{(1)}(z)$ are the Riccati-Bessel functions, and the arguments $x = ka$ and $y = mx$ are the *size parameters*. Mie coefficients constitute the main result of the Mie theory, which are valid regardless of the spherical basis used for the expansion. Besides, though the scattering problem in Ref. [28] is in particular solved for an incident linearly polarized plane wave, Mie coefficients do not depend on the incoming polarization. As a result, the same results would have been obtained upon circularly or elliptically polarized plane wave illumination. It is also important to mention that in this basis, the lowest order, i.e., the dipolar order, corresponds to $l = 1$, instead of $l = 0$ as in the multipole expansion of Eq. (2.29).

Although Mie theory is the exact, elegant mathematical solution of plane wave scattering from spheres, the inscrutably concise form of the Mie coefficients, Eqs. (2.36)–(2.39), defies physical interpretation [43]. In this regard, it is useful to compare Mie theory with the multipole expansion, specially in the dipolar regime. Namely, we can compare the electric field radiated by the electric and magnetic point dipoles of Eq. (2.30), which can be found in many textbooks, e.g. [81], with Eq. (2.32). If we do the same with the scattered magnetic fields, we obtain the following relations [117, 43, 2]:

$$\alpha_{\text{E}} = \mathrm{i} a_1 \frac{6\pi}{k^3} , \quad \alpha_{\text{M}} = \mathrm{i} b_1 \frac{6\pi}{k^3} . \tag{2.40}$$

From here we can extract the following physical insight: if a sphere under plane wave illumination can be described only by the dipolar Mie coefficients, a_1 and b_1, the sphere scatters exactly the same as the combination of point electric and magnetic dipoles located at the particle's center.

It is important to stress that Mie theory can be formulated in different bases, provided it is a complete, orthonormal spherical basis such as the one used above. In Sec. 2.3.1, we introduce

the so-called helicity basis, which will be used in Chapters 6 and 7. Nevertheless, the change of basis would not imply a change in the Mie coefficients, which depend only on the refractive index contrast m and the size parameter x of the sphere. Then, in Sec. 2.3.2, we review and define within Mie theory different scattering parameters: the extinct, absorbed, and scattered powers, cross sections, and efficiencies. Besides, we introduce the asymmetry parameter. In Sec. 2.3.3, Mie theory is applied within the helicity basis to the scattering problem analyzed in the work of Arnoldus et al. (2008) [10], summarized in Sec. 1.3, restricted to the electric dipolar regime, i.e., only a_1 contributes to the scattering of the sphere. In this scenario, the spin-orbit interaction is described as the possible AM transfer between the OAM and SAM densities during the scattering process. Finally, in Secs. 2.4.1 and 2.4.2 we go beyond the electric dipolar regime, taking into account both a_1 and b_1, studying the effects of the interaction between the dipolar electric *and* magnetic modes. These two last sections correspond to a brief summary of the results of the two published works belonging to the Nanophotonics part of the present Thesis, compiled as Chapters 6 and 7.

2.3.1 Helicity basis and duality symmetry

As mentioned above, the vector spherical harmonics are suitable for the spherical expansion of the fields. Different conventions can be used to define a complete orthonormal basis with the vector spherical harmonics [28, 76, 152] compatible with the application of Mie theory. Namely, the chosen particular combination of vector spherical harmonics in the present Thesis are those that are simultaneous eigenfunctions of the total (in the propagation direction) and the square of the AM, $\hat{\mathrm{J}}_z$ and $\hat{\mathrm{J}}^2$, and the helicity operator $\hat{\Lambda}$. This basis is especially suitable for the scattering problem of a circularly polarized plane wave, addressed in Chapters 6 and 7. It is also important to mention that Ref. [57] shows that this basis can be used as a complete, practical framework for studying light-matter interactions based only on the helicity and total AM. However, we introduce the separation of the total AM into the SAM and OAM components for this Thesis, giving a more customary physical insight.

The helicity operator originates from the projection of the total AM operator onto the normalized linear momentum operator, i.e., $\hat{\Lambda} = \hat{\mathrm{J}} \cdot \hat{\mathrm{P}}/|\hat{\mathrm{P}}| = (\hat{\mathrm{L}} + \hat{\mathrm{S}}^{\mathrm{spin}}_{ij}) \cdot \hat{\mathrm{P}}/|\hat{\mathrm{P}}|$ [57]. Directly from the definition of the OAM, $\hat{\mathrm{L}} = \mathbf{r} \times \hat{\mathrm{P}}$, and SAM, $\hat{\mathrm{S}}^{\mathrm{spin}}_{ij} = -\mathrm{i}\varepsilon_{ijk}$, operators (see Eq. (1.20)), it can be seen that the helicity is actually $\hat{\Lambda} = \hat{\mathrm{S}}^{\mathrm{spin}} \cdot \hat{\mathrm{P}}/|\hat{\mathrm{P}}|$. We focus on monochromatic fields, for which $|\hat{\mathrm{P}}|$ is directly k and, thus, the helicity operator reads as $\hat{\Lambda} = (1/k)\boldsymbol{\nabla}\times$ [58]. Remarkably, the helicity only can take the eigenvalues $\Lambda = \pm 1$.

A simple example illustrating the concept of helicity is a circularly polarized plane wave. We assume a plane wave along the z direction, that can be written as:

$$\mathbf{E}^{(0)}_{\sigma} = E_0 \, \frac{\hat{\mathbf{e}}_x + \mathrm{i}\sigma\hat{\mathbf{e}}_y}{\sqrt{2}} e^{\mathrm{i}kz} \, , \tag{2.41}$$

where $\sigma = \pm 1$ determines the handedness of the wave (here, $\sigma = +1$ is associated with a left polarized wave) and the corresponding magnetic field is $kZ\mathbf{H}^{(0)}_{\sigma} = -\mathrm{i}\boldsymbol{\nabla} \times \mathbf{E}^{(0)}_{\sigma}$, with $Z = \sqrt{\mu/\varepsilon}$. Applying the helicity operator, one obtains:

$$\hat{\Lambda}\mathbf{E}^{(0)}_{\sigma} = \frac{\boldsymbol{\nabla} \times \mathbf{E}^{(0)}_{\sigma}}{k} = \sigma \mathbf{E}^{(0)}_{\sigma} \, . \tag{2.42}$$

Therefore, a circularly polarized plane wave is an eigenstate of the helicity operator with eigenvalues $\Lambda = \sigma = \pm 1$.

In this Thesis, the following complete eigenbasis, combination of the vector spherical harmonics $\mathbf{X}_{lm}$, is chosen:

$$\hat{\Lambda}\boldsymbol{\Psi}^{\sigma}_{lm} = \sigma\boldsymbol{\Psi}^{\sigma}_{lm}\,, \tag{2.43}$$

with, following Jackson's notation [81],

$$\boldsymbol{\Psi}^{\sigma}_{lm} = \frac{1}{\sqrt{2}}\left[\frac{\boldsymbol{\nabla}\times g_l(kr)\mathbf{X}_{lm}}{k} + \sigma g_l(kr)\mathbf{X}_{lm}\right]\,, \tag{2.44}$$

and

$$\mathbf{X}_{lm} = \frac{1}{\sqrt{l(l+1)}}\hat{\mathbf{L}}Y^m_l(\theta,\phi)\,. \tag{2.45}$$

Here, the radial functions $g_l(kr)$ are linear combinations of the spherical Hankel functions. For the incident and internal fields, $g_l(kr) = j_l(kr)$ since $j_l(kr)$ are finite at $kr = 0$, whereas for scattered fields, $g_l(kr) = h^{(1)}_l(kr)$ since $h^{(1)}_l(kr)$ describe outgoing spherical waves. Furthermore, it can be demonstrated that $\boldsymbol{\Psi}^{\sigma}_{lm}$ are simultaneous eigenvectors of the square of the total AM, j^2, the component of the total AM parallel to the propagation direction, j_z [54] (the propagation direction is chosen to be the z direction), and the helicity operator for monochromatic waves [58], with eigenvalues $l(l+1)$, m, and σ, respectively.

Within this basis, one can expand any field in a multipolar sum of two different terms with opposite helicity:

$$\mathbf{E} = \mathbf{E}_+ + \mathbf{E}_- = \sum_{l=1}^{\infty}\sum_{m=-l}^{m=+l}\left(A^+_{lm}\boldsymbol{\Psi}^+_{lm} + A^-_{lm}\boldsymbol{\Psi}^-_{lm}\right)\,, \tag{2.46}$$

where $A^{+/-}_{lm}$ are expansion coefficients. This helicity decomposition is therefore suitable for the description of the scattering problems addressed here in which the incident field is an eigenstate of the helicity operator, namely, a circularly polarized plane wave. It is important to notice that only if either $A^+_{lm} = 0$ or $A^-_{lm} = 0$, Eq. (2.46) is an eigenvector of the helicity operator with eigenvalue -1 or $+1$, respectively. This can easily be understood in the schematic illustration shown in Fig. 2.6.

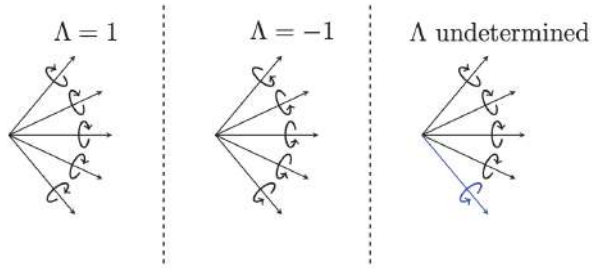

Fig. 2.6 A field composed by the superposition of different eigenfunctions of the helicity operator, e.g. $\boldsymbol{\Psi}^{\sigma}_{lm}$, has definite helicity equal to $+1$ if all the eigenfunctions have left handedness (left panel), -1 if they all have right handedness (central panel). If the field is composed by eigenfunctions with different handedness, the helicity is undetermined (right panel). This figure is taken from Ref. [57].

For fields that are not eigenvectors of the helicity operator, we can calculate the state or degree of circular polarization (DoCP). The DoCP is directly defined as the helicity density, that can be calculated as follows [38]:

$$\text{DoCP} = \Lambda_\theta = \frac{\mathbf{E}^* \cdot (\hat{\Lambda}\mathbf{E})}{\mathbf{E}^* \cdot \mathbf{E}} = \frac{|\mathbf{E}_+|^2 - |\mathbf{E}_-|^2}{|\mathbf{E}_+|^2 + |\mathbf{E}_-|^2} \,. \tag{2.47}$$

In general, the polarization state of electromagnetic radiation is described by the Stokes parameters (I,Q,U,V) [150, 28, 76], corresponding to the intensity, I, and the polarization ellipse parameters whose parametrization corresponds to the Poincaré sphere, Q,U,V. The usefulness of these four parameters is that they are easily measurable. Interestingly, following Ref. [38], it can be shown that the DoCP is also a measurable quantity, since it is related to two of the Stokes parameters as follows (see Chapter 7):

$$\text{DoCP} = \frac{V}{I} \,. \tag{2.48}$$

The introduction of the helicity basis has another advantage, related to the conservation of the helicity under a certain symmetry, the duality symmetry. In 1965, Calkin [36] demonstrated that in the absence of charges and currents, Maxwell's equations (1.7)–(1.10), are invariant under electromagnetic duality transformations, namely, $\mathbf{E} \to \mathbf{E}\cos\theta - \mathbf{H}\sin\theta$ and $\mathbf{H} \to \mathbf{E}\sin\theta + \mathbf{H}\cos\theta$, with θ an arbitrary constant. Using Noether's theorem, he linked this symmetry of the Maxwell's equations to the conservation in time of the degree of circular polarization of the field. Recently, Ref. [58] applied this concept to light-matter interactions in which the duality symmetry is in general broken due to the scattering. Namely, they demonstrated that the restoration of the duality symmetry is possible for materials without free sources, characterized by scalar permittivity and permeability. Furthermore, as shown in Sec. 2.4.1, the restoration of the duality symmetry is intimately related to the enhancement of the optical mirage (see Sec. 1.3) in the backscattering direction.

2.3.2 Mie theory: scattering parameters

When light propagates through a medium and a particle is present, the electromagnetic waves can be either absorbed or scattered. This traduces in an attenuation of the incident illumination, which is called *extinction* [76]. More specifically, to calculate the absorbed, scattered, and extinct energy, it is convenient to separate the electric and magnetic fields outside of the particle in two terms, the incident and scattered fields: $\mathbf{E}^{\text{out}} = \mathbf{E}^{(0)} + \mathbf{E}^{\text{scat}}$ and $\mathbf{H}^{\text{out}} = \mathbf{H}^{(0)} + \mathbf{H}^{\text{scat}}$. From this, the Poynting vector (energy per unit time and unit surface) of Eq. (1.18) can be calculated as:

$$\begin{aligned} \mathbf{S} &= \frac{1}{2}\Re\left\{\mathbf{E}^{(0)} \times \mathbf{H}^{(0)*} + \mathbf{E}^{\text{scat}} \times \mathbf{H}^{\text{scat}*} + \left(\mathbf{E}^{(0)} \times \mathbf{H}^{\text{scat}*} + \mathbf{E}^{\text{scat}} \times \mathbf{H}^{(0)*}\right)\right\} \\ &= \mathbf{S}^{(0)} + \mathbf{S}^{\text{scat}} + \mathbf{S}^{\text{ext}} \,, \end{aligned} \tag{2.49}$$

where it can be seen that the extinction Poynting vector arises from the interference between the incident and scattered fields. Then, the total power crossing an arbitrarily large spherical surface centered on the scatterer, A, i.e., the total energy that the particle absorbs (or possibly creates) is:

$$W_{\text{abs}} = -\int_A \hat{\mathbf{e}}_r \cdot \mathbf{S}\, dA \,. \tag{2.50}$$

which can be analogously separated as:

$$W_{\text{abs}} = W_{(0)} - W_{\text{scat}} + W_{\text{ext}} = -\int_A \hat{\mathbf{e}}_r \cdot \mathbf{S}^{(0)} dA - \int_A \hat{\mathbf{e}}_r \cdot \mathbf{S}^{\text{scat}} dA - \int_A \hat{\mathbf{e}}_r \cdot \mathbf{S}^{\text{ext}} dA \,. \tag{2.51}$$

Since all the incident power is both incoming and outgoing from the surface for a non-absorbing host medium, $W_{(0)} = 0$. Hence, the energy conservation in scattering problems, known as optical theorem [28, 81, 117], can be formulated as:

$$W_{\text{ext}} = W_{\text{abs}} + W_{\text{scat}} \,. \tag{2.52}$$

Usually, the extincted, absorbed, and scattered powers are normalized by the incident irradiance, which is the energy flow per unit time and unit area, i.e., Poynting vector, incident to the particle, $|\mathbf{S}^{(0)}|$. These normalized powers have units of area and are calculated as follows:

$$\sigma_{\text{ext}} = \frac{W_{\text{ext}}}{|\mathbf{S}^{(0)}|} \,, \quad \sigma_{\text{abs}} = \frac{W_{\text{abs}}}{|\mathbf{S}^{(0)}|} \,, \quad \sigma_{\text{scat}} = \frac{W_{\text{scat}}}{|\mathbf{S}^{(0)}|} \,, \tag{2.53}$$

corresponding, respectively to the extinction, absorption, and scattering cross sections.

Using the expanded incident and scattered fields within Mie theory, the Poynting vector and, thus, the cross sections can be calculated as a function of the Mie coefficients. Namely, they take the following form for spheres under plane wave illumination, regardless of the incident polarization [28, 76, 152]:

$$\sigma_{\text{ext}} = \frac{2\pi}{k^2} \sum_{l=1}^{\infty} (2l+1) \Re\{a_l + b_l\} \,, \tag{2.54}$$

$$\sigma_{\text{scat}} = \frac{2\pi}{k^2} \sum_{l=1}^{\infty} (2l+1) (|a_l|^2 + |b_l|^2) \,, \tag{2.55}$$

$$\sigma_{\text{abs}} = \sigma_{\text{ext}} - \sigma_{\text{scat}} \,, \tag{2.56}$$

where total energy conservation is used for the last expression.

Another cross section can be defined, which corresponds with the particle's actual geometrical area. Since here we consider spherical scatterers, the geometrical cross section is $\sigma_{\text{geom}} = \pi a^2$, with a the radius of the particle. As a consequence, extinction, Q_{ext}, absorption, Q_{abs}, and scattering, Q_{scat}, efficiencies for spheres under plane wave illumination can be calculated as the ratio between each of the cross sections and the geometrical area as follows:

$$Q_{\text{ext}} = \frac{\sigma_{\text{ext}}}{\pi a^2}, \quad Q_{\text{abs}} = \frac{\sigma_{\text{abs}}}{\pi a^2}, \quad Q_{\text{scat}} = \frac{\sigma_{\text{scat}}}{\pi a^2} \,. \tag{2.57}$$

In addition to the cross sections and the efficiencies, there is another scattering parameter that can be useful to analyze scattering problems: the widely used asymmetry parameter [28]. Asymmetry parameter, or g-parameter, is defined as the mean cosine of scattering angle, $\langle \cos\theta \rangle$, and characterizes the degree of anisotropy of a scattering process:

$$g = \langle \cos\theta \rangle = \frac{\int_\Omega (\mathbf{S}_{\text{scat}} \cdot \hat{\mathbf{e}}_r) \cos\theta \, d\Omega}{\int_\Omega (\mathbf{S}_{\text{scat}} \cdot \hat{\mathbf{e}}_r) \, d\Omega}, \tag{2.58}$$

If the particle scatters light isotropically, the g-parameter is equal to zero; if the particle scatters more light in the forward direction, $g > 0$; and if light is more scattered in the backward direction,

$g < 0$. Using Mie notation, the g-parameter can be calculated as follows [28]:

$$g = \frac{4}{x^2 Q_{\text{scat}}} \left[\sum_{l=1}^{\infty} \frac{l(l+2)}{l+1} \Re\{a_l a_{l+1}^* + b_l b_{l+1}^*\} + \sum_l \frac{2l+1}{l(l+1)} \Re\{a_l b_l^*\} \right] . \tag{2.59}$$

In particular, the two works compiled in this Thesis, Chapters 6 and 7, are restricted to the dipolar regime. The g-parameter in this regime can be calculated by setting $l = 1$ in the previous equation, yielding:

$$g = \frac{\Re\{a_1 b_1^*\}}{|a_1|^2 + |b_1|^2} , \tag{2.60}$$

where a_1 and b_1 are the first, dipolar, scattering Mie coefficients.

2.3.3 Spin-orbit interactions: transfer between SAM and OAM

Hitherto, Mie theory and the helicity basis have been briefly introduced in rather general terms. In this section, Mie theory is applied using the helicity basis to the scattering problem addressed in two of the works compiled in this Thesis (see Chapters 6 and 7): a circularly polarized plane wave incident on a non-absorbing dielectric nanosphere. The nanosphere, with radius a and refractive index m_{p}, is embedded in an otherwise non-absorbing homogeneous medium with refractive index m_{h}. The incident beam is therefore Eq. (2.41), with well-defined helicity, $\Lambda = \sigma$, expanded in the helicity basis:

$$\frac{\mathbf{E}_\sigma^{(0)}}{E_0} = \sum_{l=0}^{\infty} \sum_{m=-l}^{+l} \sum_{\sigma'=-1}^{+1} C_{lm}^{\sigma\sigma'} \mathbf{\Psi}_{lm}^{\sigma'} , \tag{2.61}$$

where $g_l(kr) = j_l(kr)$ in Eq. (2.44), $k = m_{\text{h}} k_0 = m_{\text{h}} 2\pi/\lambda_0$, with λ_0 the wavelength in vacuum, and

$$C_{lm}^{\sigma\sigma'} = \sigma \mathrm{i}^l \sqrt{4\pi(2l+1)} \delta_{m\sigma} \delta_{\sigma\sigma'} . \tag{2.62}$$

The OAM and SAM densities per photon can be calculated using Eq. (1.21) and (1.22). Since the plane wave is parallel to the z direction, the z component of the OAM and SAM densities is the only finite one, with values:

$$l_z = \frac{\mathbf{E}_\sigma^{(0)*} [-\mathrm{i}(x\partial_y - y\partial_x)] \mathbf{E}_\sigma^{(0)}}{\mathbf{E}_\sigma^{(0)*} \cdot \mathbf{E}_\sigma^{(0)}} = 0 , \tag{2.63}$$

$$s_z = \frac{\mathbf{E}_\sigma^{(0)*} \times \mathbf{E}_\sigma^{(0)}}{\mathbf{E}_\sigma^{(0)*} \cdot \mathbf{E}_\sigma^{(0)}} = \sigma , \tag{2.64}$$

and, thus, $j_z = l_z + s_z = m = \sigma = \Lambda$.

On the other hand, the scattered fields can be written as follows applying Mie theory in the same helicity basis:

$$\frac{\mathbf{E}_\sigma^{\text{scat}}}{E_0} = \sum_{l=0}^{\infty} \sum_{m=-l}^{+l} \sum_{\sigma'=-1}^{+1} D_{lm}^{\sigma\sigma'} \mathbf{\Psi}_{lm}^{\sigma'} , \tag{2.65}$$

where $g_l(kr) = h_l^{(1)}(kr)$ in Eq. (2.44), and

$$D_{lm}^{\sigma\sigma'} = -\mathrm{i}^l \sqrt{4\pi(2l+1)} \delta_{m\sigma} \frac{\sigma a_l + \sigma' b_l}{2} , \tag{2.66}$$

with a_l and b_l the Mie coefficients defined in Eqs. (2.36) and (2.37).

As mentioned above, the helicity in general is not a conserved quantity, but only when the duality symmetry is restored in the system. In contrast, since the scatterer is spherical, it presents azimuthal symmetry, and j_z of the incoming wave is preserved. After scattering, this yields to an effective AM transfer from the spin to the orbital components, keeping the value of j_z constant. This transformation between SAM and OAM components is the particular spin-orbit interaction that this Thesis focuses on. Namely, the scattered fields also have constant eigenvalue $j_z = l_z + s_z = m = \sigma$, with

$$l_z = \frac{\mathbf{E}_\sigma^{\text{scat}*}[-\mathrm{i}(\mathbf{r}\times\boldsymbol{\nabla})\cdot\hat{\mathbf{e}}_z]\mathbf{E}_\sigma^{\text{scat}}}{\mathbf{E}_\sigma^{\text{scat}*}\cdot\mathbf{E}_\sigma^{\text{scat}}}\,, \tag{2.67}$$

$$s_z = \frac{(\mathbf{E}_\sigma^{\text{scat}*}\times\mathbf{E}_\sigma^{\text{scat}})\cdot\hat{\mathbf{e}}_z}{\mathbf{E}_\sigma^{\text{scat}*}\cdot\mathbf{E}_\sigma^{\text{scat}}}\,. \tag{2.68}$$

Depending on the scattering point and the size parameters x and y, these densities per photon can take different values. For instance, Ref. [10] assumes that the particle is sufficiently small, $x \ll 1$, that the scattering can be described only with the first electric dipolar term of the expansion. In that case, only a_1 is assumed to be finite and, thus:

$$\frac{\mathbf{E}_\sigma^{\text{scat}}}{E_0} = -\mathrm{i}\sqrt{3\pi}\sigma a_1\left(\boldsymbol{\Psi}_{1\sigma}^{+} + \boldsymbol{\Psi}_{1\sigma}^{-}\right)\,. \tag{2.69}$$

Substituting this equation in Eqs. (2.67), (2.68), and (2.47) yields:

$$l_z = \sigma\frac{\sin^2\theta}{1+\cos^2\theta}\,, \tag{2.70}$$

$$s_z = \sigma\frac{2\cos^2\theta}{1+\cos^2\theta}\,, \tag{2.71}$$

$$\Lambda_\theta = \sigma\frac{2\cos\theta}{1+\cos^2\theta}\,, \tag{2.72}$$

where we notice the relation between SAM and helicity densities, $s_z = \Lambda_\theta\cos\theta$.

As explained in Sec. 1.3, the apparent shift, which we refer to as optical mirage, can be calculated via Eq. (1.24). In the pure electric dipolar regime considered in Ref. [10], Eq. (1.24) shows that the maximum value is of subwaelength order, $\Delta = \lambda/\pi$, at the perpendicular to the incident direction plane, i.e., x–y plane.

2.4 Nanophotonics: summary of the results

2.4.1 Enhanced spin-orbit optical mirages from dual nanospheres

In this section, we outline the main results of Chapter 6. In the latter, we specifically analyze the circularly polarized plane wave scattering problem of a subwavelength silicon particle in the dipolar electric *and* magnetic regime. We thus go beyond the result of Ref. [10]. Using Mie theory within the helicity basis, we compute the scattered Poynting vector and the corresponding optical mirage via Eq. (1.24). In this case, we obtain the following result:

$$\frac{\Delta}{(\lambda/\pi)} = -\frac{l_z(\theta)}{\sin\theta}\hat{\mathbf{e}}_\varphi = \frac{s_z(\theta)-\sigma}{\sin\theta}\hat{\mathbf{e}}_\varphi = -\sigma\,\frac{\sin\theta(1+2g\cos\theta)}{1+\cos^2\theta+4g\cos\theta}\hat{\mathbf{e}}_\varphi\,. \tag{2.73}$$

This equation summarizes all the results obtained in Chapter 6. First of all, we find a relation between the optical mirage and the OAM density, that is useful for the understanding of the optical mirage as a consequence of the conversion between OAM and SAM densities. This conversion follows from the conservation of the total AM density component parallel to the incident radiation, i.e., z direction, as explained in the previous section, with $j_z = \sigma = l_z + s_z$. Finally, when the Si nanosphere is dual, $a_1 = b_1$, leading to $g = 0.5$ in Eq. (2.60), the optical mirage diverges in the backscattering direction, $\theta \to \pi$. We analyze this result for the optical mirage, from two frameworks: spin-orbit interactions of light and helicity conservation.

2.4.2 Asymmetry and spin-orbit coupling of light scattered from subwavelength particles

Here, we summarize the main results presented in Chapter 7. The analytical work developed in Chapter 6 revealed different relations between the optical mirage, the g-parameter, and the duality symmetry. In Chapter 6, we further analyze the problem and demonstrate that the remarkable angular dependence of these optical mirages and those of the intensity, DoCP or helicity, and SAM and OAM of scattered photons are all linked and fully determined by the g-parameter. This traduces in results that are independent of the specific optical properties of the scatterer. Furthermore, we show that the g-parameter can be entirely determined by measuring the scattered helicity at the perpendicular direction to the incoming plane wave. This simple relation between the helicity and the asymmetry parameter opens the possibility to infer the scattered fields' whole angular properties by a single far-field polarization measurement.

Moreover, each of the values of the g-parameter, describe different scattering responses in the electric and magnetic dipolar regime. For instance, at $g = 0$, we recover the results of Ref. [10]. Accordingly, particles with different optical properties, but which share an identical g-parameter value, lead to the same angular dependence of intensity, DoCP, SAM to OAM exchanges and optical mirage.

Finally, we demonstrate that the maximum optical mirage does not correspond to the zeros of the SAM, in contrast to what occurs when only considering a pure electric dipole.

Chapter 3

Conclusions

This Thesis has been motivated by the ambitious goal of unifying the theory of spin-orbit interactions in two research fields: spintronics and nanophotonics. The work was triggered by our original approach to the single impurity scattering problem for both electron and electromagnetic radiation, presented in Sec. 1.3. In Refs. [19, 10], respectively, it was predicted that an apparent shift appeared in both scenarios after scattering. Based on the model applied in Ref. [10], our first analysis yields a common fundamental understanding of these apparent shifts. Namely, the spiraling structure of the energy transfer rate vector in the near-field leads to an apparent displacement of the sphere's actual position when viewed far from it. After this work, we realized that several properties related to the spin-orbit in electronic and light systems were unexplored. These findings are the basis of the various papers presented in this Thesis with an in-depth study of spin-orbit interactions in both fields.

Chapters 4 and 5, correspond to my works on spintronics, i.e. electronic systems. In such structures, SOC offers the possibility of controlling spin densities and currents by electric means, relating charge and spin currents, via direct and inverse SHE, or charge current and spin density, via direct and inverse SGE. Since strong SOC is related to strong spin relaxation, most of the spintronics devices combine regions with strong SOC to generate and manipulate spins and another one with negligible SOC to transport the spins. From a general perspective, we address the problem of describing these magnetoelectric effects in hybrid diffusive devices through well-known spin and charge drift-diffusion equations combined with effective boundary conditions (BC). Our descriptions are based on charge conservation, the consequences of the spin relaxation, and symmetry considerations, key to understanding the appearance of SHE and/or SGE. We focus on hybrid devices with both intrinsic and extrinsic sources of SOC, where the latter is either a bulk or interface property.

Specifically, in Chapter 4, we describe hybrid systems combining regions with different kind or strength of intrinsic linear-in-momentum SOC, including possible extrinsic impurities. Importantly, we assume that *no* SOC is induced at the interface between different regions. In this case, both intrinsic and extrinsic SOC can be included in the drift-diffusion equations within the SU(2) formalism (see, e.g., Refs. [132, 131, 67]). Our main contribution is to obtain the needed BC for the spin density integrating these equations right at the interface, generalized for any linear-in-momentum SOC and direction of the external applied electric field. We apply our model to adjacent Rashba and normal (without SOC) regions, analyzing the non-local spin galvanic effect (SGE)

and inverse SGE (ISGE) and the reciprocity between them, which could be measured in a lateral spin valve device. Non-local ISGE describes the possible diffusion of the spin density induced at the SOC region when applying an external electric field. In contrast, non-local SGE describes the possible generation of charge currents at the SOC region due to spin injection at the normal region. The main conclusion is that these magnetoelectric effects depend entirely on the electric field's direction or the injected spin density and the possible breaking of the SU(2)-covariant conservation of the spin.

Chapter 5 addresses hybrid devices combining two diffusive regions *without* SOC at whose interface SOC is induced, i.e., at microscopic scales much smaller than the mean free path of the electrons. Consequently, we can describe both regions within the drift-diffusion model, but the interfacial SOC (ISOC) cannot be included. Our solution consists of using the method of Refs. [30, 5–7], effectively including all the possible ISOC magnetoelectric effects as different phenomenological terms for the spin and charge BC, describing spin Hall effects (SHE), SGE, and spin relaxation at the interface. This method is based only on symmetry considerations, following the general principle also applied in the well-known textbook "*Spin Physics in Semiconductors*" [50]: *everything, that is not forbidden by symmetry or conservation laws, will happen*. This way, we offer a complete, universal description of metal/insulator hybrid systems with ISOC with interfacial parameters within the BC. As a demonstration of our model's usefulness, we apply the drift-diffusion model and the symmetry-based BC to two different devices, both with the same interface with ISOC, namely, a BiO_x/Cu interface. In particular, we quantify the interfacial parameters of our effective model by experimental reciprocal measurements in a lateral spin valve and a multilayered device with the same ISOC, carried out by the group of Dr. Fèlix Casanova at CIC nanoGUNE (Donostia-San Sebastián, Gipuzkoa, Spain). Since the same value of the interfacial parameters describe both experiments, our findings confirm that the effect of spin-charge interconversion is an inherent property of the interface.

It is worth mentioning another work related to SOC that we published in collaboration with the group of Dr. Francesco Giazotto from NEST Laboratory (Escuola Normale Superiore, Pisa, Italy): the realization of a Josephson phase battery [151]. The Josephson effect arises in superconducting junctions, i.e., junctions between two superconductors separated by a non-superconducting link. It consists of a dissipation-less current that can be controlled by the phase difference between the superconducting electrodes [84, 14]. In conventional Josephson junctions, such supercurrent can flow when the phase difference is finite. However, if the junction is made of a material with sizable SOC, Ref. [21] shows from symmetry arguments the possibility of inducing a controllable, non-vanishing phase difference if an external magnetic or intrinsic exchange field is present. In such a case, a spontaneous current may flow even in the absence of a phase difference. Such a device has been fabricated by the Pisa group using a nanowire with strong SOC and a superconducting loop. This device can be seen as a phase-battery generating a superconducting phase difference, similar to a battery generating a voltage difference. Our contribution was to interpret the experimental results in terms of the spin-galvanic effect in the superconducting state. The agreement between theory and experiment is excellent. For details, the reader is referred to our publication, Ref. [151].

As a consequence of the previous work, we also had the opportunity to collaborate with Dr. Claudio Guarcello to study in detail the hysteretical behavior observed in a superconducting quantum interference device (SQUID) with an anomalous junction. Our work in Ref. [69] provides a full theoretical description of the influence of a varying external magnetic field on the transport properties of superconducting loops.

In the other part of this Thesis, we focus on nanophotonics. The main works in this topic are presented in Chapters 6 and 7. Both works consider the scattering problem of a dipolar dielectric sphere under the illumination of a circularly polarized plane wave. The main point of these two works is to consider that the sphere sustains both an electric and a magnetic dipolar response and, thus, the interplay between these two may lead to intriguing effects. In this regard, depending on the strength of the two optical responses, described by the electric, α_{E}, and magnetic, α_{M}, polarizabilities, strong directionality can be obtained at the Kerker conditions. Combining the first Kerker condition, $a_1 = b_1$, when the sphere is dual, with the scattered Poynting vector's spiraling structure after scattering, we demonstrate that the resulting optical mirage diverges at the backscattering direction. Strikingly, the optical mirage's enhancement can be understood as well from a spin-orbit picture: since the scatterer is azimuthally symmetric, the total incident AM parallel to the propagation direction, which can be split into orbital and spin components, $j_z = l_z + s_z$, is preserved after scattering. In our case, the incident plane wave has $j_z = s_z = \sigma = \pm 1$. Consequently, the orbital, spiraling trajectory of the Poynting vector arises as a transfer between SAM and OAM, which varies at each scattering angle and the specific optical response. Within this perspective, the backscattering divergence of the optical mirage when the system is dual is explained due to an optical vortex's emergence with charge $l_z = 2$ (see Fig. 1.2).

Furthermore, we realized that the asymmetry of the scattering pattern could be used to describe the spin-orbit interactions, as we specifically analyze in Chapter 7. The asymmetry in the scattering is generally described by the asymmetry parameter which, in the dipolar regime, reads as $g = \Re\{a_1 b_1^*\}/(|a_1|^2 + |b_1|^2)$. From this expression, it is noticeable that spheres with different optical properties, i.e., different values of a_1 and b_1, but sharing an identical g-parameter value, will lead to the same angular dependencies of intensity, SAM to OAM exchanges, and optical mirages. Moreover, in these works, we take another symmetry into account, the duality symmetry, and its associated conserved quantity when the system is dual, the helicity density. In this sense, a full link between the optical vortex appearance, the asymmetry parameter, and the conservation of the helicity density or degree of circular polarization arises in the far-field. Finally, we also find a direct relation between the helicity density, measured at the perpendicular to the incident radiation direction, and the asymmetry parameter value. Therefore, this relation can be used to infer all the angular dependencies from a single far-field polarization measurement.

As a consequence of these investigations in light scattering, other research works were developed, which are briefly commented here. Reference [121] includes the role of absorption in dielectric spheres, which translates into enduring spin-orbit interactions but suppresses the divergent optical mirage. The latter is fundamentally explained in Ref. [120] based on our in-depth study of the mathematical description of scattering of dielectric spheres under plane wave illumination, i.e., Mie theory. Namely, we study Kerker conditions upon lossless, absorption, and optical gain regimes, i.e., adding external energy to the system. In the same vein, we mathematically demonstrate in Ref. [119] that going beyond the dipolar regime and, more specifically, the presence of multiple multipolar orders such as the quadrupole or octopole in the scattering response of an object, inhibits any possible dual behavior and, hence, helicity conservation. As a direct consequence, we demonstrate that the helicity conservation can be used as a signature of dipolar regimes in the whole optical spectrum under plane wave illumination. Finally, focusing on the so-called second Kerker condition, we find the specific conditions needed for an optimal backward light scattering in the dipolar regime. Importantly, we clarify the frequent misunderstanding that links the optimal backscattering light with a nearly zero forward scattering. The latter appears if and only if the scattering cross section is smaller than a pure electric (or magnetic) resonant sphere.

In conclusion, for further analogies and a common model to be completed, we needed an in-depth study of the SOI in both spintronics and nanophotonics, presented throughout this Thesis separately. As a consequence of that study, we had the opportunity to contribute to different publications, not only to those compiled here as chapters 4–7, but also those corresponding to Refs. [121, 120, 118, 119, 151, 69]. We firmly believe that this Thesis opens the door to achieve our original objective of a global view of the SOI problems in two of the most promising branches of Physics nowadays, spintronics and nanophotonics.

As Rutherford said: "*All of Physics is either impossible or trivial. It is impossible until you understand it, and then it becomes trivial*". This Thesis hopefully is somewhere between impossible and trivial.

Chapter 4

Nonlocal magnetoelectric effects in diffusive conductors with spatially inhomogeneous spin-orbit coupling

Nonlocal magnetoelectric effects in diffusive conductors with spatially inhomogeneous spin-orbit coupling

Cristina Sanz-Fernández,[1,*] Juan Borge,[2] Ilya V. Tokatly,[2,3,4] and F. Sebastián Bergeret[1,4,†]

[1]*Centro de Física de Materiales (CFM-MPC), Centro Mixto CSIC-UPV/EHU, 20018 Donostia-San Sebastián, Spain*

[2]*Nano-Bio Spectroscopy Group, Departamento de Física de Materiales, Universidad del País Vasco (UPV/EHU), 20018 Donostia-San Sebastián, Spain*

[3]*IKERBASQUE, Basque Foundation for Science, 48011 Bilbao, Spain*

[4]*Donostia International Physics Center (DIPC), 20018 Donostia-San Sebastián, Spain*

(Received 26 July 2019; revised manuscript received 21 October 2019; published 5 November 2019)

We present a theoretical study of nonlocal magnetoelectric effects in diffusive hybrid structures with an intrinsic linear-in-momentum spin-orbit coupling (SOC) which is assumed to be spatially inhomogeneous. Our analysis is based on the SU(2)-covariant drift-diffusion equations from which we derive boundary conditions at hybrid interfaces for SOC of any kind. Within this formulation, the spin current is covariantly conserved when the spin relaxation is only due to the intrinsic SOC. This conservation leads to the absence of spin Hall (SH) currents in homogeneous systems. If, however, extrinsic sources of spin relaxation (ESR), such as magnetic impurities and/or a random SOC at nonmagnetic impurities, are present the spin is no longer covariantly conserved, and SH currents appear. We apply our model to describe nonlocal transport in a two-dimensional system with an interface separating two regions: one normal region without intrinsic SOC and one with a Rashba SOC. We first explore the inverse spin-galvanic effect, i.e., a spin polarization induced by an electric field. We demonstrate how the spatial behavior of such spin density depends on both the direction of the electric field and the strength of the ESR rate. We also study the spin-to-charge conversion, and compute the charge current and the distribution of electrochemical potential in the whole system when a spin current is injected into the normal region. In systems with an inhomogeneous SOC varying in one spatial direction, we find an interesting nonlocal reciprocity between the spin density induced by a charge current at a given point in space, and the spatially integrated current induced by a spin density injected at the same point.

DOI: 10.1103/PhysRevB.100.195406

I. INTRODUCTION

Spin-orbit coupling (SOC) in metals and semiconductors couples the charge and spin degrees of freedom of the electrons and leads to a variety of magnetoelectric effects. For that reason, conductors with sizable SOC are used for the creation and control of spin currents and spin densities by applying electric fields. Reciprocally, magnetoelectric effects allow for detecting spin by measuring electric signals [1,2].

It is customary to distinguish between two kinds of magnetoelectric effects mediated by SOC: those relating spin and charge currents (spin Hall effect and its inverse), and those relating spin polarization and charge current (spin-galvanic effect and its inverse). The spin Hall effect (SHE) is the generation of a spin current, transverse to the applied charge current [2–5]. The inverse effect, commonly known as the inverse SHE [2], corresponds to the spin-to-charge counterpart and consists of a charge current, or a Hall voltage, induced by a given spin current. Both direct and inverse SHE have been measured in several experiments and different materials [6–11].

Here, we focus on the charge-to-spin conversion due to the spin-galvanic effect (SGE), which refers to the generation of a charge current by creating a nonequilibrium spin polarization in the material. It takes place, for example, in materials with a linear-in-momentum intrinsic SOC, such as the Rashba or linear Dresselhaus SOC [12–14]. Conversely, the inverse SGE corresponds to the spin polarization induced by applying an electric field/current [15–22], which in the particular case of Rashba SOC, is also known as the Edelstein effect [23,24]. In contrast to the SHE, the induced spin is homogeneous in space and, in principle, in the stationary case, no spin currents are generated [25–29]. Observation of the SGE and its inverse has been reported in Refs. [7,30–34].

From the experimental point of view, hybrid structures combining different materials play an important role in the detection of magnetoelectric effects. This requires, on the one hand, materials with large SOC for an efficient charge-to-spin conversion and, on the other hand, large enough spin diffusion lengths in order to transport the spin information across the device. At first glance, it seems difficult to find systems satisfying these two conditions because a strong SOC in a diffusive system will inevitably lead to a strong spin relaxation [15]. This problem can be overcome by using hybrid structures combining, for example, two different materials, one with a strong SOC, in which the charge-to-spin conversion occurs,

*cristina_sanz001@ehu.eus

†sebastian_bergeret@ehu.eus

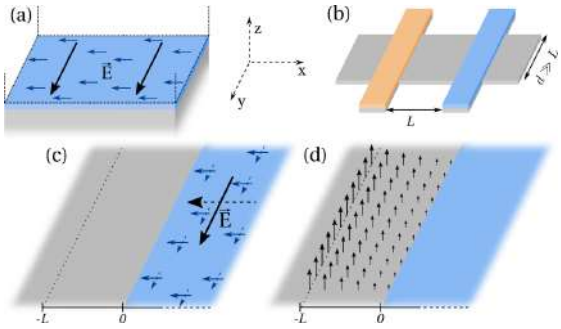

FIG. 1. Schematical view of different setups considered in this work. (a) Heterostructure with a localized SOC at the interface (blue region) between two different materials, in this case a normal conductor (gray bottom region) and an insulator (transparent top region). (b) Hybrid lateral structure for nonlocal transport measurements. The gray region is a normal conductor without SOC connected to two electrodes. At the contact with the blue electrode it is assumed a sizable SOC, whereas the orange electrode is a ferromagnet which may serve as a spin injector or detector. (c) The system under consideration to study the nonlocal inverse SGE. An electric field is applied parallel or perpendicular to the interface, between a normal conductor without SOC (gray region) and a conductor with intrinsic SOC (blue region). A spin density is induced in the latter. We are interested in the spin density at a distance L away from the interface in the normal conductor. (d) Same setup as panel (c) but now a spin is injected into the normal conductor at a distance L from the interface. We are interested in the charge current induced in the blue region as a consequence of the SGE.

adjacent to a second material with a weak SOC where the spin information can be transported over long distances. This conversion can also take place at the interface between a metal and an insulator with a sizable SOC [Fig. 1(a)] [35].

An efficient way of injecting and detecting the spin accumulation is by using nonlocal spin valves, as the one sketched in Fig. 1(b) [34,36–43]. In this setup, the source signal, either a spin or a charge current, is injected from one of the electrodes (orange/blue), whereas the response signal, a charge or spin voltage, is measured nonlocally at the detector electrode (blue/orange). Similar valves combining ferromagnetic electrodes and metallic wires have also been used to measure the SHE [8], as well as to study the reciprocity between the SHE and the inverse SHE [44].

In this work, we present a theoretical study of nonlocal electronic transport in hybrid diffusive systems with linear-in-momentum intrinsic SOC of any type. We focus on the reciprocity between the nonlocal SGE and its inverse. Our analysis is based on the drift-diffusion equations [4] formulated in the language of SU(2) gauge fields, where the intrinsic SOC and the Zeeman field enter as the space and time components of an effective SU(2) 4-potential [45–47]. Within this formalism, the spin obeys a covariant continuity equation which explains the absence of spin Hall (SH) currents in a homogeneous system with intrinsic SOC. This covariant conservation of the spin is broken in the presence of any extrinsic source of spin relaxation (ESR), as for example magnetic impurities or a random SOC originated from scattering of electrons at nonmagnetic impurities. Such symmetry breaking leads to a finite spin current that may flow into a material without SOC.

In order to describe the transport in such hybrid systems, we derive effective boundary conditions (BC) valid for systems of any dimension. These BC describe the transport between diffusive conductors with different (not only in the strength) linear-in-momentum SOC and mean-free path, and they are valid for any direction of the applied field.[1] They generalize the BC obtained in Refs. [28,48–51], for a specific case of two-dimensional (2D) Rashba systems.

We apply the diffusion equation and BC to study nonlocal measurement of the SGE and its inverse in a two-dimensional hybrid system consisting of a diffusive conductor without intrinsic SOC, labeled as normal conductor, adjacent to a Rashba conductor, i.e., a conductor with an intrinsic Rashba SOC [see Figs. 1(c) and 1(d)] [39–43]. First, we address the nonlocal inverse SGE [Fig. 1(c)], and calculate the value of the spin density induced at the normal conductor at a finite distance from the interface with the Rashba region, when an electric field is applied. If the field is parallel to the interface, and due to its covariant conservation, the spin generated at the Rashba conductor cannot diffuse into the normal region, leading to a zero signal [28,48–50]. However, inclusion of ESR breaks the covariant conservation of the spin, and a finite SH current is generated. This leads to a diffusion of the spin into the normal region. We emphasize that this, previously unnoticed, mechanism of the spin injection is different from the one appearing at the boundary between materials with different intrinsic SOC and different elastic mean-free paths [50]. If the electric field is applied perpendicular to the interface, the situation is rather different. In this case, the BC impose the conservation of both the spin density and spin (diffusive) currents at the interface. This leads to a diffusion of the spin density induced via the inverse SGE into the normal conductor even in the absence of ESR mechanisms. For the specific case of a Rashba SOC, this result coincides with the one of Ref. [50].

Second, we address the inverse effect, i.e., the nonlocal SGE [see Fig. 1(d)]. In this case, a spin density is injected into the normal conductor at a certain distance from the interface. This spin diffuses over the normal region, and the corresponding spin diffusion current reaches the Rashba conductor, where it is transformed into a charge current. We demonstrate that depending on the polarization of the injected spin density, charge currents parallel or perpendicular to the interface can be generated. In the absence of ESR, the spatially integrated current parallel to the interface vanishes, leading to zero global SGE, whereas a finite ESR leads to a finite total charge current. These two situations are the reciprocal to the nonlocal inverse SGE described above. Indeed, we find a hitherto unknown general nonlocal reciprocity relation between the

[1]Our analysis is done within the diffusive limit and hence it is assumed that the spatial variation of the SOC occurs over a length scale larger than the momentum relaxation length. In this regard, we do not take into account so-called, interfacial SOC, i.e., SOC that only exists over atomic lengths right at the interface (see, for example, Refs. [61,63,64]).

global charge current induced by the spin injected locally at some point x_0, and the spin at the same point x_0 induced by applying a uniform electric field.

Finally, we consider the nonlocal SGE when the lateral dimensions are finite. In this case, no current flows at the lateral boundaries. We solve this boundary problem and find a redistribution of the electrochemical potential and the local charge currents flowing in the whole structure.

The paper is organized as follows. In Sec. II we review the SU(2)-covariant drift-diffusion equations for the charge and the spin densities, and derive the general BC. In Sec. III we first review the inverse SGE in bulk homogeneous systems with linear-in-momentum SOC. In Sec. III B we explore the nonlocal inverse SGE in the normal/Rashba conductor structure shown in Fig. 1(c). In Sec. IV we analyze at a general level the reciprocity between this effect and the nonlocal SGE, and show that the spin density at x_0, induced via the nonlocal inverse SGE, is proportional to the integrated charge current, generated via the nonlocal SGE, by injection of a spin current density at x_0. In Sec. V we study the nonlocal SGE shown in Fig. 1(d) and compute the spatial dependence of the charge current density. In Sec. VI we analyze the SGE in the same structure but with finite lateral dimensions, and determine the redistribution of charge currents and the electrochemical potential induced by the SGE. Finally, we present our conclusions in Sec. VII.

II. THEORETICAL DESCRIPTION OF DIFFUSIVE HYBRID STRUCTURES

In this section we review the diffusion equations for the charge and spin densities in homogeneous systems in the SU(2)-covariant formalism. We derive BC for these equations at hybrid interfaces. These conditions describe interfaces between materials with different kinds and strengths of linear-in-momentum SOC.

We focus on materials with linear-in-momentum SOC. The latter can be described with the help of a SU(2) vector potential $\hat{\mathscr{A}}_k = \frac{1}{2}\mathscr{A}_k^a\sigma^a$. Specifically, we consider the following Hamiltonian [47,52]:

$$H = \frac{(p_k - \hat{\mathscr{A}}_k)^2}{2m} - \hat{\mathscr{A}}_0 + V_{\rm imp}. \tag{1}$$

A particular case of SOC is the widely studied two-dimensional Rashba SOC, for which $\mathscr{A}_y^x = -\mathscr{A}_x^y = 2m\alpha = \lambda_\alpha^{-1}$, being α the Rashba parameter. The second term in Eq. (1), $\hat{\mathscr{A}}_0 = \frac{1}{2}\mathscr{A}_0^a\sigma^a$, describes a Zeeman or ferromagnetic exchange field. The last term is the potential of randomly distributed impurities. We consider both nonmagnetic and magnetic impurities, such that $V_{\rm imp} = V_{\rm nm} + V_{\rm m}$, where $V_{\rm nm}$ contains the SOC generated by the random potential of the impurities [1]. In our notation, lower indices correspond to spatial coordinates and upper indices to spin components, and throughout the paper the summation over repeated indices is implied.

The advantage of introducing the SOC as a SU(2) gauge field is that one can derive a SU(2)-covariant continuity equation for the spin [46]. In other words, within this formalism the spin is covariantly conserved when only intrinsic linear-in-momentum SOC is considered, and it satisfies the following continuity equation:

$$\tilde{\partial}_t\hat{S} + \tilde{\partial}_k\hat{j}_k = 0, \tag{2}$$

where $\hat{S} = S^a(\sigma^a/2)$ is the spin density and $\hat{j}_k = j_k^a(\sigma^a/2)$ is the spin current density flowing in the k direction, defined as the average of the spin current operator $j_k^a = (1/2)\{\partial H/\partial p_k, \sigma^a/2\}$. The spin continuity equation has the same form as the charge continuity equation, but with the derivatives substituted by the covariant ones $\tilde{\partial}_t = \partial_t - i[\hat{\mathscr{A}}_0, \cdot]$ and $\tilde{\partial}_k = \partial_k - i[\hat{\mathscr{A}}_k, \cdot]$, respectively.

In the presence of any kind of ESR, as for example magnetic impurities, or SOC due to the impurity scattering [24,52,53], Eq. (2) acquires an additional term:

$$\tilde{\partial}_t\hat{S} + \tilde{\partial}_k\hat{j}_k = -\frac{1}{\tau_{\rm ext}}\hat{S}. \tag{3}$$

Here, we assume that the spin relaxation is isotropic in space and neglect the interference term between extrinsic and intrinsic SOC [22]. Clearly, the ESR breaks the SU(2) symmetry and hence the spin is no longer covariantly conserved.

We now consider a hybrid interface between two materials with different mean-free path and SOC. In real systems, all potentials appearing in the Hamiltonian of Eq. (1) must be finite and, therefore, both the spin currents and spin densities must also be finite at any point in space. Therefore, one can integrate Eq. (3) over an infinitesimal interval across the interface and obtain the conservation of the spin current:

$$n_k j_k^a|_{0^+} = n_k j_k^a|_{0^-}, \tag{4}$$

where $\hat{\mathbf{n}} = (n_x, n_y, n_z)$ is a unit vector perpendicular to the interface. This is the first BC.

In order to describe the spatial distribution of the spin and charge densities, we focus here on diffusive systems in which the elastic scattering rate at nonmagnetic impurities dominates over all other rates. Specifically, the inverse of the momentum relaxation time τ^{-1} is assumed to be larger than all other energies, such as SOC, Zeeman field, or the inverse of any ESR time $\tau_{\rm ext}^{-1}$. In this limiting case, the spin current is given by [47,54,55]

$$\hat{j}_k = -D\tilde{\partial}_k\hat{S} - \gamma\hat{\mathscr{F}}_{ki}j_i. \tag{5}$$

The first term corresponds to the SU(2)-covariant diffusion current, where $D = v_{\rm F}^2\tau/d$ is the diffusion coefficient, and d the dimension of the system. The second term, proportional to the charge current density j_i, describes the charge-to-spin conversion, where $\gamma = \tau/(2m)$. It is, therefore, the term responsible for the SHE. The proportionality factor contains the field strength tensor defined in terms of the SU(2) vector potential as

$$\mathscr{F}_{ij}^a = \partial_i\mathscr{A}_j^a - \partial_j\mathscr{A}_i^a + \mathscr{A}_i^b\mathscr{A}_j^c\varepsilon^{abc}. \tag{6}$$

In analogy to the ordinary Hall effect, where electrons are deflected by an external magnetic field, the second term in the right-hand side of Eq. (5) describes the spin-dependent deflection in the presence of an effective SU(2) magnetic field, Eq. (6), generated by SOC.

The charge current density in the diffusive limit is given by [47,54]

$$j_k = -D\partial_k n - \sigma_{\rm D}E_k - \gamma\mathscr{F}_{ki}\hat{j}_i, \tag{7}$$

where n is the out-of-equilibrium electron density, σ_D the Drude conductivity, and E_k the kth component of the electric field. The third term is the reciprocal to the second term in Eq. (5). It describes the spin-to-charge conversion under the action of the SU(2) field and, therefore, is related to the inverse SHE.

The spin and charge diffusion equations are obtained by substituting expressions Eqs. (5) and (7) into Eq. (3) and the charge continuity equation, respectively. Specifically, the SU(2)-covariant spin diffusion equation in a stationary case and in the absence of a Zeeman field has the following compact form:

$$\tilde{\partial}_k D \tilde{\partial}_k \hat{S} + \gamma \tilde{\partial}_k \hat{\mathscr{F}}_{ki} j_i = \frac{1}{\tau_{\text{ext}}} \hat{S}. \tag{8}$$

The covariant Laplace operator in the first term can be written explicitly by expanding the covariant derivatives [56]:

$$(\tilde{\partial}_k D \tilde{\partial}_k)^{ab} = \partial_k D \partial_k \delta^{ab} + 2P_k^{ab}\partial_k + \partial_k P_k^{ab} - \Gamma^{ab}, \tag{9}$$

where we define the following operators [56]:

$$P_k^{ab} = -iD[\hat{\mathscr{A}}_k, \cdot] = D\mathscr{A}_k^c \varepsilon^{cba}, \tag{10}$$

$$\Gamma^{ab} = D[\hat{\mathscr{A}}_k, [\hat{\mathscr{A}}_k, \cdot]] = -D^{-1} P_k^{ac} P_k^{cb}. \tag{11}$$

Here, Γ^{ab} is the general Dyakonov-Perel relaxation tensor that describes spin relaxation due to the randomization of the spin precession caused by the scattering at nonmagnetic impurities, whereas P_k^{ab} describes the precession of an inhomogeneous spin density [25,56].

The spin diffusion equation (8) is solved in the next sections for different geometries and situations. To describe hybrid interfaces between different materials, one needs an additional BC to Eq. (4), which can be obtained by integrating Eq. (5) over a small interval around the interface. In the absence of charge current sources, this integration leads to the continuity of the spin density across the interface. If a finite charge current density is induced by an electric field $j_i = -\sigma_D E_i$, we divide Eq. (5) by D and integrate it over a small interval across the junctions and obtain

$$S^a\big|_{0^-}^{0^+} = \tfrac{1}{2}\big(\tfrac{\gamma\sigma_D}{D}\big|_{0^+} + \tfrac{\gamma\sigma_D}{D}\big|_{0^-}\big)(\delta_{ij} - n_i n_j)\big(\mathscr{A}_j^a|_{0^+} - \mathscr{A}_j^a|_{0^-}\big)E_i. \tag{12}$$

In this equation we allow for different values of the momentum scattering time τ and SOC at both sides of the junction, and different directions of the electric field with respect to the interface. Equation (12) generalizes the result for 2D Rashba systems [28,48–51], for any kind of linear-in-momentum SOC and any dimension [see Figs. 1(a) and 1(b)].

In the next sections we study nonlocal transport in the diffusive hybrid structure sketched in Figs. 1(c) and 1(d). It consists of a normal conductor without intrinsic SOC (gray area) adjacent to a conductor with Rashba SOC (blue area), from here on referred to as a *Rashba conductor*. As mentioned above, the Rashba SOC is described by the SU(2) vector potential with nonzero components $\mathscr{A}_y^x = -\mathscr{A}_x^y = 2m\alpha = \lambda_\alpha^{-1}$. In what follows, we assume that the momentum scattering time τ is constant in the whole system, and focus on the effect of ESR. Furthermore, we assume that the system is invariant in the y direction, such that the spin density only depends on x.

In the normal conductor region the spin current has only a diffusion contribution [first term of Eq. (5)], and the spin diffusion equation (8) has the same form for all spin components:

$$\partial_x^2 S^a = \frac{S^a}{\lambda_s^2}, \tag{13}$$

where λ_s is the spin diffusion length in the normal conductor.

In the Rahsba conductor, the three components of the spin current $\hat{j}_x$ are obtained from Eq. (5):

$$j_x^x = -D\partial_x S^x + \lambda_\alpha^{-1} S^z, \tag{14}$$

$$j_x^z = -D\partial_x S^z - \lambda_\alpha^{-1} S^x + \gamma\sigma_D \lambda_\alpha^{-2} E_y, \tag{15}$$

$$j_x^y = -D\partial_x S^y. \tag{16}$$

The components of the spin density are determined by the following set of coupled diffusion equations:

$$\partial_x^2 S^x = 2\lambda_\alpha^{-1}\partial_x S^z + \big(\lambda_\alpha^{-2} + \lambda_{\text{ext}}^{-2}\big)S^x - \frac{\gamma\sigma_D}{D}\lambda_\alpha^{-3} E_y, \tag{17}$$

$$\partial_x^2 S^z = -2\lambda_\alpha^{-1}\partial_x S^x + \big(2\lambda_\alpha^{-2} + \lambda_{\text{ext}}^{-2}\big)S^z, \tag{18}$$

$$\partial_x^2 S^y = \big(\lambda_\alpha^{-2} + \lambda_{\text{ext}}^{-2}\big)S^y + \frac{\gamma\sigma_D}{D}\lambda_\alpha^{-3} E_x. \tag{19}$$

Notice that for generality we assume different ESR lengths in the Rashba and in the normal conductor, λ_{ext} and λ_s, respectively.

We solve Eqs. (13) and (17)–(19) in two different situations. We first consider the inverse SGE [Fig. 1(c)]: a finite spin density is induced in the Rashba conductor due to the applied electric field. We explore whether such spin density can diffuse into the normal region. We then focus on the reciprocal situation [Fig. 1(d)] in which we assume that a spin density is created (e.g., by injection) at some point at the normal conductor and determine the charge current induced at the Rashba conductor via the SGE.

III. CHARGE-TO-SPIN CONVERSION: THE INVERSE SPIN-GALVANIC EFFECT

In this section we explore the charge-to-spin conversion in homogeneous and hybrid systems with intrinsic SOC. This conversion leads to the inverse SGE, which in the particular case of Rashba SOC is also called the Edelstein effect [23].

We start our discussion by analyzing this effect in a bulk material with intrinsic SOC. Even though this example has been widely studied in the literature [25,26,57], its discussion here will serve as good starting point to introduce the main physical parameters used in the subsequent analysis of a more complicated hybrid setup.

A. Homogeneous material with intrinsic SOC

The question under which conditions a charge current through a conductor with intrinsic linear-in-momentum SOC can create a transverse SH current was addressed in several works (see, e.g., Refs. [25,26,57]). Here, we show how the answer to this question can be found straightforwardly from the SU(2)-covariant spin diffusion equation.

In a bulk homogeneous system the spin density has no spatial dependence and, therefore, the diffusion equation reduces to an algebraic equation after setting the spatial derivatives in Eq. (8) to zero. In the presence of an external electric field, this equation reduces to

$$-\Gamma^{ab}S^b = \gamma\sigma_{\rm D}\mathscr{A}_k^b\mathscr{F}_{ki}^c\varepsilon^{abc}E_i + \frac{1}{\tau_{\rm ext}}S^a. \tag{20}$$

We first assume that $\tau_{\rm ext}^{-1} = 0$, and obtain

$$S_{\rm int}^a = \frac{\gamma\sigma_{\rm D}}{D}\mathscr{A}_i^a E_i. \tag{21}$$

The SH current, i.e., the spin current transverse to the applied electric field, is obtained from Eq. (5) and reads as

$$j_k^a = -D\mathscr{A}_k^c\varepsilon^{cba}\left(S^b - S_{\rm int}^b\right). \tag{22}$$

In the absence of ESR, $\hat{S} = \hat{S}_{\rm int}$, and hence no transverse current is generated. The spin current induced by the SU(2) magnetic field is fully compensated by the spin diffusive current. This also means that in a homogeneous finite system with intrinsic SOC, no spin accumulation at the boundary is expected. This can be seen as a direct consequence of the SU(2)-covariant conservation of the current, Eq. (2), which has to be zero at the sample boundaries.

The situation is quite different in the presence of a finite ESR. For the Rashba SOC the solution of Eq. (20) can be explicitly written:

$$S^a = \frac{S_{\rm EE}^a}{1 + r_{\rm ext}^2}, \tag{23}$$

where the parameter $r_{\rm ext} = \lambda_\alpha/\lambda_{\rm ext}$, with $\lambda_{\rm ext} = \sqrt{\tau_{\rm ext}D}$, characterizes the relative strength of ESR, and

$$S_{\rm EE}^a = \frac{\gamma\sigma_{\rm D}}{D\lambda_\alpha}\epsilon^{zai}E_i \tag{24}$$

is the well-known Edelstein result [16,23] for the current-induced spin in a Rashba conductor.[2]

Substitution of Eq. (24) into Eq. (22) leads to a finite SH current [52,58,59]:

$$j_k^z = \frac{D}{\lambda_\alpha}\frac{r_{\rm ext}^2}{1 + r_{\rm ext}^2}S_{\rm EE}^k. \tag{25}$$

The above results are used in the next sections to contrast them with those obtained for hybrid systems.

B. Hybrid structure with inhomogeneous SOC

We now focus on the hybrid diffusive structure sketched in Fig. 1(c). The structure can be viewed as a building block of a lateral spin valve [Fig. 1(b)], commonly used for nonlocal detection of magnetoelectric effects [8,60]. The charge-to-spin conversion can be detected by passing a charge current at the Rashba conductor [blue region in Fig. 1(b)]. This current generates a spin accumulation which can diffuse into the normal conductor (gray region) and can be detected as a spin voltage measured by a ferromagnetic electrode (orange region) [36].

In our model of Fig. 1(c), the normal conductor occupies the half-plane $x < 0$ and the Rashba conductor is at $x > 0$. We solve the diffusion equations in both regions [Eqs. (13) and (17)–(19)] together with the BC at $x = 0$ [Eqs. (4) and (12)].

In the normal conductor region $x < 0$, the solution of Eq. (13) is an exponential function decaying away from the interface over the spin diffusion length $\lambda_{\rm s}$. Whereas, the solution at the Rashba conductor depends on the direction of the applied electric field. We distinguish between two different situations: when the electric field is applied parallel or perpendicular to the interface.

1. *Electric field parallel to the interface:* $\mathbf{E} = E_y\hat{\mathbf{e}}_y$

If the electric field is applied parallel to the interface between the normal and Rashba conductors then, according to Eq. (24), the induced spin density in the bulk of the Rashba conductor is polarized perpendicular to **E**, which in our case corresponds to the direction S^x. From Eqs. (17) and (18) we see that the diffusion of this component is coupled to S^z, whereas the spin polarization in the y direction is not induced. Thus, one needs to solve two coupled linear second-order differential equations with BC at the interface between the normal and the Rashba conductors obtained from Eqs. (4) and (12):

$$j_x^a|_{0^+} = j_x^a|_{0^-}, \quad S^a|_{0^+} - S^a|_{0^-} = S_{\rm EE}^x\delta^{ax}. \tag{26}$$

The explicit form of the spatial dependence of S^x and S^z is given in Eq. (A1) of Appendix A and it is shown in Figs. 2(a) and 2(b), respectively, for $\lambda_{\rm ext} = \lambda_{\rm s}$. The obtained behavior can be easily understood from the bulk solution. When the ESR is negligibly small, $r_{\rm ext} \to 0$, the SH current is zero and the Edelstein spin density cannot diffuse into the normal conductor [solid blue line in Fig. 2(a)]. This is a consequence of the SU(2)-covariant conservation of the spin. Such conservation does not hold for a finite $r_{\rm ext}$. Indeed, ESR leads to a finite spin current in the Rashba conductor [Eq. (25)] and, consequently, the continuity of the spin current at the interface leads to a diffusive spin current in the normal conductor. This mechanism of spin injection into the normal conductor is different from the one discussed in Ref. [50], in which the spin injection takes place due to different momentum relaxation time at both sides of the interface.

As mentioned above, the precession terms in Eqs. (17) and (18) couple the S^x and S^z components and, therefore, both are induced in the whole system, as shown in Fig. 2(b). Far away from the interface inside the Rashba conductor, $x/\lambda_\alpha \gg 1$, the spin density reaches its bulk value given by Eq. (23).

One can obtain simple expressions for the spatial dependence of the spin density in limiting cases. For example, if the ESR is very small, $r_{\rm ext} \ll 1$, we obtain from Eq. (A1)

$$\begin{aligned}\frac{S^x(x)}{S_{\rm EE}^x} &\approx \Theta(x) - \Theta(-x)r_{\rm ext}^2 e^{\frac{x}{\lambda_{\rm s}}},\\ \frac{S^z(x)}{S_{\rm EE}^x} &\approx -r_{\rm ext}^2\left(\Theta(x)\,\mathbb{I}{\rm m}\left\{\frac{\kappa_0^{*2}}{2\sqrt{2}}e^{-\frac{\kappa_0 x}{\lambda_\alpha}}\right\} + \Theta(-x)e^{\frac{x}{\lambda_{\rm s}}}\right),\end{aligned} \tag{27}$$

[2]Notice that we distinguish between $S_{\rm int}$ and $S_{\rm EE}$ to emphasize that the latter is valid specifically for Rashba SOC. In contrast, $S_{\rm int}$ denotes the spin density induced by the electric field for any linear-in-momentum SOC.

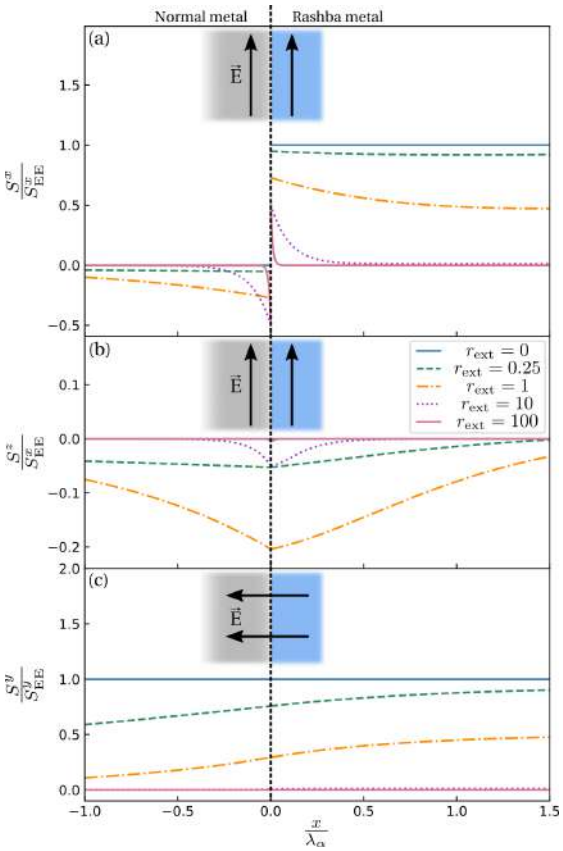

FIG. 2. Spatial dependence of the spin density induced by applying an electric field [see Fig. 1(c)] for different values of $r_{\rm ext}$. We distinguish two possible directions of the electric field: (a), (b) parallel, and (c) perpendicular to the interface. In all figures it is assumed that $\lambda_{\rm s} = \lambda_{\rm ext}$, and the calculated spin density is normalized by the corresponding bulk value $S^a_{\rm EE}$ of Eq. (24).

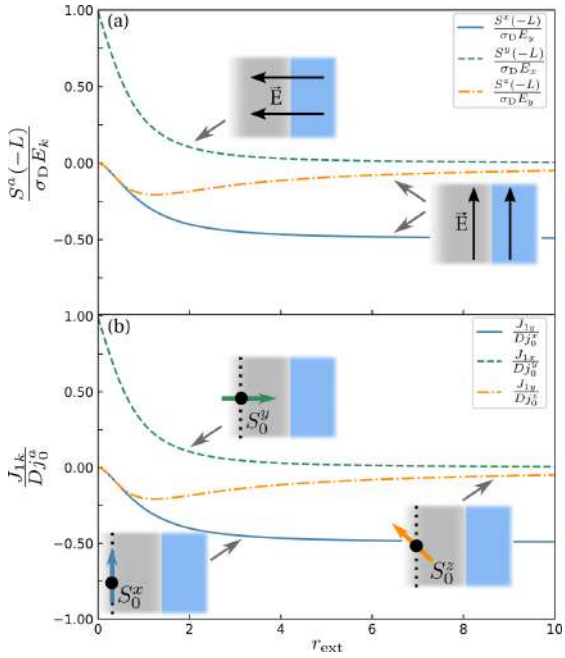

FIG. 3. (a) Spin density induced at $x = -L$ by an electric field [see Fig. 1(c)] as a function of $r_{\rm ext}$. We distinguish between an electric field applied parallel and perpendicular to the interface. (b) Integrated charge current induced by a spin density injection at $x = -L$ [see Fig. 1(d)] as a function of $r_{\rm ext}$. The charge current flows in different directions depending on the polarization of the injected spin density. All curves are calculated in units of $\gamma/(D\lambda_\alpha)$, for $L/\lambda_{\rm s} = 0.01$, $\lambda_{\rm s} = \lambda_{\rm ext}$, and normalized according to Eq. (43).

where $\kappa_0^2 = (-1 + i\sqrt{7})/2$, and corresponds to the definition of κ in Eq. (A2) with $r_{\rm ext} = 0$. This means that, to leading order in $r_{\rm ext}$, the Edelstein spin given by Eq. (23) is induced homogeneously in the Rashba conductor, whereas the amplitude of the spin density that diffuses into the normal region is proportional to $r^2_{\rm ext}$ [cf. Figs. 2(a) and 2(b)]. When $r_{\rm ext} = 0$, we recover the results obtained in Refs. [28,48].

In the opposite limit, i.e., when $r_{\rm ext} \gg 1$, we obtain from Eq. (A1)

$$\frac{S^x(x)}{S^x_{\rm EE}} \approx \frac{\lambda_{\rm s}}{\lambda_{\rm s} + \lambda_{\rm ext}} \left(\Theta(x) \frac{\lambda_{\rm ext}}{\lambda_{\rm s}} e^{-\frac{x}{\lambda_{\rm ext}}} - \Theta(-x) e^{\frac{x}{\lambda_{\rm s}}} \right),$$

$$\frac{S^z(x)}{S^x_{\rm EE}} \approx \frac{-1}{r_{\rm ext}} \frac{1 + \frac{\lambda_{\rm ext}}{\lambda_{\rm s}}}{\frac{\lambda^2_{\rm ext}}{\lambda^2_{\rm s}} + 2\frac{\lambda_{\rm ext}}{\lambda_{\rm s}} + 1} \left(\Theta(x) e^{-\frac{x}{\lambda_{\rm ext}}} + \Theta(-x) e^{\frac{x}{\lambda_{\rm s}}} \right). \quad (28)$$

In this case, the induced S^x is localized at the interface and decays exponentially into both conductors [cf. Fig. 2(a)]. The sign of the spin at both sides of the interface is opposite. If $\lambda_{\rm ext} = \lambda_{\rm s}$, as in Fig. 2, the value of the spin at each side of the interface is $\pm S^x_{\rm EE}/2$. Due to the Rashba coupling, a small contribution polarized in z also appears as shown in Fig. 2(b). If $\lambda_{\rm ext} \neq \lambda_{\rm s}$, we distinguish two cases: If $\lambda_{\rm s} \ll \lambda_{\rm ext}$, then the spin relaxes strongly in the normal conductor next to the interface. On the Rashba side, S^z practically disappears whereas there is an x-polarized spin accumulation at the edge of the order of $S^x_{\rm EE}$, which decays toward the bulk.

In the opposite limit $\lambda_{\rm s} \gg \lambda_{\rm ext}$, the spin density in the Rashba conductor is strongly suppressed by the ESR. Whereas, at the interface in the normal conductor side a spin density $S^x_{\rm EE}$ appears and decays over $\lambda_{\rm s}$ into the normal conductor.

The spin density induced in the normal conductor can be measured by detecting a spin voltage with a local ferromagnetic probe. We assume that such a contact is located at a distance L from the interface [see Figs. 1(b) and 1(c)]. In Fig. 3(a), we show the dependence on $r_{\rm ext}$ of both spin components (solid blue and dashed-dotted orange lines) induced in the normal conductor [Eq. (A1)] at the detector. We chose $\lambda_{\rm s} = \lambda_{\rm ext}$ and $L \ll \lambda_{\rm s}$. As explained above, in the absence of ESR, $r_{\rm ext} = 0$, the spin density induced by the charge current in the Rashba conductor does not diffuse into the normal part and hence both components are zero. For finite ESR, both

S^x and S^z become finite at $x = -L$, but their dependence on $r_{\rm ext}$ is quite different. The absolute value of S^x increases monotonically with $r_{\rm ext}$ and asymptotically approaches $S^x_{\rm EE}/2$, while S^z reaches a maximum at $r_{\rm ext} \approx 1$ and decays toward zero by further increase of $r_{\rm ext}$.

It is worth noticing that the situation of a parallel electric field explored in this section also corresponds to the experimental situation of Ref. [35]: a normal metal film Cu is in contact with an insulator Bi_2O_3 forming what the authors of that work called a Rashba interface. This setup is sketched in Fig. 1(a). If one assumes that the SOC is confined to the blue layer, and the electric field is applied along the films, then, in the absence of ESR, no spin current may flow from the interface into the Cu layer. Therefore, the observed magnetoresistance associated to a finite spin current cannot be only due to the Edelstein effect at the interface, but can be attributed to other extrinsic spin relaxation sources, as predicted from our previous analysis.

2. *Electric field perpendicular to the interface:* $\mathbf{E} = E_x\hat{\mathbf{e}}_x$

Now, we focus on the situation in which the electric field is applied perpendicular to the interface. According to Eq. (24), the induced spin density is polarized in the direction of $\hat{\mathscr{A}}_x$, which for Rashba SOC corresponds to S^y. This component is decoupled from the other two [see Eqs. (17)–(19)] and therefore in this case $S^{x,z} = 0$.

For the perpendicular orientation of the electric field, the BC correspond to the continuity of both the spin current and the spin density [Eqs. (4) and (12)]:

$$j^y_x|_{0^+} = j^y_x|_{0^-}, \quad S^y|_{0^+} = S^y|_{0^-}. \tag{29}$$

This means that the spin generated at the Rashba conductor via the Edelstein effect diffuses into the normal conductor, even in the absence of any ESR mechanism. From Eqs. (13), (19), and (29), one can determine explicitly the spatial dependence of S^y. In the normal conductor it reads as ($x < 0$)

$$S^y(x) = \frac{S^y_{\rm EE}}{\sqrt{1+r^2_{\rm ext}}} \frac{\lambda_s}{\lambda_\alpha + \lambda_s\sqrt{1+r^2_{\rm ext}}} e^{\frac{x}{\lambda_s}}, \tag{30}$$

and in the Rashba region ($x > 0$)

$$S^y(x) = \frac{S^y_{\rm EE}}{1+r^2_{\rm ext}} \left(1 - \frac{\lambda_\alpha}{\lambda_\alpha + \lambda_s\sqrt{1+r^2_{\rm ext}}} e^{-\frac{x}{\lambda_\alpha}\sqrt{1+r^2_{\rm ext}}}\right). \tag{31}$$

This result has to be contrasted to the one obtained when the field is applied parallel to the interface. Namely, in the latter case when $r_{\rm ext} = 0$ no spin diffuses into the normal conductor. Here, however, even if $r_{\rm ext} = 0$, the diffusion occurs as a consequence of the broken translation symmetry in the direction of the electric field.

In Fig. 2(c) we show the spatial dependence of S^y, assuming that the ESR in the normal and Rashba conductors are equal, $\lambda_s = \lambda_{\rm ext}$. As in Figs. 2(a) and 2(b), deep in the Rashba conductor $\frac{x}{\lambda_\alpha} \gg 1$, one obtains the bulk value for the spin density, determined by Eq. (23). Because of the continuity of the spin density, the increase of ESR leads to an overall homogeneous decrease of the spin density.

We compute the measurable spin density at a distance L from the interface [see Figs. 1(b) and 1(c)]. It is shown in Fig. 3(a) (dashed green line) for the particular case of $\lambda_s = \lambda_{\rm ext}$ and $L \ll \lambda_s$. Due to the latter condition, for $r_{\rm ext} = 0$ the spin density at $x = -L$ is approximately equal to $S^y_{\rm EE}$. When the ESR is switched on, the current-induced spin in the bulk Rashba conductor decreases monotonically according to Eq. (23), and so does the spin density value at $x = -L$.

The spin generated in the normal conductor is associated to a diffusive spin current j^y_x, parallel to the electric field as a consequence of the spatial variation of S^y [Eqs. (30) and (31)]. But, more interesting is the appearance of a SH current j^z_y, in the Rashba conductor as a consequence of both the covariant diffusion and the SU(2) magnetic field. This is a transverse to the electric field current and it can be calculated from Eq. (5):

$$j^z_y(x) = -\frac{D}{\lambda_\alpha}\left(S^y(x) - S^y_{\rm EE}\right), \tag{32}$$

which after substitution of $S^y(x)$ from Eq. (31) gives

$$j^z_y(x) = DS^y_{\rm EE}\left(\frac{r^2_{\rm ext}}{\lambda_\alpha\left(1+r^2_{\rm ext}\right)} + \frac{e^{-\frac{x}{\lambda_\alpha}\sqrt{1+r^2_{\rm ext}}}}{\lambda_\alpha + \lambda_s\sqrt{1+r^2_{\rm ext}}}\right). \tag{33}$$

The first term is the bulk solution of Eq. (25), whereas the second term is a correction due to the broken translation symmetry in the direction of the field. Interestingly, even in the absence of ESR, $r_{\rm ext} = 0$, there is a finite contribution to the SH current which is maximized at the interface and decays exponentially into the bulk. Such a localized SH current resembles the one obtained in Ref. [25] in a different geometry and for $r_{\rm ext} = 0$.

IV. RECIPROCITY BETWEEN THE NONLOCAL SPIN-GALVANIC EFFECT AND ITS INVERSE

In the previous section we discuss the nonlocal inverse SGE: a finite spin density, detectable in the normal conductor at a distance L from the interface [Figs. 1(b) and 1(c)] is induced as a response to an electric field applied both parallel and perpendicular to the interface. In the next section, we explore the reciprocal nonlocal effect, i.e., the charge current induced by a spin injection into the normal conductor [gray region in Figs. 1(b) and 1(d)]. Before analyzing this effect for this specific geometry, we examine the diffusion equation and identify a general nonlocal reciprocity between the spin induced by a charge current and the spatially integrated charge current induced by spin injection. We interpret this reciprocity as the nonlocal version of the reciprocity between the SGE and its inverse.

Our starting point is the general spin diffusion equation (8) that we rewrite as follows:

$$\left(D\tilde{\partial}_k\tilde{\partial}_k - \tau^{-1}_{\rm ext}\right)\hat{S} = \gamma\sigma_{\rm D}\tilde{\partial}_i\hat{\mathscr{F}}_{ik}E_k. \tag{34}$$

We assume, as before, that the SOC is inhomogeneous with a spatial variation over lengths larger than the mean-free path. As shown in Sec. II, the BC for hybrid interfaces can be obtained by integration of this equation. Here, instead, we keep the spatial dependence in the SU(2) fields and work with the general Eq. (34). We assume that the fields only vary in one direction, which we define as x. This is our only assumption. Thus, the diffusion equation reduces to a 1D linear differential equation. The solution can be written as

follows:

$$\hat{S}(x) = \gamma\sigma_{\rm D}E_k \int_{-\infty}^{\infty} \hat{G}(x,x')\tilde{\partial}_i\hat{\mathscr{F}}_{ik}(x')\,dx', \tag{35}$$

where the Green's function $\hat{G}$ satisfies

$$\left(D\tilde{\partial}_k\tilde{\partial}_k - \tau_{\rm ext}^{-1}\right)\hat{G}(x,x') = \delta(x-x'). \tag{36}$$

Equation (35) describes the nonlocal inverse SGE, i.e., the spin density created at x by a homogeneous electric field in the k direction.

We now consider the spin-to-charge conversion described by Eq. (7), which can be rewritten as

$$j_k = -\sigma_{\rm D}\partial_k\mu + j_{1k}, \tag{37}$$

where μ is the electrochemical potential defined by

$$\sigma_{\rm D}\partial_k\mu = D\partial_k n + \sigma_{\rm D}E_k, \tag{38}$$

and

$$j_{1k} = -\gamma\hat{\mathscr{F}}_{ik}\hat{j}_i \tag{39}$$

is the charge current density generated via the SOC. Here, j_i^a is the spin current originated from the covariant diffusion of S^a in the i direction and described by the first term in Eq. (5). We now integrate Eq. (39) over x and obtain

$$J_{1k} = \gamma D\int_{-\infty}^{\infty}\hat{\mathscr{F}}_{ki}\tilde{\partial}_i\hat{S}\,dx = \gamma D\int_{-\infty}^{\infty}\hat{S}\tilde{\partial}_i\hat{\mathscr{F}}_{ik}\,dx, \tag{40}$$

where the last equality follows from integration by parts. Equation (40) describes the charge current density generated by a spin density $\hat{S}$ and integrated over the direction of the spatial inhomogeneity. The spin density has to be calculated from the diffusion equation. Here, we assume that no electric field is applied, but instead a spin current $\hat{j}_0$ is injected locally at $x = x_0$. The diffusion equation (34) corresponding to this situation reads as

$$\left(D\tilde{\partial}_k\tilde{\partial}_k - \tau_{\rm ext}^{-1}\right)\hat{S} = \hat{j}_0\delta(x-x_0). \tag{41}$$

The solution to this equation can be written again in terms of the Green's function (36) as follows:

$$\hat{S}(x) = \hat{j}_0\hat{G}(x_0,x). \tag{42}$$

Substituting this result into Eq. (40), and comparing it with Eq. (35), leads to the following relation between the k component of the induced charge current and the a component of the induced spin density

$$\frac{J_{1k}}{Dj_0^a} = \frac{S^a(x_0)}{\sigma_{\rm D}E_k}. \tag{43}$$

That is a remarkable result that connects the integrated charge current induced by a spin current injected at $x = x_0$, with the spin density at x_0 induced by an applied electric field. This nonlocal reciprocity is a general property for any diffusive system with a 1D spatial inhomogeneity. It explains the identical curves shown in both panels of Fig. 3. Specifically, the result of Fig. 3(b) is discussed in the next section.

V. SPIN-TO-CHARGE CONVERSION: THE SPIN-GALVANIC EFFECT

We now verify the reciprocity demonstrated in the previous section by computing explicitly the nonlocal SGE in the setup sketched in Fig. 1(d). We assume that a spin current $\hat{j}_0$ is injected into the normal conductor at $x = -L$. Experimentally this can be done, for example, by injecting a current from a ferromagnetic lead [36,37]. We first solve the spin diffusion equations (13) and (17)–(19) together with the BC of Eqs. (4) and (12). Since $\mathbf{E} = 0$, the latter imply the conservation of the spin current and the spin density at the interface located at $x = 0$:

$$j_x^a|_{0^+} = j_x^a|_{0^-}, \quad S^a|_{0^+} = S^a|_{0^-}. \tag{44}$$

This continuity leads to the spin diffusion into the Rashba conductor for any polarization of the injected spin and strength of the ESR. At the injection point $x = -L$, the continuity of the spin density is assumed and, from Eq. (41),

$$j_x^a|_{-L^+} - j_x^a|_{-L^-} = j_0^a, \tag{45}$$

where j_0^a is the injected spin current. Again, in Eqs. (17)–(19) we see that the components S^x and S^z are coupled through the SOC whereas the S^y component is not. Therefore, in the next two subsections we distinguish between the injected spin current polarized in the x and z directions, and the injected current polarized in the y direction. As shown in Sec. IV, these two cases should be reciprocal to the results of Sec. III when the electric field was applied parallel or perpendicular to the interface, respectively.

A. Spin current polarized in the x or z direction

Let us assume that the spin current injected at $x = -L$ is polarized in the x or z direction and compute the charge current density induced in the Rashba conductor (39). Since the Rashba SOC is only finite at $x > 0$, this current flows in the y direction and consists of two contributions:

$$j_{1y}(x) = j_y^{\rm int} + j_y^{\rm bulk} = \frac{\gamma}{\lambda_\alpha}\left(\delta(x)j_x^x(x) + \Theta(x)\lambda_\alpha^{-1}j_x^z(x)\right), \tag{46}$$

with

$$j_x^x(x) = -D\left(\partial_x S^x - \frac{S^z}{\lambda_\alpha}\right) \quad \text{and} \quad j_x^z(x) = -D\left(\partial_x S^z + \frac{S^x}{\lambda_\alpha}\right) \tag{47}$$

from Eqs. (14) and (15). The explicit spatial dependence of S^x and S^z is given in Eq. (B1) of Appendix B. One of the contributions, $j_y^{\rm int}$, is localized at the interface, whereas the other one, $j_y^{\rm bulk}$, is finite at the Rashba conductor. In Fig. 4(a) we show the spatial dependence of the latter in the absence of ESR, $r_{\rm ext} = 0$. In view of the result of Sec. III B 1, at a first glance it might seem strange that, even though $r_{\rm ext} = 0$, a finite charge current density is induced in the system. However, as we have understood in the previous section with Eq. (43), the reciprocity involves the integrated current. Indeed, by substituting Eq. (B1) into (46), and performing the integration, one can demonstrate indeed that $J_{1y} = 0$ if $r_{\rm ext} = 0$.

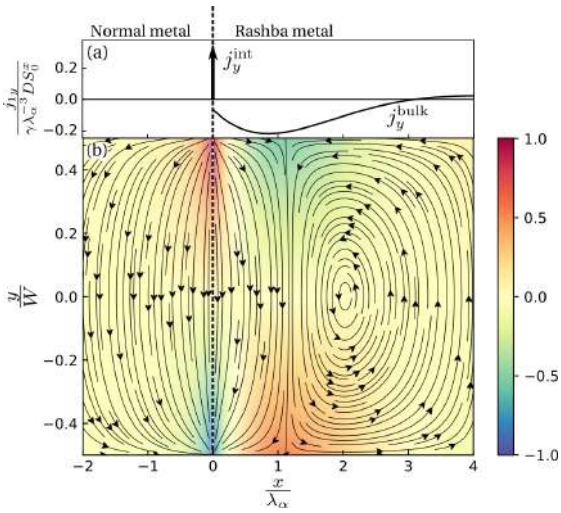

FIG. 4. (a) Spatial dependence of the charge current density j_{1y} induced by the Rashba SOC when the spin density injected at $x = -L$ is x polarized. The interfacial and bulk contributions can be distinguished. (b) Redistribution of the electrochemical potential μ due to the insulating boundaries placed at $y = \pm W/2$. The vector field lines correspond to the total charge current densities $\mathbf{j} = -\sigma_{\rm D}\nabla\mu + j_{1y}\hat{\mathbf{e}}_y$. Both plots are shown for pure Rashba SOC, $r_{\rm ext} = 0$, with $\lambda_\alpha/\lambda_{\rm s} = 0.1$, and $L/\lambda_{\rm s} = 0.1$.

In contrast, in the case of a finite $r_{\rm ext}$ one obtains a finite total current (see Appendix C)

$$J_{1y} = \gamma\lambda_\alpha^{-1}\int_0^\infty \frac{S^x}{\tau_{\rm ext}}dx. \tag{48}$$

This result is in accordance with the reciprocity relation (43) and the results of Sec. III B 1. In Fig. 3(b) we show the behavior of J_{1y} (solid blue and dashed-dotted orange lines) as a function of $r_{\rm ext}$. With the proper normalization imposed by Eq. (43), these curves are identical to those in Fig. 3(a).

B. Spin current polarized in the y direction

If the spin current injected at $x = -L$ is y polarized, only the S^y component is induced. This implies that only the longitudinal charge current density with $k = x$ in Eq. (39) is nonzero:

$$j_{1x} = -\Theta(x)\gamma\lambda_\alpha^{-2}j_y^z = \Theta(x)D\gamma\lambda_\alpha^{-3}S^y, \tag{49}$$

where we have used Eq. (5) for the spin current density. In the present geometry, only the commutator part of the covariant derivative contributes, such that the current j_y^z is proportional to S^y. The analytic expression for $S^y(x)$ is given in Eq. (B2) of Appendix B. In the region $x > 0$ it reads as

$$S^y(x) = \frac{\lambda_\alpha j_0^y}{D}\frac{e^{-\left(\sqrt{1+r_{\rm ext}^2}\frac{x}{\lambda_\alpha}+\frac{L}{\lambda_{\rm s}}\right)}}{r_{\rm s}+\sqrt{1+r_{\rm ext}^2}}. \tag{50}$$

According to Eq. (37), the charge current density is given by the contribution j_{1x} and the diffusive term

$$j_x = -\sigma_{\rm D}\partial_x\mu(x) + j_{1x}(x). \tag{51}$$

Because of the charge conservation, $\partial_x j_x = 0$ and the total charge current should be constant in space, $j_x = \text{const}$. The value of this constant is determined by the BC imposed on the outer boundaries of the system. For example, in a large, but finite, sample with floating edges, $j_x = 0$. This condition, together with Eq. (51), determines the distribution of the electrochemical potential $\mu(x)$ in the system:

$$\partial_x\mu(x) = \frac{1}{\sigma_{\rm D}}j_{1x}(x), \tag{52}$$

and eventually relates the voltage drop $\Delta\mu$ across the sample to the space-integrated induced current:

$$\Delta\mu = \frac{1}{\sigma_{\rm D}}\int j_{1x}dx \equiv \frac{1}{\sigma_{\rm D}}J_{1x}. \tag{53}$$

Notice that the integrated current J_{1x} is exactly the object entering the reciprocity relation of Eq. (43). In the present case, by using Eq. (49), and performing the integration, we find (see Appendix C)

$$J_{1x} = -\frac{\gamma j_0^y e^{-\frac{L}{\lambda_{\rm s}}}}{\lambda_\alpha\sqrt{1+r_{\rm ext}^2}(r_{\rm s}+\sqrt{1+r_{\rm ext}^2})}. \tag{54}$$

As in the charge-to-spin conversion case, Sec. III B 2, even if $\tau_{\rm ext}^{-1} \to 0$, the magnetoelectric effect does not vanish. In Fig. 3(b) we show J_{1x} (dashed green line) as a function of $r_{\rm ext}$. In agreement with Eq. (43), this curve coincides with the corresponding curve in Fig. 3(a).

VI. LOCAL CHARGE CURRENTS DUE TO THE SPIN-GALVANIC EFFECT IN A FINITE LATERAL GEOMETRY

In Sec. V A we have shown that the nonlocal spin injection in a system without ESR, $r_{\rm ext} = 0$, generates a distribution of local transverse charge currents which integrate to zero [see Fig. 4(a)]. Since the system was infinite in the y direction, such local currents flow in the y direction but do not depend on y. In contrast, if the system is finite in the lateral y direction, then the component j_y of the charge current density has to vanish at the lateral edges, and one expects a more complicated current pattern.

Here, we compute the local distribution of the charge current density and the electrochemical potential in a system of finite width W. We assume that the system has sharp boundaries at $y = \pm W/2$, and consider a particular case in which the injected spin current is polarized in the x direction, $j_0^a = \delta^{ax}j_0^x$ in Eq. (45).

In order to find the redistribution of the electrochemical potential, we need to solve the charge continuity equation $\partial_k j_k = 0$, with j_k of Eq. (37). This reduces to solving the Laplace equation for $\mu(\mathbf{r})$ with the BC of zero j_y at the boundaries $y = \pm W/2$. The corresponding boundary problem takes the following form:

$$\begin{aligned}&\partial_x^2\mu(x,y) + \partial_y^2\mu(x,y) = 0,\\ &\sigma_{\rm D}\partial_y\mu(x,y)|_{y=\pm\frac{W}{2}} = j_{1y}(x),\end{aligned} \tag{55}$$

where the second equation corresponds to zero charge current at the boundary, with $j_{1y}(x)$ from Eq. (46) and plotted in

Fig. 4(a). Notice that the latter has two different contributions: the interfacial $j_y^{\rm int}$ and the bulk one $j_y^{\rm bulk}$.

The boundary problem of Eq. (55) can be solved following the same procedure used in Ref. [61]. Here, we present the result in Fig. 4(b). The color plot shows the electrochemical potential, whereas the streamlines are the corresponding local charge current densities of Eq. (37). Interestingly, near the interface, where the term $j_y^{\rm int}$ of Eq. (46) is finite, the currents on both sides of the barrier tend to cancel it. In the Rashba conductor, the spatial distribution is more complicated and follows the $j_y^{\rm bulk}$ spatial behavior.

We explore here only the case $r_{\rm ext} = 0$. However, in the case of finite $r_{\rm ext}$ one expects a qualitatively similar behavior of the current patterns. The only difference is that, in that case, the integrated charge current would be finite in accordance with Eq. (48).

VII. CONCLUSIONS

In summary, we present an exhaustive analysis of nonlocal magnetoelectric effects in a system with an inhomogeneous linear-in-momentum SOC. Our study is based on the SU(2)-covariant drift-diffusion equations with an additional term describing the spin relaxation due to extrinsic processes. From the spin diffusion equation we obtain BC describing diffusive systems of any dimension with interfaces between conductors with different SOC and mean-free paths. One of these BC imposes the conservation of the spin current at the interface, whereas the second BC describes the jump of the spin density when an electric field is applied in the direction parallel to the interface. In contrast, for fields perpendicular to the interface, the second BC imposes the continuity of the spin density.

With the help of these BC we explore the nonlocal SGE and its inverse in a two-dimensional hybrid structure consisting of a conductor without SOC adjacent to Rashba conductor. First, we analyze the inverse SGE, i.e., the conversion of a charge current into a spin density. When the field is applied parallel to the interface between the two conductors and in the absence of ESR, the spin induced in the Rashba conductor does not diffuse into the normal conductor. However, for a finite $r_{\rm ext}$, a finite SH current appears and leads to a spin density diffusing into the normal conductor. In the case in which the field is applied perpendicular to the interface, the situation is rather different. In this case, the spin generated via the local inverse SGE always diffuses into the normal conductor.

We also study the reciprocal effect, ti.e., the SGE which is based on the spin-to-charge conversion. For a system with a 1D spatial inhomogeneity, we obtain from the spin diffusion equation a direct proportionality between the local spin induced by the inverse SGE and the spatially integrated charge current induced by the direct SGE [Eq. (43)]. This relation leads to a complete reciprocity between these two observables, and we use it to study the nonlocal SGE in the same setup. Finally, we compute the local currents and redistribution of the electrochemical potential, induced by the SGE in a system of finite lateral dimensions without ESR.

Our results are relevant for experiments on nonlocal magnetoelectric effects in hybrid structures which combine regions with different strengths of SOC, such as semiconducting [21], metal-insulator [35], and van der Waals heterostructures [62]. In the latter case, it is possible to build stacks of 2D materials, as for example graphene, such that the regions adjacent to a different material, for instance transition metal dichalcogenides, may exhibit sizable SOC [39–43]. In such structures, the SOC field is inhomogeneous in space and the electronic transport is governed by the effects discussed in this work.

ACKNOWLEDGMENT

We acknowledge funding by the Spanish Ministerio de Ciencia, Innovación y Universidades (MICINN) (Projects No. FIS2016-79464-P and No. FIS2017-82804-P) and by Grupos Consolidados UPV/EHU del Gobierno Vasco (Grant No. IT1249-19).

APPENDIX A: INVERSE SPIN-GALVANIC EFFECT: SPATIAL DEPENDENCE OF THE SPIN DENSITY

Here, we present the explicit form of the solution of the boundary problem solved in Sec. III. For an electric field applied parallel to the interface (Sec. III B 1), one needs to solve Eq. (13) in the normal conductor and Eqs. (17) and (18) in the Rashba region together with the BC (26). The solution for the spin densities is

$$\frac{S^x(x)}{S^x_{\rm EE}} = \frac{\Theta(x)}{1+r_{\rm ext}^2} - \frac{r_{\rm ext}^2}{1+r_{\rm ext}^2}\frac{\Theta(x)\,\mathbb{I}{\rm m}\left\{\left[\kappa^* + a^*\left(1+r_{\rm s}^2+\kappa^* r_{\rm s}\right)\right]e^{-\frac{\kappa x}{\lambda_\alpha}}\right\} + \Theta(-x)\,\mathbb{I}{\rm m}\{r_{\rm s}\kappa^* a + a|\kappa|^2 + \kappa|a|^2\}e^{\frac{x}{\lambda_{\rm s}}}}{\mathbb{I}{\rm m}\left\{[a(\kappa+r_{\rm s})-1](a^*+\kappa^*+r_{\rm s})\right\}},$$
$$\frac{S^z(x)}{S^x_{\rm EE}} = \frac{r_{\rm ext}^2}{1+r_{\rm ext}^2}\frac{\mathbb{I}{\rm m}\left\{\left(r_{\rm s}\kappa|a|^2+\kappa a^*\right)\left(\Theta(x)e^{-\frac{\kappa x}{\lambda_\alpha}}+\Theta(-x)e^{\frac{x}{\lambda_{\rm s}}}\right)\right\}}{\mathbb{I}{\rm m}\left\{[a(\kappa+r_{\rm s})-1](a^*+\kappa^*+r_{\rm s})\right\}}, \tag{A1}$$

with $r_{\rm s} = \lambda_\alpha/\lambda_{\rm s}$, and

$$a = \frac{2\kappa}{\kappa^2-\left(2+r_{\rm ext}^2\right)}, \qquad \kappa^2 = -\left(\tfrac{1}{2}-r_{\rm ext}^2\right) + \tfrac{\rm i}{2}\sqrt{7+16r_{\rm ext}^2}. \tag{A2}$$

In the main text, for Eq. (27) we use the value of κ_0 which equals to the κ defined above when $r_{\rm ext} = 0$.

APPENDIX B: SPIN-GALVANIC EFFECT: SPATIAL DEPENDENCE OF THE SPIN DENSITY

Here, we present the explicit form of the solution of the boundary problem solved in Sec. V. Specifically, one needs to solve Eqs. (13) in the normal conductor and Eqs. (17)–(19) in the Rashba region when $\mathbf{E} = 0$. At the boundary between the two regions, $x = 0$, we impose the continuity of the spin

currents and spin densities, and at $x = -L$ the condition (45). When the injected current j_0^a is polarized in $a = x$ or z directions, Sec. V A, the solution reads as

$$S^x(x) = \frac{\lambda_\alpha}{D}\left\{\frac{\mathbb{I}\mathrm{m}\left\{\left[\left(j_0^x a - j_0^z\right)(r_s+\kappa) - \left(j_0^x + j_0^z a\right)\right]e^{-\left(\frac{\kappa^* x}{\lambda_\alpha}+\frac{L}{\lambda_s}\right)}\right\}}{\mathbb{I}\mathrm{m}\left\{[a(\kappa+r_s)-1](a^*+\kappa^*+r_s)\right\}}\Theta(x)\right.$$
$$\left.+\left[\frac{\mathbb{I}\mathrm{m}\left\{j_0^x a(r_s+\kappa) - j_0^z(\kappa+a)\right\}}{\mathbb{I}\mathrm{m}\left\{[a(\kappa+r_s)-1](a^*+\kappa^*+r_s)\right\}}e^{\frac{x-L}{\lambda_s}} + \frac{j_0^x}{2r_s}\left(e^{-\frac{|x+L|}{\lambda_s}} - e^{\frac{x-L}{\lambda_s}}\right)\right]\Theta(-x)\right\},$$
$$S^z(x) = \frac{\lambda_\alpha}{D}\left\{\frac{\mathbb{I}\mathrm{m}\left\{\left[\left(j_0^x|a|^2 - j_0^z a^*\right)(r_s+\kappa) - \left(j_0^x a^* + j_0^z|a|^2\right)\right]e^{-\left(\frac{\kappa^* x}{\lambda_\alpha}+\frac{L}{\lambda_s}\right)}\right\}}{\mathbb{I}\mathrm{m}\left\{[a(\kappa+r_s)-1](a^*+\kappa^*+r_s)\right\}}\Theta(x)\right.$$
$$\left.+\left[\frac{\mathbb{I}\mathrm{m}\left\{a\left[j_0^z\left(r_s+\kappa^*\right) - j_0^x(\kappa^* a^* - 1)\right]\right\}}{\mathbb{I}\mathrm{m}\left\{[a(\kappa+r_s)-1](a^*+\kappa^*+r_s)\right\}}e^{\frac{x-L}{\lambda_s}} + \frac{j_0^z}{2r_s}\left(e^{-\frac{|x+L|}{\lambda_s}} - e^{\frac{x-L}{\lambda_s}}\right)\right]\Theta(-x)\right\}, \tag{B1}$$

with $r_s = \lambda_\alpha/\lambda_s$, and a, κ from Eq. (A2). On the other hand, when the injected spin current is polarized in the y direction (Sec. V A), one obtains

$$S^y(x) = \frac{j_0^y \lambda_\alpha}{D}\left[\frac{e^{-\left(\sqrt{1+r_{\mathrm{ext}}^2}\frac{x}{\lambda_\alpha}+\frac{L}{\lambda_s}\right)}}{r_s+\sqrt{1+r_{\mathrm{ext}}^2}}\Theta(x) + \left(\frac{r_s-\sqrt{1+r_{\mathrm{ext}}^2}}{2r_s\left(r_s+\sqrt{1+r_{\mathrm{ext}}^2}\right)}e^{\frac{x-L}{\lambda_s}} + \frac{1}{2r_s}e^{-\frac{|x+L|}{\lambda_s}}\right)\Theta(-x)\right]. \tag{B2}$$

APPENDIX C: INTEGRATED CHARGE CURRENT DENSITY

Here, we derive the expressions for the spatially integrated charge current density used in Sec. V [Eqs. (48) and (54)], but for linear-in-momentum SOC of any kind. The spatial variation of the SOC is a steplike function, and therefore the SU(2) field of Eq. (6) has a component localized right at the interface, $x = 0$, and another one homogeneous inside the Rashba conductor. Correspondingly, the charge current density j_{1k} in Eq. (37) has also an interfacial and a bulk contribution:

$$j_{1k} = -\gamma\left[\delta(x)\left(\mathscr{A}_i^a\delta^{kx} - \mathscr{A}_k^a\delta^{ix}\right) + \Theta(x)\mathscr{A}_k^c\mathscr{A}_i^b\varepsilon^{cba}\right]j_i^a. \tag{C1}$$

Integrating this equation over x gives

$$J_{1k} = -\gamma\left[\left(\mathscr{A}_i^a\delta^{kx} - \mathscr{A}_k^a\delta^{ix}\right)j_i^a|_0 + \int_0^\infty \mathscr{A}_k^c\mathscr{A}_i^b\varepsilon^{cba}\,j_i^a dx\right]. \tag{C2}$$

On the other hand, we can also integrate the continuity equation (3) over the semi-infinite Rashba conductor

$$\int_0^\infty \partial_x j_x^a dx + \int_0^\infty \mathscr{A}_k^c\, j_k^b\varepsilon^{cba}dx = -\int_0^\infty \frac{S^a}{\tau_{\mathrm{ext}}}dx,$$
$$\downarrow$$
$$j_x^a|_0^\infty + \int_0^\infty \mathscr{A}_k^c\, j_k^b\varepsilon^{cba}dx = -\int_0^\infty \frac{S^a}{\tau_{\mathrm{ext}}}dx, \tag{C3}$$

where in the second line we have used the fact that $j_x^a|_\infty = 0$. Substitution of Eq. (C3) into (C2) gives

$$J_{1k} = -\gamma\left(\mathscr{A}_i^a\delta^{kx}j_i^a|_0 - \mathscr{A}_k^a\int_0^\infty \frac{S^a}{\tau_{\mathrm{ext}}}dx\right). \tag{C4}$$

This expression is a general result for the integrated current in any hybrid structure composed of a normal and a linear-in-momentum SOC conductor with an interface at $x = 0$.

[1] I. Zutić, J. Fabian, and S. D. Sarma, Rev. Mod. Phys. **76**, 323 (2004).
[2] J. Sinova, S. O. Valenzuela, J. Wunderlich, C. H. Back, and T. Jungwirth, Rev. Mod. Phys. **87**, 1213 (2015).
[3] J. E. Hirsch, Phys. Rev. Lett. **83**, 1834 (1999).
[4] M. I. Dyakonov and A. V. Khaetskii, *Spin Physics in Semiconductors* (Springer, Berlin, 2017), Vol. 157.
[5] G. Vignale, J. Supercond. Novel Magn. **23**, 3 (2010).
[6] Y. K. Kato, R. C. Myers, A. C. Gossard, and D. D. Awschalom, Science **306**, 1910 (2004).
[7] V. Sih, R. C. Myers, Y. K. Kato, W. H. Lau, A. C. Gossard, and D. D. Awschalom, Nat. Phys. **1**, 31 (2005).
[8] S. O. Valenzuela and M. Tinkham, Nature (London) **442**, 176 (2006).
[9] T. Kimura, Y. Otani, T. Sato, S. Takahashi, and S. Maekawa, Phys. Rev. Lett. **98**, 156601 (2007).
[10] T. Seki, Y. Hasegawa, S. Mitani, S. Takahashi, H. Imamura, S. Maekawa, J. Nitta, and K. Takanashi, Nat. Mater. **7**, 125 (2008).
[11] E. Sagasta, Y. Omori, M. Isasa, M. Gradhand, L. E. Hueso, Y. Niimi, Y. C. Otani, and F. Casanova, Phys. Rev. B **94**, 060412(R) (2016).
[12] F. T. Vas'ko and N. A. Prima, Fiz. Tverd. Tela **21**, 1734 (1979) [Sov. Phys. Solid State **21**, 994 (1979)].
[13] Y. A. Bychkov and E. I. Rashba, J. Phys. C: Solid State Phys. **17**, 6039 (1984).

[14] G. Dresselhaus, Phys. Rev. **100**, 580 (1955).
[15] M. I. Dyakonov and V. I. Perel, Phys. Lett. A **35**, 459 (1971).
[16] A. G. Aronov and Y. B. Lyanda-Geller, Pis'Ma Zh. Eksp. Teor. Fiz. **50**, 398 (1989) [JETP Lett. **50**, 431 (1989)].
[17] A. G. Aronov, Y. B. Lyanda-Geller, and G. E. Pikus, Zh. Eksp. Teor. Fiz. **100**, 973 (1991) [Sov. Phys.–JETP **73**, 537 (1991)].
[18] W. Zhang, M. B. Jungfleisch, W. Jiang, J. E. Pearson, and A. Hoffmann, J. Appl. Phys. **117**, 17C727 (2015).
[19] V. Bel'kov and S. Ganichev, Semicond. Sci. Technol. **23**, 114003 (2008).
[20] L. E. Golub and E. L. Ivchenko, Phys. Rev. B **84**, 115303 (2011).
[21] M. Luengo-Kovac, S. Huang, D. Del Gaudio, J. Occena, R. S. Goldman, R. Raimondi, and V. Sih, Phys. Rev. B **96**, 195206 (2017).
[22] C. Gorini, A. Maleki Sheikhabadi, K. Shen, I. V. Tokatly, G. Vignale, and R. Raimondi, Phys. Rev. B **95**, 205424 (2017).
[23] V. M. Edelstein, Solid State Commun. **73**, 233 (1990).
[24] K. Shen, G. Vignale, and R. Raimondi, Phys. Rev. Lett **112**, 096601 (2014).
[25] E. G. Mishchenko, A. V. Shytov, and B. I. Halperin, Phys. Rev. Lett. **93**, 226602 (2004).
[26] R. Raimondi and P. Schwab, Phys. Rev. B **71**, 033311 (2005).
[27] J.-I. Inoue, G. E. W. Bauer, and L. W. Molenkamp, Phys. Rev. B **70**, 041303(R) (2004).
[28] R. Raimondi, C. Gorini, P. Schwab, and M. Dzierzawa, Phys. Rev. B **74**, 035340 (2006).
[29] O. V. Dimitrova, Phys. Rev. B **71**, 245327 (2005).
[30] N. P. Stern, S. Ghosh, G. Xiang, M. Zhu, N. Samarth, and D. D. Awschalom, Phys. Rev. Lett. **97**, 126603 (2006).
[31] S. D. Ganichev, E. L. Ivchenko, V. V. Bel'Kov, S. A. Tarasenko, M. Sollinger, D. Weiss, W. Wegscheider, and W. Prettl, Nature (London) **417**, 153 (2002).
[32] J. C. R. Sánchez, L. Vila, G. Desfonds, S. Gambarelli, J. P. Attané, J. M. De Teresa, C. Magén, and A. Fert, Nat. Commun. **4**, 2944 (2013).
[33] S. Karube, K. Kondou, and Y. Otani, Appl. Phys. Express **9**, 033001 (2016).
[34] M. Isasa, M. C. Martínez-Velarte, E. Villamor, C. Magén, L. Morellón, J. M. De Teresa, M. R. Ibarra, G. Vignale, E. V. Chulkov, E. E. Krasovskii, L. E. Hueso, and F. Casanova, Phys. Rev. B **93**, 014420 (2016).
[35] J. Kim, Y.-T. Chen, S. Karube, S. Takahashi, K. Kondou, G. Tatara, and Y. C. Otani, Phys. Rev. B **96**, 140409(R) (2017).
[36] F. J. Jedema, A. T. Filip, and B. J. Van Wees, Nature (London) **410**, 345 (2001).
[37] F. J. Jedema, H. B. Heersche, A. T. Filip, J. J. A. Baselmans, and B. J. Van Wees, Nature (London) **416**, 713 (2002).
[38] M. Johnson and R. H. Silsbee, Phys. Rev. Lett. **55**, 1790 (1985).
[39] C. Safeer, J. Ingla-Aynés, F. Herling, J. H. Garcia, M. Vila, N. Ontoso, M. R. Calvo, S. Roche, L. E. Hueso, and F. Casanova, Nano Lett. **19**, 1074 (2019).
[40] T. S. Ghiasi, A. A. Kaverzin, P. J. Blah, and B. J. van Wees, Nano Lett. **19**, 5959 (2019).
[41] L. Li, J. Zhang, G. Myeong, W. Shin, H. Lim, B. Kim, S. Kim, T. Jin, B. Kim, C. Kim *et al.*, arXiv:1906.10702.
[42] L. A. Benitez, W. S. Torres, J. F. Sierra, M. Timmermans, J. H. Garcia, S. Roche, M. V. Costache, and S. O. Valenzuela, arXiv:1908.07868.
[43] A. M. Hoque, D. Khokhriakov, B. Karpiak, and S. P. Dash, arXiv:1908.09367.
[44] Y. Niimi and Y. Otani, Rep. Prog. Phys. **78**, 124501 (2015).
[45] C. Gorini, P. Schwab, R. Raimondi, and A. L. Shelankov, Phys. Rev. B **82**, 195316 (2010).
[46] I. V. Tokatly, Phys. Rev. Lett. **101**, 106601 (2008).
[47] I. V. Tokatly, Phys. Rev. B **96**, 060502(R) (2017).
[48] Y. Tserkovnyak, B. I. Halperin, A. A. Kovalev, and A. Brataas, Phys. Rev. B **76**, 085319 (2007).
[49] İ. Adagideli, M. Scheid, M. Wimmer, G. E. W. Bauer, and K. Richter, New J. Phys. **9**, 382 (2007).
[50] A. Brataas, A. G. Mal'shukov, and Y. Tserkovnyak, New J. Phys. **9**, 345 (2007).
[51] L. Y. Wang and C. S. Chu, Phys. Rev. B **84**, 125327 (2011).
[52] R. Raimondi, P. Schwab, C. Gorini, and G. Vignale, Ann. Phys. **524** (2012).
[53] C. Huang, I. V. Tokatly, and F. S. Bergeret, Phys. Rev. B **98**, 144515 (2018).
[54] C. Gorini, U. Eckern, and R. Raimondi, Phys. Rev. Lett. **115**, 076602 (2015).
[55] F. Konschelle, I. V. Tokatly, and F. S. Bergeret, Phys. Rev. B **92**, 125443 (2015).
[56] F. S. Bergeret and I. V. Tokatly, Phys. Rev. B **89**, 134517 (2014).
[57] J. Sinova, D. Culcer, Q. Niu, N. A. Sinitsyn, T. Jungwirth, and A. H. MacDonald, Phys. Rev. Lett. **92**, 126603 (2004).
[58] O. Chalaev and D. Loss, Phys. Rev. B **71**, 245318 (2005).
[59] C. Gorini, P. Schwab, M. Dzierzawa, and R. Raimondi, Phys. Rev. B **78**, 125327 (2008).
[60] E. Villamor, M. Isasa, S. Vélez, A. Bedoya-Pinto, P. Vavassori, L. E. Hueso, F. S. Bergeret, and F. Casanova, Phys. Rev. B **91**, 020403(R) (2015).
[61] J. Borge and I. V. Tokatly, Phys. Rev. B **99**, 241401(R) (2019).
[62] A. K. Geim and I. V. Grigorieva, Nature (London) **499**, 419 (2013).
[63] J. Borge and I. V. Tokatly, Phys. Rev. B **96**, 115445 (2017).
[64] V. P. Amin, J. Zemen, and M. D. Stiles, Phys. Rev. Lett. **121**, 136805 (2018).

Chapter 5

Quantification of interfacial spin-charge conversion in hybrid devices with a metal/insulator interface

Applied Physics Letters ARTICLE scitation.org/journal/apl

Quantification of interfacial spin-charge conversion in hybrid devices with a metal/insulator interface

Cite as: Appl. Phys. Lett. **117**, 142405 (2020); doi: 10.1063/5.0023992
Submitted: 3 August 2020 · Accepted: 11 September 2020 ·
Published Online: 6 October 2020

Cristina Sanz-Fernández,[1,a)] Van Tuong Pham,[2,a)] Edurne Sagasta,[2] Luis E. Hueso,[2,3] Ilya V. Tokatly,[3,4,5,a)] Fèlix Casanova,[2,3,a)] and F. Sebastián Bergeret[1,5,a)]

AFFILIATIONS

[1]Centro de Física de Materiales (CFM-MPC), Centro Mixto CSIC-UPV/EHU, 20018 Donostia-San Sebastián, Basque Country, Spain
[2]CIC nanoGUNE, 20018 Donostia-San Sebastián, Basque Country, Spain
[3]IKERBASQUE, Basque Foundation for Science, 48013 Bilbao, Basque Country, Spain
[4]Nano-Bio Spectroscopy Group, Departamento de Física de Materiales, Universidad del País Vasco (UPV/EHU), 20018 Donostia-San Sebastián, Basque Country, Spain
[5]Donostia International Physics Center (DIPC), 20018 Donostia-San Sebastián, Basque Country, Spain

[a)]**Authors to whom correspondence should be addressed:** cristina_sanz001@ehu.eus; v.pham@nanogune.eu; ilya.tokatly@ehu.es; f.casanova@nanogune.eu; and fs.bergeret@csic.es

ABSTRACT

We present and experimentally verify a universal theoretical framework for the description of spin-charge interconversion in non-magnetic metal/insulator structures with interfacial spin–orbit coupling (ISOC). Our formulation is based on drift-diffusion equations supplemented with generalized boundary conditions. The latter encode the effects of ISOC and relate the electronic transport in such systems to spin loss and spin-charge interconversion at the interface. We demonstrate that the conversion efficiency depends solely on these interfacial parameters. We apply our formalism to two typical spintronic devices that exploit ISOC: a lateral spin valve and a multilayer Hall bar, for which we calculate the non-local resistance and the spin Hall magnetoresistance, respectively. Finally, we perform measurements on these two devices with a BiO_x/Cu interface and verify that transport properties related to the ISOC are quantified by the same set of interfacial parameters.

A thorough understanding of charge and spin transport in systems with spin–orbit coupling (SOC) is crucial for the electric control of spin currents.[1,2] The latter leads to the widely studied spin Hall effect (SHE)[3–5] and Edelstein (EE) effect,[6–9] which are at the basis of spin–orbit torque memories[10–12] and spin-based logic devices.[13,14]

Of particular interest are systems with spin-charge interconversion (SCI) at the interface between an insulator (I) with a heavy element and a normal metal (N) with negligible SOC and long spin relaxation length as, for example, BiO_x/Cu bilayers. In these systems, the SCI occurs at the hybrid interface via an interfacial spin–orbit coupling (ISOC).[15,16] Whereas the electronic transport in N is well described by customary drift-diffusion equations, the interfacial effects occur at atomic scales near the interface and, hence, their inclusion is more subtle. Some works use an intuitive picture based on an idealized 2DEG with Rashba SOC at the interface,[16–18] in which the interconversion takes place via the EE and its inverse (IEE). Such a description is clearly valid for conductive surface states in (e.g., topological) insulators[19,20] or 2DEGs.[21,22] However, in metallic systems, it requires additional microscopic parameters to model the coupling between interface states and the diffusive motion of electrons in the metal. Moreover, the very existence of a well-defined two-dimensional interface band and its relevance for the electronic transport in systems such as BiO_x/Cu is not obvious as realistic structures are frequently polycrystalline and disordered. Moreover, one can contemplate other microscopic scenarios to describe the SCI. For example, at the BiO_x/Cu interface, Bi atoms could diffuse into Cu inducing an effective extrinsic SHE in a thin layer near the interface.[23] Alternatively, a SCI can be generated via an interfacial spin-dependent scattering of the bulk Bloch states.[24–26] Each of these scenarios will invoke different sets of microscopic parameters to be inferred from macroscopic transport measurements.

In this Letter, we approach the problem from a different angle and propose a universal theoretical framework, which is independent

of microscopic details. We combine the drift-diffusion theory with effective boundary conditions (BCs)[27] to account for ISOC. Such BCs describe two types of interfacial processes: SCI and spin-losses, quantified, respectively, by the interfacial spin-to-charge/charge-to-spin conductivities, $\sigma_{sc/cs}$, and the spin-loss conductances $G_{\parallel/\perp}$ for spins polarized parallel/perpendicular to the interface. The SCI efficiency is determined by the ratio between the strengths of these two processes. This ratio coincides with the widely used conversion efficiency and the inverse Edelstein length λ_{IEE} such that $\lambda_{IEE} = \sigma_{sc}/G_{\parallel}$. Furthermore, we apply our theory to describe two typical experimental setups: non-local resistance measurement in a Permalloy/copper (Py/Cu) lateral spin valve (LSV) with a middle BiO_x/Cu wire, Fig. 2(a), and measurement of the spin Hall magnetoresistance (SMR) in a BiO_x/Cu/YIG trilayer Hall bar, Fig. 4(a). From the fitting of our theory to the experimental results, we show that both experiments are described by similar values of the ISOC parameters. This confirms that the SCI only depends on the intrinsic properties of the BiO_x/Cu interface. Moreover, we demonstrate that $\sigma_{sc} = \sigma_{cs}$, in accordance with Onsager reciprocity.

We start considering the I/N structure depicted in Fig. 1. In the N layer, spin and charge transport is described by the diffusion equations,

$$\nabla^2 \hat{\mu} = \frac{\hat{\mu}}{\lambda_N^2}, \tag{1}$$

$$\nabla^2 \mu = 0. \tag{2}$$

Here, $\hat{\mu} = (\mu^x, \mu^y, \mu^z)$ and μ are the spin and charge electrochemical potentials (ECP), where the symbol $\hat{}$ indicates spin pseudovector. It is assumed that N has inversion symmetry with an isotropic spin relaxation described by the spin diffusion length λ_N.[28] The diffusive charge and spin currents are defined as $e\hat{\mathbf{j}} = -\sigma_N \nabla \hat{\mu}$ and $e\mathbf{j} = -\sigma_N \nabla \mu$, respectively, with $e = -|e|$ and σ_N the conductivity of N.

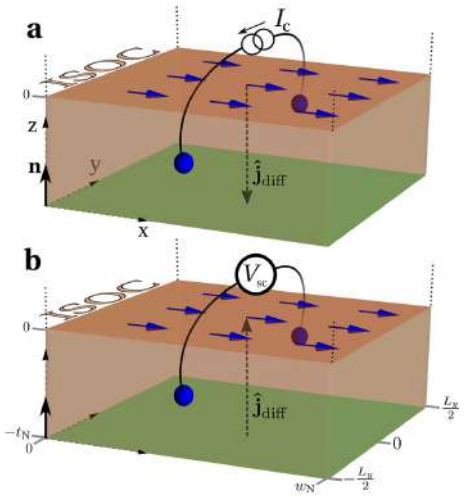

FIG. 1. Sketch of the non-magnetic insulator ($z > 0$)/metal ($z < 0$) system under study. ISOC is finite at the interface with normal vector $\mathbf{n}$. (a) Charge-to-spin conversion: a charge current I_c induces at the interface an out-of-plane spin current density $\hat{\mathbf{j}}_{diff}$ perpendicularly polarized. (b) Spin-to-charge conversion: a $\mathbf{n}$ injected spin current density $\mathbf{j}_{diff}$ induces at the interface a voltage drop perpendicular to the polarization of $\hat{\mathbf{j}}_{diff}$.

Equations (1) and (2) are complemented by BCs at the interfaces. At the interface with vacuum, one imposes a zero current condition, whereas at the I/N interface with ISOC, the BCs for the spin and charge densities read:[27]

$$-\sigma_N(\nabla \cdot \mathbf{n})\hat{\mu}|_0 = G_\perp \hat{\mu}_\perp|_0 + G_\parallel \hat{\mu}_\parallel|_0 + \sigma_{cs}(\mathbf{n} \times \nabla)\mu|_0, \tag{3}$$

$$-\sigma_N(\nabla \cdot \mathbf{n})\mu|_0 = \sigma_{sc}(\mathbf{n} \times \nabla)\hat{\mu}|_0. \tag{4}$$

Here, $\mathbf{n}$ is the unitary vector normal to the interface, see Fig. 1(a). The last term in the rhs of Eq. (3) describes the charge-to-spin conversion quantified by the conductivity σ_{cs}. This term couples an effective electric field and the (outgoing) spin current density at the interface[27,29–31] and can be interpreted as an interfacial SHE. Alternatively, it can be interpreted as if the electric field induces a homogeneous spin ECP via an interfacial EE, which in turn diffuses into N. Both interpretations are fully compatible within the present formalism. The second type of process taking place at the interface are spin-losses [first two terms in the rhs of Eq. (3)], quantified by the spin-loss conductances per area $G_{\perp/\parallel}$ for spins perpendicular/parallel ($\hat{\mu}_\perp/\hat{\mu}_\parallel$) to the interface.

The charge is obviously conserved and, therefore, the rhs of Eq. (4) only contains the spin-to-charge conversion term. The latter is the reciprocal of the last term in Eq. (3)[32] and can be interpreted as an interfacial inverse SHE but, again, an alternative interpretation is possible: from the conservation of the charge current at the interface, we can relate the bulk charge current to the divergence of an interfacial current $\mathbf{j}_I$ as $\sigma_N(\nabla \cdot \mathbf{n})\mu|_0 = -e\nabla \cdot \mathbf{j}_I$. Comparing the latter with Eq. (4), we define $\mathbf{j}_I$ as[33]

$$e\mathbf{j}_I = -\sigma_{sc}(\mathbf{n} \times \hat{\mu})|_0. \tag{5}$$

Written in this way, Eq. (4) describes the conversion of a non-equilibrium spin into an interfacial charge current, which corresponds to an interfacial IEE, see Fig. 1(b). This interpretation allows us to introduce the commonly used conversion length λ_{IEE}, defined as the ratio between the amplitude of the induced interfacial charge current density, $\mathbf{j}_I$, and the amplitude of the spin current injected from the bulk, $\sigma_N(\nabla \cdot \mathbf{n})\hat{\mu}|_0$. According to Eq. (5), the effect is finite only if the spin current is polarized in a direction parallel to the interface. Using Eqs. (3) and (5), we obtain

$$\lambda_{IEE} = \frac{\sigma_{sc}}{G_\parallel}. \tag{6}$$

This is a remarkable result that follows straightforwardly from our description of hybrid systems with ISOC and for which the spin-charge interconversion occurs only at the interface. λ_{IEE} is purely determined by interfacial parameters and it is indeed a quantification of the conversion efficiency: it is the ratio between the spin-to-charge conversion and the spin-loss at the interface. Both parameters, σ_{sc} and $G_\parallel$, depend on the microscopic properties of the interface, which are intrinsic for each material combination, and may depend on temperature.

From an experimental perspective, the spin-to-charge conversion is usually detected electrically, by measuring a voltage drop [see

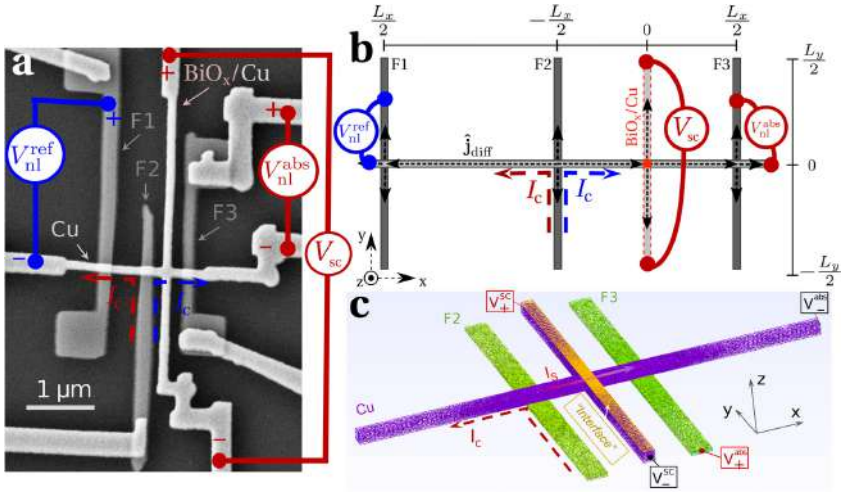

FIG. 2. (a) SEM image of the two Py/Cu LSVs, the reference one between ferromagnets F1–F2 and the one with a middle BiO$_x$/Cu wire (light red covering) between F2–F3. Non-local voltages V_{nl}^{ref} (blue circuit) and V_{nl}^{abs} (red circuit) are measured applying an external magnetic field (B) along the y axis. The spin-to-charge conversion voltage V_{sc} (red circuit) is detected applying B along the x axis. (b) Effective one-dimensional model of the device. (c) Geometry and mesh of the 3D finite element method model. The BiO$_x$/Cu interface is simulated as a thin layer (yellow) on top of the transverse Cu wire (purple).

Figs. 2(a) and 4(a)]. For concreteness, we consider the generic setup of Fig. 1(b): a spin current polarized in the x direction flows towards the interface, and a voltage difference is generated in the transverse y direction according to Eq. (5). The averaged voltage drop between the points $y = \pm L_y/2$ is given by (see supplementary material Note S1)

$$V_{sc} = \frac{\sigma_{sc}}{e\sigma_N A_N}\int\int_{-\frac{L_y}{2}}^{\frac{L_y}{2}} \left(\mathbf{n}\times\hat{\mu}|_0\right)\cdot\mathbf{e}_y\, dxdy, \tag{7}$$

where $\mathbf{e}_y$ is a unitary vector in the y direction and $A_N = t_N w_N$ is the wire cross section, with t_N and w_N being its thickness and width, over which the voltage drop is averaged. According to Eq. (7), the voltage drop between two points is proportional to the spin accumulation between them created via the ISOC. Next, we calculate the voltage drop associated with SCI in two different devices with an I/N interface.

We start analyzing the double Py/Cu LSV shown in Fig. 2(a) (see supplementary material Note S2 for experimental details). A charge current I_c is injected from the ferromagnetic injector F2 into the Cu wire. F2 forms a LSV either with the detector F1 or F3. We use the F1–F2 LSV as a reference device. In the F2–F3 LSV, there is an additional middle Cu wire covered by a BiO$_x$ layer, resulting in an I/N interface with ISOC, in which part of the spin current is absorbed and converted to a transverse charge current.

Quantitative description of electronic transport in LSVs has been widely studied in the literature.[34,35] In our Cu wires, $\lambda_N \gg t_N, w_N$, allowing us to simplify the ECPs diffusion to a one-dimensional problem,[34–36] see Fig. 2(b) and supplementary material Note S3. At the BiO$_x$/Cu wire, the z-integration using Eq. (3) leads to a renormalization of λ_N,

$$\lambda_{N\parallel} = \frac{\lambda_N}{\sqrt{1+\frac{G_\parallel \lambda_N^2}{\sigma_N t_N}}}. \tag{8}$$

At the node, $x = 0$ in Fig. 2(b), we use Kirchhoff's law for the spin currents (see supplementary material Note S3),

$$-A_N\sigma_N\partial_x\hat{\mu}_\parallel\big|_{0^-}^{0^+} = -G_{N\parallel}\hat{\mu}_\parallel|_{x=0} - A_n^{eff}\sigma_{cs}\frac{ej_c}{\sigma_N}\hat{\mathbf{e}}_x. \tag{9}$$

Here, $G_{N\parallel} = \frac{t_N\sigma_N A_n^{eff}}{\lambda_{N\parallel}^2}$ is the effective spin (bulk) conductance of the BiO$_x$/Cu wire, with $A_n^{eff} = w_N(w_N + 2\lambda_{N\parallel})$. The latter is the effective area of the BiO$_x$/Cu interface that absorbs (injects) spin current. Indeed, the rhs of this equation corresponds to Eq. (3) with an effective spin-loss conductance counting for both the interfacial and bulk spin-losses at the middle wire. The last term in Eq. (9) corresponds to the last term in Eq. (3) and it is proportional to the total injected charge current I_c along the middle wire oriented in the y direction. If we assume an homogeneously distribution of the current, then $\mathbf{j}_c = j_c\,\hat{\mathbf{e}}_y$, with $j_c = \frac{I_c}{A_N}$.

The Cu/Py interfaces are described by the following BC:[34,37,38]

$$\begin{aligned} -A_N\sigma_N\partial_x\hat{\mu}_\parallel\big|_{x=-\frac{L_x^-}{2}}^{x=-\frac{L_x^+}{2}} &= -A_F\left(\sigma_F^*\partial_y\hat{\mu}_{\parallel F2}|_{y=0} + p_F e j_c\right), \\ -A_N\sigma_N\partial_x\hat{\mu}_\parallel\big|_{x=-\frac{L_x^+}{2}}^{x=\frac{L_x^-}{2}} &= -A_F\sigma_F^*\partial_y\hat{\mu}_{\parallel F3}|_{y=0}, \end{aligned} \tag{10}$$

where $\hat{\mu}_{\parallel F2/F3}$ is the spin ECP at F2/F3, p_F the spin polarization, and $\sigma_F^* = \sigma_F(1-p_F^2)$ the effective conductivity of Py. L_x is the distance

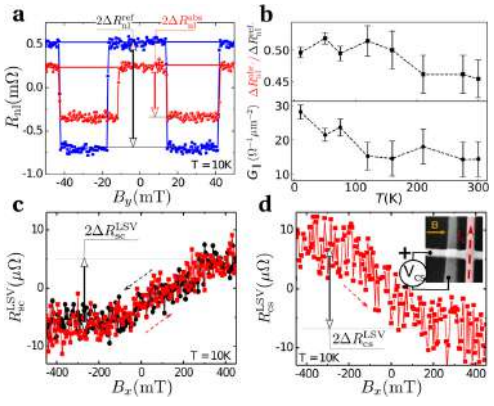

FIG. 3. (a) Non-local resistances as a function of B_y (trace and retrace) measured at $I_c = 70\ \mu$A and 10 K for the reference LSV (blue squares) and the BiO_x/Cu LSV (red circles). ΔR_{nl}^{ref} and ΔR_{nl}^{abs} are tagged. (b) Temperature dependence of the spin absorption ratio (upper panel) and the corresponding spin-loss conductance (lower panel). (c) and (d) Reciprocal SCI non-local resistances as a function of B_x (trace in red and retrace in black), from which we extract the spin-to-charge ($2\Delta R_{sc}^{LSV}$) from an average of seven sweeps and charge-to-spin ($2\Delta R_{cs}^{LSV}$) signals from an average of four sweeps, respectively. Measurements are performed at 10 K and $I_c = 70\ \mu$A (c) and $I_c = 150\ \mu$A (d).

between consecutive ferromagnetic wires and A_F the Py/Cu junction area.[34] For the reference LSV, we substitute F3 by F1 in Eq. (10). Because the Py/Cu interfaces are electrically transparent, we assume the continuity of $\hat{\mu}_\parallel$. This condition, together with the one-dimensional version of Eq. (1) and the BCs (9) and (10), determines the full spatial dependence of $\hat{\mu}_\parallel$.

Specifically, we need $\hat{\mu}_\parallel$ at the detector F1/F3 to determine the non-local voltage $V_{nl} = e^{-1} p_F \hat{\mu}_{\parallel F1/F3}|_{y=0}$[34,39] [see Fig. 2(b)] and the corresponding non-local resistance, $R_{nl} = V_{nl}/I_c$, where I_c is the current injected from F2. R_{nl} changes sign when the magnetic configuration of the ferromagnetic injector and detector changes from parallel, R_{nl}^{P}, to antiparallel, R_{nl}^{AP}. This allows us to remove any baseline resistance coming from non-spin related effects by taking $\Delta R_{nl} = R_{nl}^{P} - R_{nl}^{AP}$ [see Fig. 3(a)]. Comparing the resistance measured at F3, ΔR_{nl}^{abs}, with the one measured at F1, ΔR_{nl}^{ref}, we determine the magnitude of the spin absorption and, therefore, the value of the spin-loss conductance, $G_\parallel$. For this, we compute the ratio $\Delta R_{nl}^{abs}/\Delta R_{nl}^{ref} = \hat{\mu}_{\parallel F3}/\hat{\mu}_{\parallel F1}|_{y=0}$ by solving the full boundary problem,

$$\frac{\Delta R_{nl}^{abs}}{\Delta R_{nl}^{ref}} = \left[1 + \frac{G_{N\parallel}\,(G_F + 2G_N) - G_F\, e^{-\frac{L_N}{\lambda_N}}}{2G_N\,(G_F + 2G_N) + G_F\, e^{-\frac{L_N}{\lambda_N}}}\right]^{-1}. \quad (11)$$

Here, $G_i = \frac{\sigma_i A_i}{L_i}$ are the bare Cu ($i = N$) and Py ($i = F$) wires spin conductances. The form of Eq. (11) agrees with the one obtained in previous works.[35,38,40] However, our expression is more general since it distinguishes via $G_{N\parallel}$ between interfacial and bulk losses at the BiO_x/Cu wire. Consequently, we can ensure that our calculation of $G_\parallel$ and, therefore, λ_{IEE}, is only related to interfacial effects [see Eqs. (6), (8), and (9)].

Figure 3(b) shows a weak temperature dependence of the absorption ratio, $\Delta R_{nl}^{abs}/\Delta R_{nl}^{ref} \approx 0.5$, revealing that about half of the spin current is absorbed at the BiO_x/Cu middle wire. The temperature dependence of σ_N is measured (supplementary material Note S4), with $t_N = w_N = 80$ nm and $L_x = 570$ nm. The specific properties of the Py and Cu wires (ρ_F and p_F temperature dependencies and constant spin resistivities $\lambda_F/\sigma_F = 0.91\ f\Omega m^2$ and $\lambda_N/\sigma_N = 18.3\ f\Omega m^2$) are well characterized from our previous work.[41] Thereupon, by inserting these experimental values into Eq. (11) for different temperatures, we obtain the $G_\parallel$ dependence shown in Fig. 3(b). A slight decrease in $G_\parallel$ can be observed with increasing temperature, which seems to arise from the Cu conductivity. A linear relation between $G_\parallel$ and σ_N (see supplementary material Note S5A) suggests a Dyakonov–Perel mechanism of the spin-loss, expected for a Rashba interface and in agreement with Ref. 42.

We can also determine $\sigma_{sc/cs}$ in the same device. By injecting a charge current I_c from F2, an x-polarized spin current is created and reaches the BiO_x/Cu wire, where a conversion to a transverse charge current occurs via Eq. (5). This is detected as a non-local voltage V_{sc} along the BiO_x/Cu wire, determining the non-local resistance $R_{sc}^{LSV} = V_{sc}/I_c$ as a function of an in-plane magnetic field B_x. By reversing the orientation of the magnetic field, the opposite R_{sc}^{LSV} is obtained. The difference of the opposite values of R_{sc}^{LSV}, $2\Delta R_{sc}^{LSV}$ in Fig. 3(c), allows us to remove any baseline resistance. By swapping the voltage

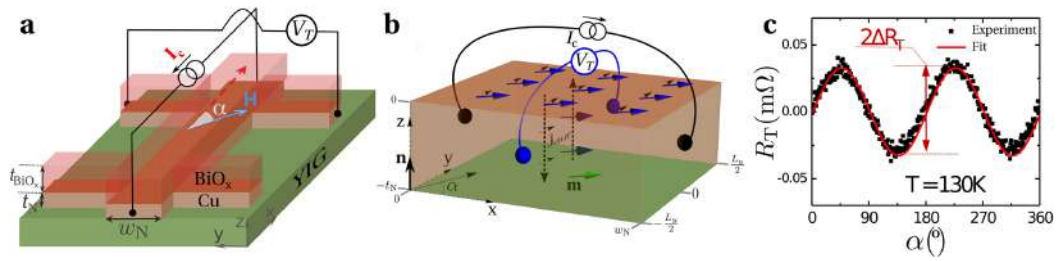

FIG. 4. (a) Measurement configuration of the TADMR in the BiO_x/Cu Hall-cross device on YIG. An in-plane B-field (100 mT) is rotated an angle (α) with respect to the applied current ($I_c = 5$ mA) direction. (b) Double SCI at the BiO_x/Cu interface. (c) Transverse resistance measured as a function of α (black squares). The solid red curve corresponds to a fit to Eq. (14).

and current probes, the reciprocal charge-to-spin conversion signal, $R_{cs}^{LSV} = V_{cs}/I_c$, can be determined.

Theoretically, from the full spatial dependence of $\hat{\mu}_\parallel$, we compute V_{sc} from Eq. (7) and V_{cs} from $V_{cs} = e^{-1} p_F \mu^x_{\parallel F2}|_{y=0}$, yielding

$$\Delta R_{sc/cs}^{LSV} = \pm \frac{\sigma_{sc/cs}}{\sigma_N} \frac{A_n^{eff}}{A_N} \frac{p_F e^{\frac{l_{sx}}{2\lambda_N}}}{G_F\left(1 - \frac{G_{N\parallel}}{2G_N}\right) + e^{\frac{l_{sx}}{\lambda_N}}(G_F + 2G_N)\left(1 + \frac{G_{N\parallel}}{2G_N}\right)}. \tag{12}$$

Experimentally, Figs. 3(c) and 3(d) confirm the reciprocity between both measurements, $\Delta R_{cs}^{LSV} = \Delta R_{sc}^{LSV}$. The broken time reversal symmetry, due to the magnetic contacts, leads to the opposite sign for reciprocal measurements. Contrasting this with the result of Eq. (12), one confirms that $\sigma_{sc} = \sigma_{cs}$.[43] The experimental value, $2\Delta R_{sc}^{LSV} \approx 15 \pm 3\,\mu\Omega$ at 10 K, yields $\sigma_{sc/cs} \approx 44 \pm 9\,\Omega^{-1}\mathrm{cm}^{-1}$ and $\lambda_{IEE} \approx 0.16 \pm 0.03$ nm. The latter value is of the same order of magnitude but somewhat smaller than the previously reported results obtained by spin pumping experiments, $\lambda_{IEE} \approx 0.2 - 0.7$ nm,[15,18,42] and LSV experiments, $\lambda_{IEE} \approx 0.5 - 1$ nm.[36] This discrepancy might be due to a different quality of the BiO_x/Cu interface: *ex situ* deposition in our experiment and *in situ* deposition in other works. The temperature dependence of the different parameters is presented in Note S5B in the supplementary material. One observes a decreasing trend of σ_{sc} by increasing the temperature, which translates in a decrease of λ_{IEE}, in agreement with the previous literature.[42]

The accuracy of our 1D model is checked by performing a 3D finite element method simulation detailed in supplementary material Note S6. Figure 2(c) shows the geometry of the simulated device and the mesh of the finite elements. The ISOC is simulated as a thin layer of finite thickness t_{int}, spin diffusion length λ_{int}, and a spin Hall angle θ_{int}^{eff}. From the definition $\lambda_{IEE} = \frac{1}{2}\theta_{int}^{eff} t_{int}$,[44] we obtain $\lambda_{IEE} = 0.10 \pm 0.02$ nm, in good agreement with our 1D model.

To verify that both ISOC parameters, $G_\parallel$ and σ_{sc}, are interface specific, we carry out another experiment involving a BiO_x/Cu interface. Namely, we measure the SMR in a Cu layer sandwiched between BiO_x (at $z = 0$) and $Y_3Fe_5O_{12}$ (YIG) insulating layers (at $z = -t_N$), shaped as a Hall bar, see Fig. 4(a) and supplementary material Note S2 for the experimental details. In this setup, a double SCI takes place as sketched in Fig. 4(b). A charge current I_c in the x direction induces an out-of-plane y-polarized spin current density via Eq. (3). This spin current propagates towards the Cu/YIG interface where it is partly reflected with mixed x and y polarizations.[45–47] The reflected spin current diffuses back to the BiO_x/Cu interface, where its x-polarized contribution is reciprocally converted to an interfacial charge current. The overall effect is then proportional to $\sigma_{cs}\sigma_{sc} = \sigma_{sc}^2$.

The electron spin reflection at the Cu/YIG interface depends on the direction of magnetization $\mathbf{m}$ of ferrimagnetic YIG. The effective BC describing this interface is known and reads[48,49]

$$-\sigma_N(\nabla \cdot \mathbf{n})\hat{\mu}|_{-t_N} = G_s\,\hat{\mu}|_{-t_N} + G_r\,\mathbf{m} \times (\hat{\mu} \times \mathbf{m})|_{-t_N} + G_i\,(\mathbf{m} \times \hat{\mu})|_{-t_N}. \tag{13}$$

Here, G_s is the so-called spin-sink conductance and $G_{r,i}$ are the real and imaginary parts of the spin-mixing conductance (per area), $G_{\uparrow\downarrow} = G_r + iG_i$. In YIG, $G_i \ll G_r$ and, hence, G_i is neglected.[47,50–52]

We measure the transverse angular dependent magnetoresistance (TADMR) in the BiO_x/Cu/YIG Hall bar of Fig. 4(a). The transverse voltage, V_T, depends on the direction of the in-plane applied magnetic field, parameterized by the angle α. The TADMR measurements are shown in Fig. 4(c).

Theoretically, we calculate the spatial dependence of $\hat{\mu}$ by solving the boundary problem of Eqs. (1), (3), and (13) by assuming translational invariance in the x–y plane. We then determine V_T from Eq. (7) and obtain for $R_T = V_T/I_c$,

$$R_T \approx \frac{\sigma_{sc}^2}{2\sigma_N^2 t_N^2} \frac{G_r}{(G_\parallel + G_s)(G_\parallel + G_s + G_r)} \sin(2\alpha) = \Delta R_T \sin(2\alpha). \tag{14}$$

Here, ΔR_T is the amplitude of the modulation and we assume that $\lambda_N \gg t_N$ (see supplementary material Note S7). The parameters of the Cu/YIG interface, $G_{r,s}$, add to the spin-loss at the BiO_x/Cu interface $G_\parallel$. We identify by comparison of Eqs. (3) and (13) two effective spin-loss conductances, $G_x = (G_\parallel + G_s)$ and $G_y = (G_\parallel + G_s + G_r)$, for spins polarized in the x and y directions, respectively. The amplitude of the SMR signal, Eq. (14), is then proportional to $G_x - G_y$.

From Fig. 4(c), we estimate $\Delta R_T \approx 0.03\,\mathrm{m}\Omega$ at $T = 130$ K. At this temperature, from the LSV measurements, we obtain $G_\parallel \approx 1.5 \times 10^{13}\,\Omega^{-1}\mathrm{m}^{-2}$ and $\sigma_{sc/cs} \approx 11.3\,\Omega^{-1}\mathrm{cm}^{-1}$, as shown in Figs. 3(b) and S3b, respectively. The spin conductances G_s and G_r in light metal/YIG interfaces have been estimated in evaporated Cu[53] and Al.[54] Whereas $G_s = 3.6 \times 10^{12}\,\Omega^{-1}\mathrm{m}^{-2}$ for Cu/YIG[53] is a consistent value in the literature,[54,55] the reported G_r is very low,[53] as generally observed in evaporated metals on YIG.[54,56] By substituting $G_\parallel$, G_s, and $\sigma_{sc/cs}$ values in Eq. (14), we obtain $G_r \approx 6.1 \times 10^{13}\,\Omega^{-1}\mathrm{m}^{-2}$. This value for sputtered Cu on YIG is much larger than that estimated in evaporated Cu on YIG, in agreement with the reported difference between sputtered and evaporated Pt.[56] Importantly, the obtained G_r satisfies the required condition $G_s < G_r$,[47,55] which confirms the validity of our estimation.

In summary, we present a complete theoretical framework based on the drift-diffusion equations to accurately describe electronic transport in systems with ISOC at non-magnetic metal/insulator interfaces. Within our model, the interface is described by two types of processes: spin-losses, parameterized by the interfacial conductances $G_{\parallel/\perp}$, and SCI, quantified by σ_{sc} and σ_{cs}. These parameters are material specific. The efficiency of the spin-to-charge conversion is quantified by the ratio $\sigma_{sc}/G_\parallel$, which coincides with the commonly used Edelstein length λ_{IEE}. The Onsager reciprocity[57–59] is directly captured by $\sigma_{sc} = \sigma_{cs}$, as demonstrated by comparing our theoretical and experimental results. Our theory is an effective tool for an accurate quantification of SCI phenomena at interfaces, which is of paramount importance in many spintronic devices. It is important to emphasize that the present formulation of our theory is valid for interfaces between non-magnetic materials. In principle, one could go beyond our theory and address the problem of magnetic moment transfer at a metal/magnetic insulator interface by including interfacial exchange interaction and magnon dynamics into the model.[47]

See the supplementary material for additional details on the derivation of the spin-to-charge averaged voltage, Eq. (7), and the renormalized spin diffusion length and node boundary condition for the LSV, Eqs. (8) and (9), respectively; measured temperature dependence of the Cu resistivity and analysis on the temperature dependence of

the ISOC parameters in the LSV; a brief explanation of the 3D simulation and the relation between the simulation and ISOC parameters; theoretical result for the transverse resistance measured in the multilayer Hall bar, i.e., which leads to Eq. (14); and the experimental details of the nanofabrication and measurements of the LSV and multilayer Hall bar devices.

AUTHORS' CONTRIBUTIONS

C.S-F. and V.T.P. contributed equally to this work.

C.S-F., F.S.B., and I.V.T. acknowledge funding from the Spanish Ministerio de Ciencia, Innovación y Universidades (MICINN) (Project Nos. FIS2016–79464-P and FIS2017–82804-P) and Grupos Consolidados UPV/EHU del Gobierno Vasco (Grant No. IT1249-19). The work of F.S.B. is partially funded by EU's Horizon 2020 research and innovation program under Grant Agreement No. 800923 (SUPERTED). The work at nanoGUNE is supported by Intel Corporation through the Semiconductor Research Corporation under MSR-INTEL TASK No. 2017-IN-2744 and the "FEINMAN" Intel Science Technology Center and by the Spanish MICINN under the Maria de Maeztu Units of Excellence Programme (No. MDM-2016–0618) and under Project Nos. MAT2015–65159-R and RTI2018–094861-B-100. V.T.P. acknowledges postdoctoral fellowship support from the "Juan de la Cierva–Formación" program by the Spanish MICINN (Grant No. FJCI-2017-34494). E.S. thanks the Spanish MECD for a Ph.D. fellowship (Grant No. FPU14/03102).

DATA AVAILABILITY

The data that support the findings of this study are available from the corresponding authors upon reasonable request.

REFERENCES

[1]I. Žutić, J. Fabian, and S. D. Sarma, Rev. Mod. Phys. **76**, 323 (2004).
[2]G. Vignale and J. Supercond, Nov. Magn. **23**, 3 (2010).
[3]J. Sinova, S. O. Valenzuela, J. Wunderlich, C. H. Back, and T. Jungwirth, Rev. Mod. Phys. **87**, 1213 (2015).
[4]S. O. Valenzuela and M. Tinkham, Nature **442**, 176 (2006).
[5]T. Kimura, Y. Otani, T. Sato, S. Takahashi, and S. Maekawa, Phys. Rev. Lett. **98**, 156601 (2007).
[6]A. Aronov and Y. B. Lyanda-Geller, JETP Lett. **50**, 431 (1989), available at http://www.jetpletters.ac.ru/ps/1132/article_17140.shtml.
[7]V. M. Edelstein, Solid State Commun. **73**, 233 (1990).
[8]Y. Ando and M. Shiraishi, J. Phys. Soc. Jpn. **86**, 011001 (2017).
[9]A. Soumyanarayanan, N. Reyren, A. Fert, and C. Panagopoulos, Nature **539**, 509 (2016).
[10]I. M. Miron, K. Garello, G. Gaudin, P.-J. Zermatten, M. V. Costache, S. Auffret, S. Bandiera, B. Rodmacq, A. Schuhl, and P. Gambardella, Nature **476**, 189 (2011).
[11]L. Liu, C.-F. Pai, Y. Li, H. Tseng, D. Ralph, and R. Buhrman, Science **336**, 555 (2012).
[12]C. Safeer, E. Jué, A. Lopez, L. Buda-Prejbeanu, S. Auffret, S. Pizzini, O. Boulle, I. M. Miron, and G. Gaudin, Nat. Nanotechnol. **11**, 143 (2016).
[13]V. T. Pham, I. Groen, S. Manipatruni, W. Y. Choi, D. E. Nikonov, E. Sagasta, C.-C. Lin, T. A. Gosavi, A. Marty, L. E. Hueso, I. A. Young, and F. Casanova, Nat. Electron. **3**, 309 (2020).
[14]S. Manipatruni, D. E. Nikonov, C.-C. Lin, T. A. Gosavi, H. Liu, B. Prasad, Y.-L. Huang, E. Bonturim, R. Ramesh, and I. A. Young, Nature **565**, 35 (2019).
[15]S. Karube, K. Kondou, and Y. Otani, Appl. Phys. Express **9**, 033001 (2016).
[16]J. Kim, Y.-T. Chen, S. Karube, S. Takahashi, K. Kondou, G. Tatara, and Y. Otani, Phys. Rev. B **96**, 140409 (2017).
[17]H. Nakayama, Y. Kanno, H. An, T. Tashiro, S. Haku, A. Nomura, and K. Ando, Phys. Rev. Lett. **117**, 116602 (2016).
[18]H. Tsai, S. Karube, K. Kondou, N. Yamaguchi, F. Ishii, and Y. Otani, Sci. Rep. **8**, 5564 (2018).
[19]J.-C. Rojas-Sánchez, S. Oyarzún, Y. Fu, A. Marty, C. Vergnaud, S. Gambarelli, L. Vila, M. Jamet, Y. Ohtsubo, A. Taleb-Ibrahimi, P. Le Fèvre, F. Bertran, N. Reyren, J.-M. George, and A. Fert, Phys. Rev. Lett. **116**, 096602 (2016).
[20]K. Kondou, R. Yoshimi, A. Tsukazaki, Y. Fukuma, J. Matsuno, K. Takahashi, M. Kawasaki, Y. Tokura, and Y. Otani, Nat. Phys. **12**, 1027 (2016).
[21]E. Lesne, Y. Fu, S. Oyarzun, J. Rojas-Sánchez, D. Vaz, H. Naganuma, G. Sicoli, J.-P. Attané, M. Jamet, E. Jacquet *et al.*, Nat. Mater. **15**, 1261 (2016).
[22]D. C. Vaz, P. Noël, A. Johansson, B. Göbel, F. Y. Bruno, G. Singh, S. Mckeown-Walker, F. Trier, L. M. Vicente-Arche, A. Sander *et al.*, Nat. Mater. **18**, 1187 (2019).
[23]Y. Niimi, Y. Kawanishi, D. H. Wei, C. Deranlot, H. X. Yang, M. Chshiev, T. Valet, A. Fert, and Y. Otani, Phys. Rev. Lett. **109**, 156602 (2012).
[24]J. Linder and T. Yokoyama, Phys. Rev. Lett. **106**, 237201 (2011).
[25]I. V. Tokatly, E. E. Krasovskii, and G. Vignale, Phys. Rev. B **91**, 035403 (2015).
[26]J. Borge and I. V. Tokatly, Phys. Rev. B **96**, 115445 (2017).
[27]J. Borge and I. V. Tokatly, Phys. Rev. B **99**, 241401 (2019).
[28]C. Sanz-Fernández, J. Borge, I. V. Tokatly, and F. S. Bergeret, Phys. Rev. B **100**, 195406 (2019).
[29]V. P. Amin, J. Zemen, and M. D. Stiles, Phys. Rev. Lett. **121**, 136805 (2018).
[30]V. P. Amin and M. D. Stiles, Phys. Rev. B **94**, 104420 (2016).
[31]V. P. Amin and M. D. Stiles, Phys. Rev. B **94**, 104419 (2016).
[32]Symmetry arguments alone cannot fix the relation between σ_{sc} and σ_{cs}.[27] However, we will see by contrasting theory with experiment, that reciprocity requires $\sigma_{sc} = \sigma_{cs}$.
[33]Notice that, in principle, an additional divergenceless term may appear in the rhs of Eq. (5). Indeed, as demonstrated in Ref. 27, symmetry allows for a term proportional to the out-of-plane component of the spin ECP. In the present work, we only consider spin polarization parallel to the I/N interface and, hence, we neglect that term.
[34]S. Takahashi and S. Maekawa, Phys. Rev. B **67**, 052409 (2003).
[35]Y. Niimi, H. Suzuki, Y. Kawanishi, Y. Omori, T. Valet, A. Fert, and Y. Otani, Phys. Rev. B **89**, 054401 (2014).
[36]H. Isshiki, P. Muduli, J. Kim, K. Kondou, and Y. Otani, preprint arXiv:1901.03095 (2019).
[37]V. T. Pham, L. Vila, G. Zahnd, A. Marty, W. Savero-Torres, M. Jamet, and J.-P. Attané, Nano Lett. **16**, 6755 (2016).
[38]T. Kimura, J. Hamrle, and Y. Otani, Phys. Rev. B **72**, 014461 (2005).
[39]T. Kimura, J. Hamrle, and Y. Otani, Appl. Phys. Lett. **85**, 3501 (2004).
[40]M. Isasa, M. C. Martínez-Velarte, E. Villamor, C. Magén, L. Morellón, J. M. De Teresa, M. R. Ibarra, G. Vignale, E. V. Chulkov, E. E. Krasovskii, L. E. Hueso, and F. Casanova, Phys. Rev. B **93**, 014420 (2016).
[41]E. Sagasta, Y. Omori, M. Isasa, Y. Otani, L. E. Hueso, and F. Casanova, Appl. Phys. Lett. **111**, 082407 (2017).
[42]H. Tsai, K. Kondou, and Y. Otani, Jpn. J. Appl. Phys., Part 1 **58**, 110907 (2019).
[43]In principle, any transport measurement in a system with a linear response will fulfill the Onsager reciprocity.[57–59] Within our theory, the global reciprocity is guarantied by $\sigma_{sc} = \sigma_{cs}$. Importantly, the global reciprocity does not imply a point-wise identity of the local current densities.
[44]J. R. Sánchez, L. Vila, G. Desfonds, S. Gambarelli, J. Attané, J. De Teresa, C. Magén, and A. Fert, Nat. Commun. **4**, 2944 (2013).
[45]Y.-T. Chen, S. Takahashi, H. Nakayama, M. Althammer, S. T. B. Goennenwein, E. Saitoh, and G. E. W. Bauer, Phys. Rev. B **87**, 144411 (2013).
[46]H. Nakayama, M. Althammer, Y.-T. Chen, K. Uchida, Y. Kajiwara, D. Kikuchi, T. Ohtani, S. Geprägs, M. Opel, S. Takahashi *et al.*, Phys. Rev. Lett. **110**, 206601 (2013).
[47]X.-P. Zhang, F. S. Bergeret, and V. N. Golovach, Nano Lett. **19**, 6330 (2019).
[48]A. Brataas, Y. V. Nazarov, and G. E. Bauer, Phys. Rev. Lett. **84**, 2481 (2000).
[49]Following our convention, the vector **n** normal to the interface, points from the Cu towards the insulating YIG layer.
[50]N. Vlietstra, J. Shan, V. Castel, J. Ben Youssef, G. E. W. Bauer, and B. J. van Wees, Appl. Phys. Lett. **103**, 032401 (2013).

[51]M. Althammer, S. Meyer, H. Nakayama, M. Schreier, S. Altmannshofer, M. Weiler, H. Huebl, S. Geprägs, M. Opel, R. Gross, D. Meier, C. Klewe, T. Kuschel, J.-M. Schmalhorst, G. Reiss, L. Shen, A. Gupta, Y.-T. Chen, G. E. W. Bauer, E. Saitoh, and S. T. B. Goennenwein, Phys. Rev. B **87**, 224401 (2013).
[52]T. Kosub, S. Vélez, J. M. Gomez-Perez, L. E. Hueso, J. Fassbender, F. Casanova, and D. Makarov, Appl. Phys. Lett. **113**, 222409 (2018).
[53]E. Villamor, M. Isasa, S. Vélez, A. Bedoya-Pinto, P. Vavassori, L. E. Hueso, F. S. Bergeret, and F. Casanova, Phys. Rev. B **91**, 020403 (2015).
[54]K. S. Das, F. K. Dejene, B. J. van Wees, and I. J. Vera-Marun, Appl. Phys. Lett. **114**, 072405 (2019).
[55]L. J. Cornelissen, K. J. H. Peters, G. E. W. Bauer, R. A. Duine, and B. J. van Wees, Phys. Rev. B **94**, 014412 (2016).
[56]N. Vlietstra, J. Shan, V. Castel, B. J. van Wees, and J. Ben Youssef, Phys. Rev. B **87**, 184421 (2013).
[57]H. B. G. Casimir, "On Onsager's principle of microscopic reversibility," Rev. Mod. Phys. **17**, 343–350 (1945).
[58]L. Onsager, "Reciprocal relations in irreversible processes. I," Phys. Rev. **37**, 405 (1931).
[59]L. Onsager, "Reciprocal relations in irreversible processes. II," Phys. Rev. **38**, 2265 (1931).

Chapter 6

Enhanced spin-orbit optical mirages from dual nanospheres

Enhanced spin-orbit optical mirages from dual nanospheres

Jorge Olmos-Trigo,[1] Cristina Sanz-Fernández,[2] Aitzol García-Etxarri,[1,2,3] Gabriel Molina-Terriza,[1,2,3] F. Sebastián Bergeret,[1,2] and Juan José Sáenz[1,3,*]

[1]*Donostia International Physics Center (DIPC), 20018 Donostia-San Sebastián, Spain*

[2]*Centro de Física de Materiales (CFM-MPC), Centro Mixto CSIC-UPV/EHU, 20018 Donostia-San Sebastián, Spain*

[3]*IKERBASQUE, Basque Foundation for Science, 48013 Bilbao, Spain*

(Received 13 July 2018; published 29 January 2019)

Spin-orbit interaction of light can lead to the so-called optical mirages, i.e., a perceived displacement in the position of a particle due to the spiraling structure of the scattered light. In electric dipoles, the maximum displacement is subwavelength and does not depend on the optical properties of the scatterer. Here we will show that the optical mirage in high refractive index dielectric nanoparticles depends strongly on the ratio between electric and magnetic dipolar responses. When the dual symmetry is satisfied (at the first Kerker condition), there is a considerable enhancement (far above the wavelength) of the spin-orbit optical mirage which can be related to the emergence of an optical vortex in the backscattering direction.

DOI: 10.1103/PhysRevA.99.013852

I. INTRODUCTION

It is customary to separate the angular momentum (AM) of light [1] into two contributions, the spin angular momentum (SAM) and the orbital angular momentum (OAM), that can be coupled by light propagation and scattering. The study of this spin-orbit interaction (SOI) has attracted a great deal of interest in recent years [2–5].

An interesting analogy between the SOI in light and the spin Hall effect (SHE) in electronic systems can be drawn [6,7]. In the latter, electrons with different spins are deflected differently by scattering off impurities due to the SOI. This leads to a transversal spin current that in turn induces a measurable spin accumulation at the sample edges. One of the microscopic origins of the SHE is the so-called side-jump mechanism [8], in which a spin-dependent displacement of the center of mass of the electronic wave packet takes place due to the SOI (for more details, we refer to the reviews [9,10]).

Similarly, an apparent transversal displacement of a target particle induced by light scattering can be explained by an AM exchange. Hereafter, this effect is referred to as an *optical mirage*. It has been observed in several situations, for example in beams impinging on a dielectric surface [11–13] or when considering a spherical target described by a single electric polarizability [14,15]. In the latter case, the apparent shift of the dipole localization does not depend on the optical properties but rather on the scattering angle, with opposite displacements for incident left and right circularly polarized photons (spins). The apparent shift (Δ) is maximized at the plane perpendicular to the direction of the incoming wave taking a value of $\Delta = \lambda/\pi$ [15], and thus, for circularly polarized light [16,17], it is always subwavelength. In contrast, for larger multipolar spheres, and certain combinations of radius and refractive index, resonant apparent shifts, reaching tens of wavelengths in magnitude, were found at some specific angles [18]. These results were interpreted [18] as a result of full transfer from SAM to OAM at those directions at which the scattered light is linearly polarized (where the SAM of scattered photons is identically zero).

In this paper, we demonstrate that by taking into account both the electric and magnetic dipoles sustained by a high refractive index (HRI) spherical particle, the subwavelength maximum limit can be drastically surpassed when the particle is excited by circularly polarized light. In other words, a large macroscopic apparent shift ($\Delta \gg \lambda$), even larger than those reported previously [18], is induced in the backscattering region. Specifically, we show that this optical mirage is related to the generation of a spiraling power flow and can be explained in terms of an angular momentum redistribution per photon between the SAM and OAM contributions.

In contrast with earlier work [18], we show that, for HRI dipolar spheres, the optical mirage is maximum at angles where the spin of the photons is sign-reversed, i.e. at directions at which the light is not linearly polarized.

Based on helicity conservation, we predict an intriguing enhancement of the momentum transfer when the system is dual, i.e., when the electric and magnetic dipolar moments are equal. At this so-called "first Kerker condition" [19–21], the scattered light is circularly polarized in all directions with a vanishing intensity in the backscattering direction. As we show, this leads to a huge apparent shift near backscattering associated with the appearance of a (2σ charge) topological optical vortex.

II. SYSTEM AND THEORETICAL METHODS

We consider a nonabsorbing dielectric sphere of radius a and refractive index n_p embedded in an otherwise homogeneous medium with constant and real refractive index n_h. The geometry of the scattering problem is sketched in Fig. 1, where we consider a circularly polarized plane wave with wave number $k = n_h k_0 = n_h 2\pi/\lambda_0$ (where λ_0 is the light wavelength in vacuum) and helicity $\sigma = \pm 1$ (we associate

*juanjo.saenz@dipc.org

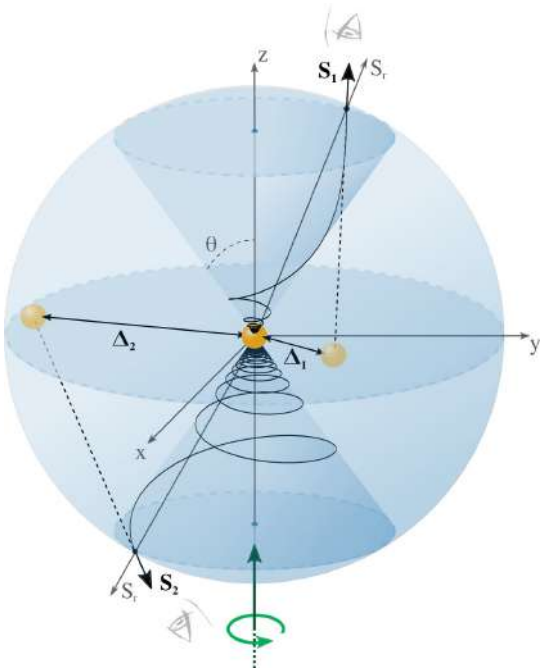

FIG. 1. Schematic representation of the optical mirage vector when considering a clockwise circularly polarized incoming wave (thick green straight arrow lying on the z-axis). The observer, represented by an eye, perceives a nonradial scattered Poynting vector ($\mathbf{S}_1, \mathbf{S}_2$) that leads to an apparent shift ($\mathbf{\Delta}_1, \mathbf{\Delta}_2$) of the dipole localization, both lying on the xy plane.

left polarized light with a positive helicity $\sigma = +1$) incident along the z-axis. Instead of using the traditional multipole Mie expansion to describe the light scattered by the sphere [22,23], we shall find it useful to work in a basis of multipoles, eigenfunctions, $\mathbf{\Psi}^{\sigma}_{lm}$, of the helicity operator Λ [24,25],

$$\mathbf{\Lambda}\mathbf{\Psi}^{\sigma}_{lm} = (1/k)\nabla \times \mathbf{\Psi}^{\sigma}_{lm} = \sigma\mathbf{\Psi}^{\sigma}_{lm},$$

with

$$\mathbf{\Psi}^{\sigma}_{lm} = \frac{1}{\sqrt{2}}\left[\frac{\nabla \times g_l(kr)\mathbf{X}_{lm}}{k} + \sigma g_l(kr)\mathbf{X}_{lm}\right], \tag{1}$$

$$g_l(kr) = A^{(1)}_l h^{(1)}_l(kr) + A^{(2)}_l h^{(2)}_l(kr), \tag{2}$$

$$\mathbf{X}_{lm} = \frac{1}{\sqrt{l(l+1)}}\mathbf{L}Y^m_l(\theta,\varphi), \tag{3}$$

where, following Jackson's notation [22], $\mathbf{X}_{lm}$ denote the vector spherical harmonic, where $\mathbf{X}_{00} = 0$, $g_l(kr)$ is a linear combination of the spherical Hankel functions, $Y^m_l(\theta,\varphi)$ are the spherical harmonics, and $\mathbf{L}$ is the orbital angular momentum operator, $\mathbf{L} = -i\ (\mathbf{r}\times\nabla)$. In this helicity basis, the incident field can be written as

$$\frac{\mathbf{E}^{(0)}_{\sigma}}{E_0} = \frac{\hat{\boldsymbol{x}} + \sigma i\hat{\boldsymbol{y}}}{\sqrt{2}}e^{ikz} = \sum_{l=0}^{\infty}\sum_{m=-l}^{+l}\sum_{\sigma'=\pm1} C^{\sigma\sigma'}_{lm}\mathbf{\Psi}^{\sigma'}_{lm}, \tag{4}$$

$$kZ\mathbf{H}^{(0)}_{\sigma} = -i\nabla\times\mathbf{E}^{(0)}_{\sigma}, \tag{5}$$

$$C^{\sigma\sigma'}_{lm} = \sigma i^l\sqrt{4\pi(2l+1)}\delta_{m\sigma}\delta_{\sigma\sigma'}, \tag{6}$$

where $1/Z = \epsilon_0 c n_h$ (where ϵ_0 and c are the vacuum permittivity and the speed of light, respectively) and $\mathbf{\Psi}^{\sigma'}_{lm}$ is given by Eq. (1) with $g_l(kr) = j_l(kr)$. Such a circularly polarized wave, with helicity σ, carries a $j_z = m = \sigma$ unit of total angular momentum per photon parallel to the propagation direction [22].

In the same basis, the scattered fields are given by

$$\frac{\mathbf{E}^{\text{scat}}_{\sigma}}{E_0} = \sum_{l=0}^{\infty}\sum_{m=-l}^{+l}\sum_{\sigma'=\pm1} D^{\sigma\sigma'}_{lm}\mathbf{\Psi}^{\sigma'}_{lm}, \tag{7}$$

$$D^{\sigma\sigma'}_{lm} = -i^l\sqrt{4\pi(2l+1)}\frac{\sigma a_l + \sigma' b_l}{2}\delta_{m\sigma}, \tag{8}$$

where now, since they are outgoing waves at infinity, $g_l(kr) = h^{(1)}_l(kr)$. Notice that a_l and b_l are the standard Mie electric and magnetic scattering coefficients [23]. Since a sphere presents axial symmetry around the z-axis, *the j_z of the incident beam is preserved* and the scattered wave can only involve $m = \sigma$. Consequently, $\mathbf{E}^{\text{scat}}_{\sigma}$ is an eigenfunction of the z-component of the total (dimensionless) angular momentum operator, $\mathbf{J} = \mathbf{L} + \mathbf{S}^{\text{spin}}$ (as well as of $\mathbf{J}^2$) [26], with eigenvalue $j_z = m = \sigma$,

$$\sigma = \frac{\mathbf{E}^{\text{scat}*}_{\sigma}\cdot\left(L_z + \mathbf{S}^{\text{spin}}_z\right)\mathbf{E}^{\text{scat}}_{\sigma}}{\left|\mathbf{E}^{\text{scat}}_{\sigma}\right|^2} = \ell_z(\mathbf{r}) + s_z(\mathbf{r}), \tag{9}$$

$$s_z(\mathbf{r}) = \frac{-i\left\{\mathbf{E}^{\text{scat}*}_{\sigma}\times\mathbf{E}^{\text{scat}}_{\sigma}\right\}\cdot\hat{\mathbf{e}}_z}{\left|\mathbf{E}^{\text{scat}}_{\sigma}\right|^2}, \tag{10}$$

$$\ell_z(\mathbf{r}) = \frac{\mathbf{E}^{\text{scat}*}_{\sigma}\cdot L_z\mathbf{E}^{\text{scat}}_{\sigma}}{\left|\mathbf{E}^{\text{scat}}_{\sigma}\right|^2} = \frac{-i}{\left|\mathbf{E}^{\text{scat}}_{\sigma}\right|^2}\left\{\mathbf{E}^{\text{scat}*}_{\sigma}\cdot\frac{\partial\mathbf{E}^{\text{scat}}_{\sigma}}{\partial\varphi}\right\}. \tag{11}$$

Equation (9) shows that the sum of the (dimensionless) OAM, $\ell_z(\mathbf{r})$, and SAM, $s_z(\mathbf{r})$, *per photon* is constant and equal to the helicity of the incoming plane wave. Notice that this is valid even in the near-field region, and it would be valid even in the presence of absorption. However, in general, the helicity is not preserved in the scattering process.

III. RESULTS AND DISCUSSION

Let us now consider the scattering from a HRI subwavelength sphere in a spectral range such that the optical response can be described by its first dipolar Mie coefficients a_1 and b_1, i.e., by its electric and magnetic polarizabilities $\alpha_{\text{E}} = ia_1(6\pi/k^3)$ and $\alpha_{\text{M}} = ib_1(6\pi/k^3)$. The scattered field can be written as the sum of two components with opposite helicity,

$$\begin{aligned}\frac{\mathbf{E}^{\text{scat}}_{\sigma}}{E_0} &= -\frac{k^3}{\sqrt{12\pi}}\{(\sigma\alpha_{\text{E}} + \alpha_{\text{M}})\mathbf{\Psi}^{+}_{1\sigma} + (\sigma\alpha_{\text{E}} - \alpha_{\text{M}})\mathbf{\Psi}^{-}_{1\sigma}\}\\ &= \mathbf{E}_{\sigma+} + \mathbf{E}_{\sigma-},\end{aligned} \tag{12}$$

which in the far-field limit become

$$\mathbf{E}_{\sigma\sigma'} \sim E_{\sigma\sigma'}e^{i\sigma\varphi}\left(\hat{\boldsymbol{e}}_{\sigma'} + i\sigma\frac{\sqrt{2}}{kr}\frac{\sigma\cos\theta - \sigma'}{\sin\theta}\hat{\boldsymbol{e}}_r + \cdots\right), \tag{13}$$

where the last identity corresponds to the medium–far-field expansion with

$$\frac{E_{\sigma\sigma'}}{E_0} = \frac{e^{ikr}}{4\pi kr} k^3 \left(\frac{\sigma\alpha_{\mathrm{E}} + \sigma'\alpha_{\mathrm{M}}}{2} \right) (\sigma \cos\theta + \sigma'), \quad (14)$$

$$\hat{\boldsymbol{e}}_{\sigma'} = \frac{1}{\sqrt{2}} (\hat{\boldsymbol{e}}_\theta + i\sigma' \hat{\boldsymbol{e}}_\varphi). \quad (15)$$

The scattered fields by HRI dielectric nanoparticles present a number of peculiar properties arising from the interference between the electric and magnetic dipolar radiation, and they have been largely discussed both theoretically and experimentally [27–33]. Most of these properties are encoded in the far-field radiation pattern, i.e., in the differential scattering cross section given by [20]

$$\frac{d\sigma_{\mathrm{scat}}(\theta)}{d\Omega} = \lim_{r\to\infty} r^2 \frac{\mathbf{S}^{\mathrm{scat}} \cdot \hat{\boldsymbol{e}}_r}{|\mathbf{S}^{(0)}|} = r^2 \frac{|E_{\sigma+}|^2 + |E_{\sigma-}|^2}{|E_0|^2}$$

$$= \frac{k^4 |\alpha_{\mathrm{sum}}|^2}{(4\pi)^2} \left(\frac{1 + \cos^2\theta}{2} + 2g\cos\theta \right), \quad (16)$$

where $\mathbf{S}^{\mathrm{scat}} = (1/2)\mathrm{Re}\{\mathbf{E}^{\mathrm{scat}*} \times \mathbf{H}^{\mathrm{scat}}\}$ is the time-averaged Poynting vector, $|\alpha_{\mathrm{sum}}|^2 \equiv |\alpha_{\mathrm{E}}|^2 + |\alpha_{\mathrm{M}}|^2$, and

$$g = \frac{\mathrm{Re}\{\alpha_{\mathrm{E}}\alpha_{\mathrm{M}}^*\}}{|\alpha_{\mathrm{sum}}|^2} \quad (17)$$

is the so-called asymmetry factor [23] for dipolar electric and magnetic scatterers [20,34].

Although in the strict far-field limit the flow lines of $\mathbf{S}^{\mathrm{scat}}$ lie along the spherical radial direction, tracing them to their source they do indeed spiral toward the origin in analogy with the light scattered by an electric dipole excited by circularly polarized light [15,18,35–37]. Consequently, as sketched in Fig. 1, the full Poynting vector $\mathbf{S}^{\mathrm{scat}}$ makes an angle with the line of sight, which determines an apparent shift $\boldsymbol{\Delta}$ in the perceived position of the particle, with

$$\boldsymbol{\Delta} = \lim_{kr\to\infty} -r \left(\frac{\mathbf{S}^{\mathrm{scat}} - \hat{\boldsymbol{e}}_r (\hat{\boldsymbol{e}}_r \cdot \mathbf{S}^{\mathrm{scat}})}{|\mathbf{S}_r|} \right) \quad (18)$$

$$= \lim_{kr\to\infty} \left(\frac{\hat{\boldsymbol{e}}_r \times (\mathbf{r} \times \mathbf{S}^{\mathrm{scat}})}{|\mathbf{S}_r|} \right) \quad (19)$$

$$= \lim_{kr\to\infty} \left(\frac{2i}{k |\mathbf{E}_\sigma^{\mathrm{scat}}|^2} \frac{\mathbf{E}_\sigma^{\mathrm{scat}*}}{\sin\theta} \cdot \frac{\partial \mathbf{E}_\sigma^{\mathrm{scat}}}{\partial\varphi} \right) \hat{\boldsymbol{e}}_\varphi, \quad (20)$$

where $\mathbf{E}_\sigma^{\mathrm{scat}}$ is given by Eqs. (12) and (13). Taking into account Eq. (11), the apparent shift can be written as

$$\frac{\boldsymbol{\Delta}}{(\lambda/\pi)} = -\frac{\ell_z(\theta)}{\sin\theta} \hat{\boldsymbol{e}}_\varphi = \frac{s_z(\theta) - \sigma}{\sin\theta} \hat{\boldsymbol{e}}_\varphi \quad (21)$$

$$= -\sigma \left[\frac{\sin\theta(1 + 2g\cos\theta)}{1 + \cos^2\theta + 4g\cos\theta} \right] \hat{\boldsymbol{e}}_\varphi. \quad (22)$$

This is the first important result of this paper: the shift is always along $\hat{\boldsymbol{e}}_\varphi$, perpendicular to the incidence plane and proportional to the z-component of the OAM per photon. Importantly, the sign of the displacement is purely determined by the incoming helicity.

In the absence of magnetic dipolar response, setting $g = 0$ in Eq. (22), one recovers the previously reported results for electric dipoles [15,18], which were interpreted as a result of transfer from SAM to OAM [18,38]. According to those previous works, this transfer is expected to be maximum at those directions at which the scattered light is linearly polarized (where the SAM of scattered photons is identically zero). For an electric dipole excited by circularly polarized light, the maximum transfer would take place in the plane perpendicular to the incoming light ($\theta = \pi/2$), where the maximum displacement is equal to $\Delta = \lambda/\pi$.

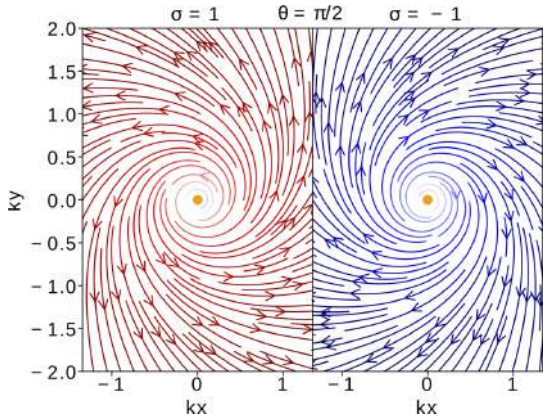

FIG. 2. Poynting vector streamlines with counterclockwise (clockwise) rotation for $\sigma = 1$ ($\sigma = -1$) when viewed from the perpendicular direction, $\theta = \pi/2$. The streamlines lie on the x-y plane (kx and ky are dimensionless variables, where $k = 2\pi/\lambda$ is the light wave number). This figure is valid for any dipolar response, i.e., arbitrary α_{E} and α_{M}. The small central circle represents the dipolar particle.

The fields scattered by electric and magnetic dipoles present a very different polarization structure [39,40]. Contrary to the purely electric (or magnetic) case, when excited with a circularly polarized field, the scattered radiation on the plane perpendicular to the incoming light ($\theta = \pi/2$) is no longer linearly polarized. Interestingly, this change does not affect the streamlines of the Poynting vector on this particular plane (as shown in Fig. 2), leading to the same subwavelength optical mirage. However, out of this plane the apparent displacement presents a peculiar behavior that depends strongly on both θ and the wavelength.

Figures 3 and 4 summarize the anomalous behavior of the apparent displacement $\Delta(\lambda, \theta)$ for silicon nanospheres in the infrared (similar behavior is obtained in other spectral ranges as long as the scattering cross section can be described by only the first two dipolar multipoles [see Fig. 3(a)]). As can be seen in Fig. 4, for $\theta = \pi/2$ the displacement is always λ/π for all wavelengths. When the asymmetry factor g is negative ($\lambda_{g1} < \lambda < \lambda_{g2}$), the maximum displacement occurs for $\theta < \pi/2$ and it is always subwavelength but slightly larger than the one for $\theta = \pi/2$. However, for $g > 0$ the apparent displacement can be much larger than λ/π, and when the electric and magnetic polarizabilities are identical ($\lambda = \lambda_{\mathrm{K1}}$), i.e., at the so-called first Kerker condition, it diverges as $\theta \to \pi$. Notice that the singularity is resolved naturally since at the first Kerker condition there is exactly zero backscattered intensity.

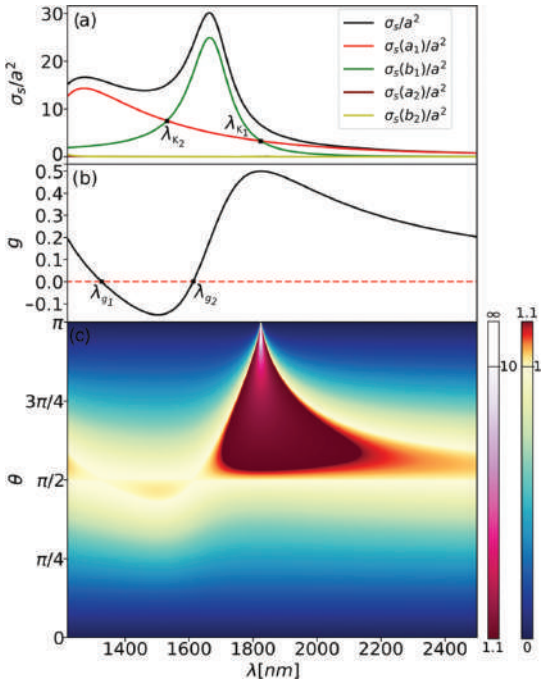

FIG. 3. (a) Scattering cross sections σ_s for a 230 nm Si nanosphere vs the wavelength. The special wavelengths $\lambda_{K_1} = 1825$ nm and $\lambda_{K_2} = 1520$ nm correspond to first and second Kerker conditions, respectively. (b) Asymmetry factor vs the wavelength. This is identical to zero at $\lambda_{g_1} = 1326$ nm and $\lambda_{g_2} = 1612$ nm (and negative in between). The maximum value is localized at the first Kerker condition, namely λ_{K_1}. (c) Colormap of the normalized optical mirage, $\Delta/(\lambda/\pi)$, vs the scattering angle and the wavelength. The maximum enhancement for λ_{K_1} at backscattering ($\theta = \pi$) is clearly observed.

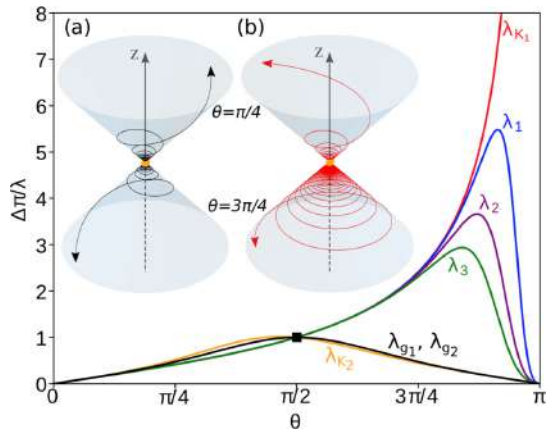

FIG. 4. Optical mirage colormap (Fig. 3) cuts vs the scattering angle for different values of the wavelength, belonging to regions with $g < 0$ (λ_{K_2}), $g = 0$ ($\lambda_{g_1}, \lambda_{g_2}$), and $g > 0$ (λ_1, λ_2, and λ_3, respectively decreased 5, 10, and 15 nm with respect to λ_{K_1}, and λ_{K_1} itself). At $\theta = \pi/2$, $\Delta = \lambda/\pi$ is observed to be a universal value. Both subplots show examples of trajectories of the Poynting vector at forward and backscattering, being similar for λ_{g_1} and λ_{g_2} (a) and considerably different for λ_{K_1} (b).

We can now examine the peculiar behavior of $\mathbf{\Delta}$ near the first Kerker condition in terms of the angular momentum flow. When the electric and magnetic responses are identical, i.e., $\alpha_E = \alpha_M$, the system is "dual" and the scattering preserves helicity [41,42]. In this case, the asymmetry factor is maximum, $g = 1/2$ [see Fig. 3(b)], which leads to $s_z(\theta) = \sigma \cos\theta$ and

$$\frac{\mathbf{\Delta}\pi}{\lambda_{K_1}} = -\sigma \tan\left(\frac{\theta}{2}\right)\hat{\boldsymbol{e}}_\varphi. \tag{23}$$

From this equation, two interesting limiting cases can be identified: First, in the forward direction the optical mirage and l_z go to zero since $\mathbf{S}_\varphi = \mathbf{0}$. This can alternatively be understood by means of the symmetries of the system: due to the duality of the scatterer, the system must conserve the helicity of the incoming field, which in the forward direction corresponds to the spin density. Thus, the incident circular polarization is preserved in the forward direction and must carry all the angular momentum density (leaving $\ell_z = 0$). Second, in the direction perpendicular to the incident wave vector ($\theta = \pi/2$), the interference term vanishes. As a consequence, $s_z = 0$ and $\ell_z = \sigma$, and, in analogy with electric dipoles, we obtain $\Delta = \sigma\lambda/\pi$, although in that case light in this direction is fully circularly polarized (see Fig. 2).

The most striking effect arises at an observation angle near backscattering $\theta \lesssim \pi$ where, as discussed above, the apparent displacement diverges. This divergence is solved because the Poynting vector becomes strictly zero at backscattering, which suggests the appearance of an optical vortex in that direction. As a matter of fact, near backscattering $\ell_z(\lesssim \theta) \to 2\sigma$, while the spin reverses sign $s_z(\theta \lesssim \pi) \to -\sigma$ (but still maintaining constant helicity), which confirms the existence of a vortex with $l = 2\sigma$ emerging from a nanoparticle as a nanoscale analog of the light backscattered from a perfect reflecting cone [43].

IV. CONCLUDING REMARKS

In conclusion, we have shown that light scattering from dipolar electric and magnetic nanoparticles, excited by circular polarized light, can lead to macroscopic apparent displacements of the particle position ("optical mirages") much larger than the incident wavelength. We derived an explicit relationship between the apparent shift and the z-component of the OAM per photon, ℓ_z. As a result of the interference between the fields scattered by the electric and magnetic dipoles, we found that ℓ_z presents a nontrivial dependence on the scattering angle, which, in contrast with previous work [18], leads to optical mirage maxima at angles where the spin of the photons is sign-reversed, i.e., at directions at which the light is not linearly polarized. Interestingly, for dual spheres, i.e., at the so-called first Kerker condition, we predict a huge enhancement of the apparent shift related to the emergence of an optical vortex in the backscattering direction. We believe that our results open new perspectives in the study of optical

spin-orbit phenomena, including new possible applications of HRI particles as building blocks in photonic devices.

ACKNOWLEDGMENTS

This research was supported by the Spanish Ministerio de Economía y Competitividad (MICINN) and European Regional Development Fund (ERDF) Projects No. FIS2014-55987-P, No. FIS2015-69295-C3-3-P, and No. FIS2017-82804-P, by the Basque Dep. de Educación Project No. PI-2016-1-0041 and by the Basque Government ELKARTEK program (KK-2016/00030, KK-2017/00089). A.G.-E. received funding from the Fellows Gipuzkoa fellowship of the Gipuzkoako Foru Aldundia through FEDER "Una Manera de hacer Europa."

J.O.-T. and C.S.-F. contributed equally to this work.

[1] L. Allen, S. M. Barnett, and M. J. Padgett, *Optical Angular Momentum* (CRC, Boca Raton, FL, 2003).
[2] V. S. Liberman and B. Y. Zel'dovich, Phys. Rev. A **46**, 5199 (1992).
[3] J. H. Crichton and P. L. Marston, Electron. J. Diff. Eqs. Conf. **04**, 37 (2000).
[4] M. Berry, M. Jeffrey, and M. Mansuripur, J. Opt. A **7**, 685 (2005).
[5] K. Y. Bliokh, F. Rodríguez-Fortuño, F. Nori, and A. V. Zayats, Nat. Photon. **9**, 796 (2015).
[6] M. Dyakonov and V. Perel, Phys. Lett. A **35**, 459 (1971).
[7] J. E. Hirsch, Phys. Rev. Lett. **83**, 1834 (1999).
[8] L. Berger, Phys. Rev. B **2**, 4559 (1970).
[9] M. I. Dyakonov and A. Khaetskii, in *Spin Physics in Semiconductors*, edited by M. I. Dyakonov (Springer-Verlag, Berlin, Heidelberg, 2008), pp. 211–243.
[10] J. Sinova, S. O. Valenzuela, J. Wunderlich, C. Back, and T. Jungwirth, Rev. Mod. Phys. **87**, 1213 (2015).
[11] M. Onoda, S. Murakami, and N. Nagaosa, Phys. Rev. Lett. **93**, 083901 (2004).
[12] K. Y. Bliokh and Y. P. Bliokh, Phys. Rev. Lett. **96**, 073903 (2006).
[13] O. Hosten and P. Kwiat, Science **319**, 787 (2008).
[14] C. Schwartz and A. Dogariu, Opt. Express **14**, 8425 (2006).
[15] H. F. Arnoldus, X. Li, and J. Shu, Opt. Lett. **33**, 1446 (2008).
[16] In contrast, the apparent shifts for electric dipolar particles illuminated by "*elliptically*" polarized fields can be much larger, as recently reported by Araneda *et al.* [17] after the submission of the present work.
[17] G. Araneda, S. Walser, Y. Colombe, D. Higginbottom, J. Volz, R. Blatt, and A. Rauschenbeutel, Nat. Phys. **15**, 17 (2019).
[18] D. Haefner, S. Sukhov, and A. Dogariu, Phys. Rev. Lett. **102**, 123903 (2009).
[19] M. Kerker, D.-S. Wang, and C. Giles, J. Opt. Soc. Am. A **73**, 765 (1983).
[20] M. Nieto-Vesperinas, R. Gomez-Medina, and J. J. Saenz, J. Opt. Soc. Am. A **28**, 54 (2011).
[21] R. Gomez-Medina, B. Garcia-Camara, I. Suárez-Lacalle, F. González, F. Moreno, M. Nieto-Vesperinas, and J. J. Sáenz, J. Nanophoton. **5**, 053512 (2011).
[22] J. D. Jackson, *Classical Electrodynamics* (Wiley, New York, 1999).
[23] C. F. Bohren and D. R. Huffman, *Absorption and Scattering of Light by Small Particles* (Wiley, New York, 2008).
[24] I. Fernandez-Corbaton, X. Zambrana-Puyalto, and G. Molina-Terriza, Phys. Rev. A **86**, 042103 (2012).
[25] X. Zambrana-Puyalto, I. Fernandez-Corbaton, M. Juan, X. Vidal, and G. Molina-Terriza, Opt. Lett. **38**, 1857 (2013).
[26] N. Tischler, X. Zambrana-Puyalto, and G. Molina-Terriza, Eur. J. Phys. **33**, 1099 (2012).
[27] A. B. Evlyukhin, C. Reinhardt, A. Seidel, B. S. Luk'yanchuk, and B. N. Chichkov, Phys. Rev. B **82**, 045404 (2010).
[28] A. García-Etxarri, R. Gómez-Medina, L. S. Froufe-Pérez, C. López, L. Chantada, F. Scheffold, J. Aizpurua, M. Nieto-Vesperinas, and J. J. Sáenz, Opt. Express **19**, 4815 (2011).
[29] J.-M. Geffrin, B. García-Cámara, R. Gómez-Medina, P. Albella, L. S. Froufe-Pérez, C. Eyraud, A. Litman, R. Vaillon, F. González, M. Nieto-Vesperinas, J. J. Sáenz, and F. Moreno, Nat. Commun. **3**, 1171 (2012).
[30] S. Person, M. Jain, Z. Lapin, J. J. Sáenz, G. Wicks, and L. Novotny, Nano Lett. **13**, 1806 (2013).
[31] Y. H. Fu, A. I. Kuznetsov, A. E. Miroshnichenko, Y. F. Yu, and B. Luk'yanchuk, Nat. Commun. **4**, 1527 (2013).
[32] L. Shi, J. T. Harris, R. Fenollosa, I. Rodriguez, X. Lu, B. A. Korgel, and F. Meseguer, Nat. Commun. **4**, 1904 (2013).
[33] A. I. Kuznetsov, A. E. Miroshnichenko, M. L. Brongersma, Y. S. Kivshar, and B. Luk'yanchuk, Science **354**, aag2472 (2016).
[34] R. Gómez-Medina, L. S. Froufe-Pérez, M. Yépez, F. Scheffold, M. Nieto-Vesperinas, and J. J. Sáenz, Phys. Rev. A **85**, 035802 (2012).
[35] W. Gough, Eur. J. Phys. **7**, 81 (1986).
[36] H. F. Arnoldus and J. T. Foley, Opt. Commun. **231**, 115 (2004).
[37] C. Schwartz and A. Dogariu, Opt. Lett. **31**, 1121 (2006).
[38] K. Y. Bliokh, E. A. Ostrovskaya, M. A. Alonso, O. G. Rodríguez-Herrera, D. Lara, and C. Dainty, Opt. Express **19**, 26132 (2011).
[39] A. Garcia-Etxarri, ACS Photon. **4**, 1159 (2017).
[40] A. García-Etxarri and J. A. Dionne, Phys. Rev. B **87**, 235409 (2013).
[41] I. Fernandez-Corbaton, X. Zambrana-Puyalto, N. Tischler, X. Vidal, M. L. Juan, and G. Molina-Terriza, Phys. Rev. Lett. **111**, 060401 (2013).
[42] M. K. Schmidt, J. Aizpurua, X. Zambrana-Puyalto, X. Vidal, G. Molina-Terriza, and J. J. Sáenz, Phys. Rev. Lett. **114**, 113902 (2015).
[43] M. Mansuripur, A. R. Zakharian, and E. M. Wright, Phys. Rev. A **84**, 033813 (2011).

Chapter 7

Asymmetry and spin-orbit coupling of light scattered from subwavelength particles

Optics Letters

Asymmetry and spin-orbit coupling of light scattered from subwavelength particles

Jorge Olmos-Trigo,[1] Cristina Sanz-Fernández,[2] F. Sebastián Bergeret,[1,2] and Juan José Sáenz[1,3,*]

[1]Donostia International Physics Center (DIPC), 20018 Donostia-San Sebastián, Spain
[2]Centro de Física de Materiales (CFM-MPC), Centro Mixto CSIC-UPV/EHU, 20018 Donostia-San Sebastián, Spain
[3]IKERBASQUE, Basque Foundation for Science, 48013 Bilbao, Basque Country, Spain
*Corresponding author: juanjo.saenz@dipc.org

Received 17 December 2018; accepted 25 February 2019; posted 4 March 2019 (Doc. ID 355680); published 28 March 2019

Light scattering and spin-orbit angular momentum coupling phenomena from subwavelength objects, with electric and magnetic dipolar responses, are receiving an increasing interest. Under illumination by circularly polarized light, spin-orbit coupling effects have been shown to lead to significant shifts between the measured and actual position of particles. Here we show that the remarkable angular dependence of these "optical mirages" and those of the intensity, degree of circular polarization (DoCP), and spin and orbital angular momentum of scattered photons are all linked, and fully determined, by the dimensionless "asymmetry parameter" g, being independent of the specific optical properties of the scatterer. Interestingly, for $g \neq 0$, the maxima of the optical mirage and angular momentum exchange take place at different scattering angles. We further show that the g parameter is exactly half of the DoCP at a right-angle scattering, which opens the possibility to infer the whole angular properties of the scattered fields by a single far-field polarization measurement.

https://doi.org/10.1364/OL.44.001762

The interference between electric and magnetic dipolar fields scattered from high refractive index (HRI) subwavelength particles is known to lead to strong asymmetric intensity distributions [1], electric-magnetic radiation pressure effects [2], and other interesting phenomena with novel physical effects and applications [3]. In addition to energy and linear momentum, a light wave carries angular momentum (AM) [4] that can be split into spin (SAM) and orbital angular momentum (OAM) [5–7]. Light scattering may couple these two components of the AM, via the spin-orbit interaction (SOI) and modify the contributions of SAM and OAM [8,9]. This phenomena has attracted a great deal of attention in recent years [10–12].

Among all of the intriguing effects originated by the SOI, perhaps the most interesting is the appearance of the optical mirage, i.e., an apparent transversal displacement of a target after scattering [13,14]. This apparent shift, induced by the AM exchange per photon, has been predicted and experimentally proved in very different situations. These include circularly polarized light impinging a dielectric surface [15,16] or a single electric dipolar particle [17,18], where the absolute values of the optical mirage are limited to subwalengths scales. It has been recently demonstrated that this dipolar limit can be surpassed by illumination with elliptically polarized light [15,19,20]. Analogously, enhanced optical mirage values (reaching tens of wavelengths) were obtained for resonant Mie scatters, where higher multipoles are needed [21]. In particular, it has been shown that a high refractive index (HRI) Si-sphere with electric and magnetic dipolar response [22,23], can lead to a diverging optical mirage at backscattering [24–26], when the helicity is preserved [27]. These findings may give ground for the conjecture that any optical property related to the electric and magnetic polarizabilities, such as absorption, particle size, or refractive index, may modify the helicity pattern and hence the optical mirage.

In this Letter, we demonstrate that the degree of circular polarization (DoCP) or, equivalently, the helicity density, Λ_θ [28], depends indeed on the optical properties only through the asymmetry parameter g in the dipolar regime [29]. We demonstrate that from the DoCP measurement in the far field limit (FF), at a single scattering angle, one get full information about other optical parameters, such as g, the re-distribution of AM and the optical mirage. Interestingly, it follows from our study that for non-zero g, the maximum exchange of AM and the maximum optical mirage value do not occur at the same scattering angle. At these two different maxima, the polarization of light is not lineal but elliptical with a z-component of the OAM larger than the total AM, in striking contrast with the pure electric (or magnetic) case $g = 0$ [17,18].

We consider a dielectric sphere of radius a with an arbitrary permittivity ϵ_p and refractive index $m_p^2 = \epsilon_p$, which is embedded in an otherwise homogeneous medium with constant and real relative dielectric permittivity ϵ_h and refractive index $m_h^2 = \epsilon_h$. The geometry of the scattering is sketched in Fig. 1, where a circularly polarized plane wave, with wavenumber k ($k = m_h 2\pi/\lambda_0$, being λ_0 the wavelength in vacuum) and well-defined helicity $\sigma = \pm 1$, is incoming along the z-axis.

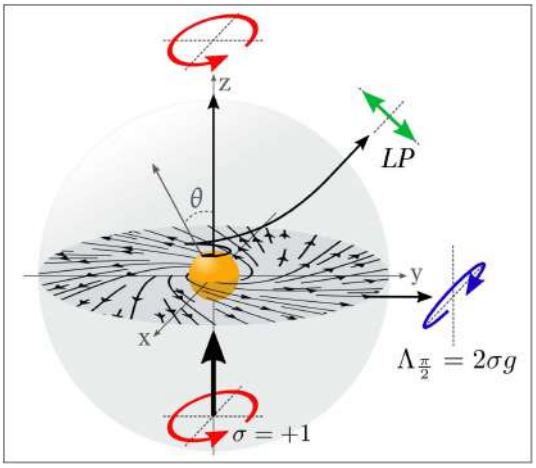

Fig. 1. Sketch of the system: plane wave with well-defined helicity, preserved in forward scattering, $\sigma = 1$, impinging on an example sphere with $g = -0.4$. The scattered light is shown via the conical trajectories of the Poynting vector. At $\theta = \pi/2$, the single measurement of the DoCP gives the value of the scatterer's g-parameter. Red and blue lines illustrate both the counterclockwise and clockwise polarizations, while the linear polarization (LP) is illustrated in green.

The electric field scattered by the nanosphere can be expanded in the helicity basis, allowing us to separate it into two components with well-defined helicity, $\mathbf{E}_{\sigma}^{\text{scat}} = \mathbf{E}_{\sigma+} + \mathbf{E}_{\sigma-}$.

For subwavelength spheres, characterized by their first a_1 and b_1 Mie coefficients [28] or by their electric and magnetic polarizabilities, $\alpha_{\text{E}} = ia_1(6\pi/k^3)$ and $\alpha_M = ib_1(6\pi/k^3)$, the (FF) scattered fields are given by [26]

$$\mathbf{E}_{\sigma\sigma'} \sim \frac{1}{\sqrt{2}} E_{\sigma\sigma'} e^{i\sigma\varphi}(\hat{\mathbf{e}}_\theta + i\sigma'\hat{\mathbf{e}}_\varphi), \tag{1}$$

$$\frac{E_{\sigma\sigma'}}{E_0} = \frac{e^{ikr}}{4\pi kr} k^3 \left(\frac{\sigma\alpha_{\text{E}} + \sigma'\alpha_{\text{M}}}{2}\right)(\sigma\cos\theta + \sigma'), \tag{2}$$

where E_0 is the amplitude of the incident wave. The (FF) radiation pattern, given by the differential scattering cross section, is given by

$$\frac{d\sigma_{\text{scatt}}}{d\Omega} = \frac{k^4(|\alpha_{\text{E}}|^2 + |\alpha_{\text{M}}|^2)}{32\pi^2}(1 + \cos^2\theta + 4g\cos\theta), \tag{3}$$

where

$$g = \langle\cos\theta\rangle = \frac{\text{Re}\{\alpha_{\text{E}}\alpha_{\text{M}}^*\}}{|\alpha_{\text{E}}|^2 + |\alpha_{\text{M}}|^2} \tag{4}$$

is the asymmetry parameter in the dipolar approximation [29]. Notice that $-1/2 < g \leq 1/2$ where the limits correspond to the so-called first ($g = 1/2$) and second ($g = -1/2$) Kerker conditions [30], and $g = -1/2$ is an unreachable value in the absence of gain [31,32].

Applying the definition of the helicity operator [33], $\Lambda \equiv (1/k)\nabla\times$, the helicity density or DoCP can be expressed in terms of the V and I Stokes parameters

$$\text{DoCP} = \Lambda_\theta = \frac{\mathbf{E}_\sigma^{\text{scat}*} \cdot (\Lambda\mathbf{E}_\sigma^{\text{scat}})}{\mathbf{E}_\sigma^{\text{scat}*} \cdot \mathbf{E}_\sigma^{\text{scat}}} = \frac{|\mathbf{E}_{\sigma+}|^2 - |\mathbf{E}_{\sigma-}|^2}{|\mathbf{E}_{\sigma+}|^2 + |\mathbf{E}_{\sigma-}|^2} = \frac{V}{I} \tag{5}$$

$$= \frac{2\sigma((1 + \cos^2\theta)g + \cos\theta)}{1 + \cos^2\theta + 4g\cos\theta}, \tag{6}$$

while the DoCP mean value $\langle\Lambda\rangle$ [17]

$$\langle\Lambda\rangle \equiv \frac{\int\{|\mathbf{E}_{\sigma+}|^2 - |\mathbf{E}_{\sigma-}|^2\}d\Omega}{\int\{|\mathbf{E}_{\sigma+}|^2 + |\mathbf{E}_{\sigma-}|^2\}d\Omega} = 2\sigma g. \tag{7}$$

The angular dependence of the DoCP just depends on the g-parameter. In Fig. 2 we show the DoCP pattern versus both scattering angle θ and g-parameter for an incoming light with helicity $\sigma = +1$. As it can be inferred, the DoCP values are restricted to $-1 < \Lambda \leq 1$, which is maximized when the system is dual, i.e., at the first Kerker condition when helicity is preserved. In addition, we find that the polarization of the scattered light is linear ($\Lambda_{\theta_0} = 0$) when the condition $g = -\cos\theta_0/(1 + \cos^2\theta_0)$ is fulfilled, corresponding to the dashed line in Fig. 2. As it can be seen, it matches with $\theta_0 = \pi/2$ only for $g = 0$, which corresponds with the pure electric (or magnetic) dipolar case. The relatively simple measurement of the polarization degree at a right-angle scattering configuration provides a useful insight on the scattering properties of small particles. In particular, the spectral evolution of the degree of linear polarization was shown to be a simple and accurate way to identify electric and magnetic behaviors of the scattered fields [1,34,35]. Interestingly, we find that the degree of circular polarization, measured at right scattering angles, $\theta = \pi/2$, follows a biunivocal relation with the g-parameter

$$\Lambda_{\frac{\pi}{2}} = \langle\Lambda\rangle = 2\sigma g. \tag{8}$$

This is an important result of this work. This means that by measuring the degree of circular polarization at 90°, we can directly extract the g-parameter.

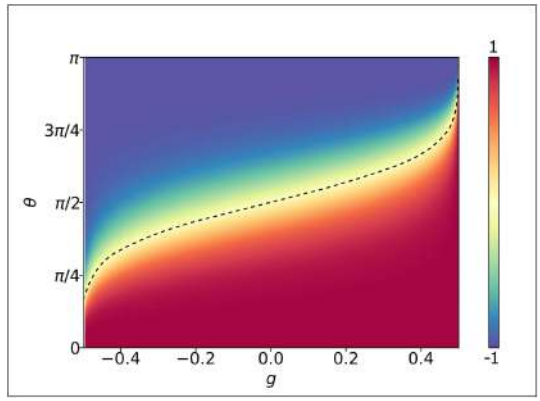

Fig. 2. Color map of the DoCP versus the scattering angle θ and the g-parameter. The white vertical line indicates that this set of DoCP values is forbidden due to causality, i.e., $g > -1/2$. The first Kerker condition, satisfied for $g = 1/2$, gives rise to the conservation of the DoCP, independently of the scattering angle (intense red color). The dashed line illustrates the curve where the scattered light is linearly polarized, $\Lambda = 0$.

Once we have a complete description of the angular dependence of the helicity density in the dipolar regime, it is interesting to analyze its relation with the angular momentum exchanges and the spin-orbit optical mirage. Following Crichton and Marston [7], we notice that the z-component of the SAM per scattered photon, $s_z(\theta)$, is a measurable quantity simply related to the DoCP of the scattered light

$$s_z = \Lambda_\theta \cos\theta, \tag{9}$$

where Λ_θ is given by Eq. (6). Additionally, due to the axial symmetry of the scatterer, the z-component of the total angular momentum of the incoming photons $j_z = \sigma$ is preserved after scattering. Then the z-component of the OAM per scatterd photon, $\ell_z(\theta)$, can also be related to the DoCP

$$\ell_z(\theta) \equiv j_z - s_z(\theta) = \sigma - \Lambda_\theta \cos\theta, \tag{10}$$

which allows us to link the optical mirage's apparent shift [26], Δ, with Λ_θ as

$$\frac{\Delta\pi}{\lambda} = \frac{\ell(\theta)}{\sin\theta} = \frac{\sigma - \Lambda_\theta \cos\theta}{\sin\theta}. \tag{11}$$

Equations (3), (6), (9), (10), and (11) reflect the remarkable result that intensity, degree of circular polarization (DoCP), spin and orbital angular momentum of scattered photons, and the optical mirage ($d\sigma_{\text{scatt}}/d\Omega$, Λ_θ, s_z, ℓ_z and Δ) are all linked, and fully determined, by the dimensionless "asymmetry parameter" g, which is independent of the specific optical properties of the scatterer. This is an important result of the present work: as a direct consequence of Eq. (8), within a single measurement of the DoCP at 90° via polarization filters in the FF, we can extract the g-parameter and infer the angular dependence of all the relevant scattering quantities.

Figure 3 illustrates the angular momentum exchange and the optical mirage dependence with the (FF) observation angle θ for an incoming plane wave with helicity $\sigma = +1$ and total z-component of the total angular momentum per photon $j_z = \sigma$. Figures 3(a) and 3(b) summarize the results for $g = -0.4$ and $g = 0.4$, respectively. In contrast to pure electric (or pure magnetic) dipolar particles with symmetric scattering [$g = 0$, Fig. 3(c)], the maximum angular momentum exchange (corresponding to the minimum of s_z) and the maximum apparent shift of the optical mirage, $\tilde{\Delta} = \Delta/\Delta_{\max}$, take place at

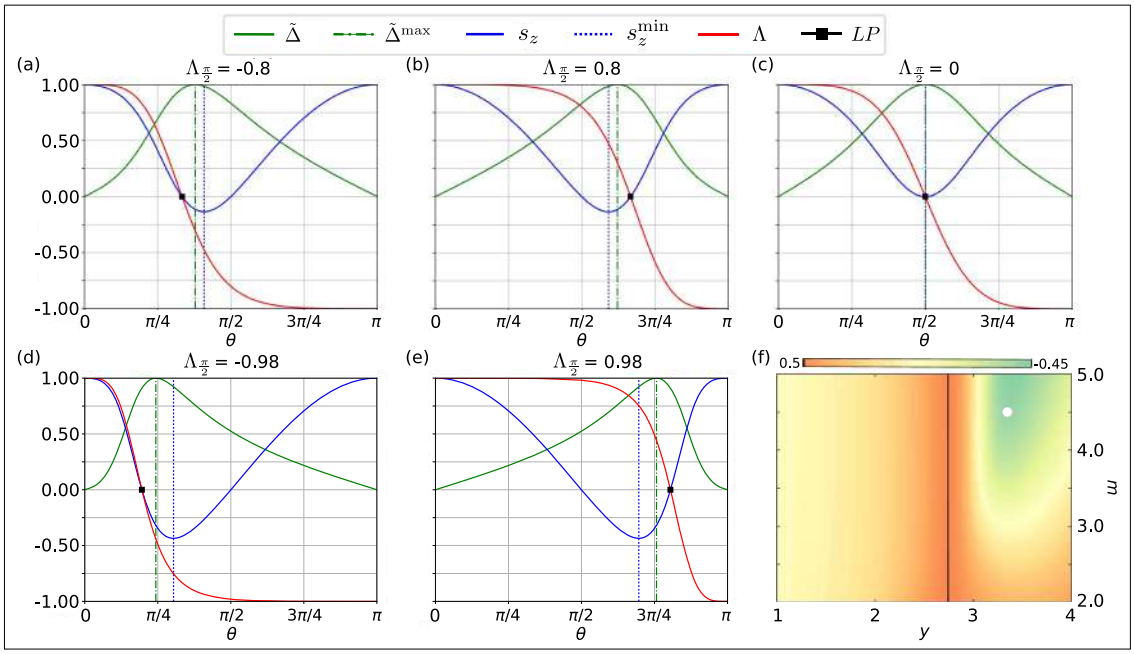

Fig. 3. Normalized optical mirage $\tilde{\Delta} = \Delta/\tilde{\Delta}^{\max}$, spin density ($s_z$), and DoCP ($\Lambda$) versus the scattering angle θ for an incoming circularly polarized plane wave of helicity $\sigma = +1$. The green vertical dashed–dotted lines represent the angles corresponding to the maximum of optical mirage, $\tilde{\Delta}^{\max}$. Blue dotted lines correspond to the angles at which spin-to-orbit angular momentum transfer is maximum (or minimum value of the z-component of SAM per scattered photon, $s_z^{\min}$). The black squares indicate $\Lambda_\theta = 0$, namely, the (FF) observation angles at which light is linearly polarized (LP). (a) and (b) correspond to $\Lambda_{\pi/2} = -0.8$ and $\Lambda_{\pi/2} = +0.8$ (i.e., $g = -0.4$ and $g = +0.4$), respectively. As it can be seen, $g \neq 0$, $\tilde{\Delta}^{\max}$, $s_z^{\min}$, and LP are localized in three different scattering angles in contrast to the $g = 0$ case (c) where they all collapse at right scattering angles $\theta = \pi/2$. (d) and (e) show the different angular dependences as the asymmetry parameter approaches the second ($\Lambda_{\pi/2} = -0.98 \gtrsim -1$) and first ($\Lambda_{\pi/2} = 0.98 \lesssim 1$) Kerker conditions, respectively. (f) Reproduces the asymmetry parameter for isotropic spheres as a function of their refractive index m and size parameter $y = mka$ in the dipolar regime (after Ref. [29]). The black vertical line indicates the first Kerker condition, where $\alpha_E = \alpha_M$. The solid white point highlights $g = -0.4$, which corresponds to both a high refractive index (HRI) dielectric sphere or to a small perfectly conducting sphere [36]. Both subwavelength particles will give rise to exactly the same spin-orbit coupling effects.

different scattering angles but in an angular region in which the z-component of the SAM is negative (i.e., where the photons are not linearly polarized) while the z-component of the OAM is larger than that of the total AM ($\ell_z = j_z - s_z > j_z = 1$). The equivalent effect happens for $\sigma = -1$.

The angular gaps between the minimum of the z-component of the SAM (maximum AM exchange), the maximum of the optical mirage effect, and the angle at which light is linearly polarized first increase when the asymmetry parameter tends to the second or first Kerker conditions, $|g| \approx 0.5$, as it can be seen in Figs. 3(d) and 3(e). However, in the limit of dual scatterers ($g = +0.5$), $s_z \to \cos\theta$, $\Lambda_\theta \to +1$, and the extrema collapse again at the singular backscattering angle $\theta = \pi$. At this condition, there is a divergent optical mirage at backscattering associated to the appearance of an optical vortex with $s_z = -1$ and $\ell_z = 2$ [26]. In contrast, in absence of gain, the Optical Theorem imposes that the limit of $g = -0.5$ is unreachable [31,32], which inhibits the complete (flipping) transformation from $s_z = \sigma$ to $s_z = -\sigma$, although a huge enhancement of the optical mirage is predictably getting close to this condition. Based on the aforementioned, in analogy with dual spheres, we can predict that an anti-dual sphere that could be made with a material with gain [27], with $g = -0.5$, would generate a perfect optical vortex in the forward direction with a divergent apparent displacement.

In conclusion, we have shown that the asymmetry and spin-orbit coupling effects of light scattered from subwavelength spheres with electric and magnetic dipolar responses are fully determined by the dimensionless "asymmetry parameter" g. As a consequence, particles with different optical properties, but which share an identical g parameter value [see Fig. 3(f)], will lead to the same angular dependences of intensity, DoCP, SAM to OAM exchanges and optical mirage apparent shifts. The g-factor can be obtained from a single far-field measurement of the DoCP at 90° and, as a consequence, it is possible to infer all the angular dependences from a single far-field polarization measurement.

We believe that our results open new perspectives in different areas of Optics and Photonics, including science and engineering of antennas, metamaterials, nanophotonics, and optical imaging.

Funding. Ministerio de Economía y Competitividad (MINECO) (FIS2014-55987-P, FIS2015-69295-C3-3-P, FIS2017-82804-P); Eusko Jaurlaritza (PI-2016-1-0041 and PhD Fellowship PRE-2018-2-0252); European Regional Development Fund (ERDF).

REFERENCES

1. J.-M. Geffrin, B. García-Cámara, R. Gómez-Medina, P. Albella, L. S. Froufe-Pérez, C. Eyraud, A. Litman, R. Vaillon, F. González, M. Nieto-Vesperinas, J. J. Sáenz, and F. Moreno, Nat. Commun. **3**, 1171 (2012).
2. M. Nieto-Vesperinas, J. J. Sáenz, R. Gómez-Medina, and L. Chantada, Opt. Express **18**, 11428 (2010).
3. A. I. Kuznetsov, A. E. Miroshnichenko, M. L. Brongersma, Y. S. Kivshar, and B. Luk'yanchuk, Science **354**, aag2472 (2016).
4. L. Allen, S. M. Barnett, and M. J. Padgett, *Optical Angular Momentum* (CRC Press, 2003).
5. H. He, M. Friese, N. Heckenberg, and H. Rubinsztein-Dunlop, Phys. Rev. Lett. **75**, 826 (1995).
6. N. Simpson, K. Dholakia, L. Allen, and M. Padgett, Opt. Lett. **22**, 52 (1997).
7. J. H. Crichton and P. L. Marston, Electron. J. Differential Equations **4**, 37 (2000).
8. G. Moe and W. Happer, J. Phys. B **10**, 1191 (1977).
9. K. Y. Bliokh, E. A. Ostrovskaya, M. A. Alonso, O. G. Rodríguez-Herrera, D. Lara, and C. Dainty, Opt. Express **19**, 26132 (2011).
10. M. Berry, M. Jeffrey, and M. Mansuripur, J. Opt. A **7**, 685 (2005).
11. K. Y. Bliokh, F. Rodríguez-Fortuño, F. Nori, and A. V. Zayats, Nat. Photonics **9**, 796 (2015).
12. K. Y. Bliokh, A. Y. Bekshaev, and F. Nori, Phys. Rev. Lett. **119**, 073901 (2017).
13. M. Onoda, S. Murakami, and N. Nagaosa, Phys. Rev. Lett. **93**, 083901 (2004).
14. K. Y. Bliokh and Y. P. Bliokh, Phys. Rev. Lett. **96**, 073903 (2006).
15. O. Hosten and P. Kwiat, Science **319**, 787 (2008).
16. M. Berry, Proc. R. Soc. London Ser. A **467**, 2500 (2011).
17. C. Schwartz and A. Dogariu, Opt. Express **14**, 8425 (2006).
18. H. F. Arnoldus, X. Li, and J. Shu, Opt. Lett. **33**, 1446 (2008).
19. Y. Gorodetski, K. Bliokh, B. Stein, C. Genet, N. Shitrit, V. Kleiner, E. Hasman, and T. Ebbesen, Phys. Rev. Lett. **109**, 013901 (2012).
20. G. Araneda, S. Walser, Y. Colombe, D. Higginbottom, J. Volz, R. Blatt, and A. Rauschenbeutel, Nat. Phys. **15**, 17 (2019).
21. D. Haefner, S. Sukhov, and A. Dogariu, Phys. Rev. Lett. **102**, 123903 (2009).
22. A. B. Evlyukhin, C. Reinhardt, A. Seidel, B. S. Luk'yanchuk, and B. N. Chichkov, Phys. Rev. B **82**, 045404 (2010).
23. A. García-Etxarri, R. Gómez-Medina, L. S. Froufe-Pérez, C. López, L. Chantada, F. Scheffold, J. Aizpurua, M. Nieto-Vesperinas, and J. J. Sáenz, Opt. Express **19**, 4815 (2011).
24. J. Olmos-Trigo, C. Sanz-Fernández, F. S. Bergeret, and J. J. Sáenz, in *Nanolight*, Benasque, Spain, March11–16, 2018.
25. D. Gao, R. Shi, A. E. Miroshnichenko, and L. Gao, Laser Photon. Rev. **12**, 1800130 (2018).
26. J. Olmos-Trigo, C. Sanz-Fernández, A. García-Etxarri, G. Molina-Terriza, F. S. Bergeret, and J. J. Sáenz, Phys. Rev. A **99**, 013852 (2019).
27. X. Zambrana-Puyalto, I. Fernandez-Corbaton, M. Juan, X. Vidal, and G. Molina-Terriza, Opt. Lett. **38**, 1857 (2013).
28. C. F. Bohren and D. R. Huffman, *Absorption and Scattering of Light by Small Particles* (Wiley, 2008).
29. R. Gómez-Medina, L. Froufe-Pérez, M. Yépez, F. Scheffold, M. Nieto-Vesperinas, and J. J. Sáenz, Phys. Rev. A **85**, 035802 (2012).
30. M. Kerker, D.-S. Wang, and C. Giles, J. Opt. Soc. Am. A **73**, 765 (1983).
31. A. Alù and N. Engheta, J. Nanophoton. **4**, 041590 (2010).
32. R. Gomez-Medina, B. Garcia-Camara, I. Suárez-Lacalle, F. González, F. Moreno, M. Nieto-Vesperinas, and J. J. Sáenz, J. Nanophoton. **5**, 053512 (2011).
33. I. Fernandez-Corbaton, X. Zambrana-Puyalto, and G. Molina-Terriza, Phys. Rev. A **86**, 042103 (2012).
34. B. Setién, P. Albella, J. Saiz, F. González, and F. Moreno, New J. Phys. **12**, 103031 (2010).
35. B. García-Cámara, F. González, and F. Moreno, Opt. Lett. **35**, 4084 (2010).
36. J. D. Jackson, *Classical Electrodynamics* (Wiley, 1999).

References

[1] Adagideli, İ. and Bauer, G. E. W. (2005). Intrinsic spin hall edges. Phys. Rev. Lett., 95:256602.

[2] Albaladejo, S., Gómez-Medina, R., Froufe-Pérez, L. S., Marinchio, H., Carminati, R., Torrado, J. F., Armelles, G., García-Martín, A., and Sáenz, J. J. (2010). Radiative corrections to the polarizability tensor of an electrically small anisotropic dielectric particle. Opt. Express, 18(4):3556–3567.

[3] Allen, L., Beijersbergen, M. W., Spreeuw, R. J. C., and Woerdman, J. P. (1992). Orbital angular momentum of light and the transformation of laguerre-gaussian laser modes. Phys. Rev. A, 45:8185–8189.

[4] Allen, L., Padgett, M., and Babiker, M. (1999). IV The orbital angular momentum of light. Prog. Opt., 39:291 – 372.

[5] Amin, V. P. and Stiles, M. D. (2016a). Spin transport at interfaces with spin-orbit coupling: Formalism. Phys. Rev. B, 94:104419.

[6] Amin, V. P. and Stiles, M. D. (2016b). Spin transport at interfaces with spin-orbit coupling: Phenomenology. Phys. Rev. B, 94:104420.

[7] Amin, V. P., Zemen, J., and Stiles, M. D. (2018). Interface-generated spin currents. Phys. Rev. Lett., 121:136805.

[8] Araneda, G., Walser, S., Colombe, Y., Higginbottom, D. B., Volz, J., Blatt, R., and Rauschenbeutel, A. (2019). Wavelength-scale errors in optical localization due to spin–orbit coupling of light. Nat. Phys., 15(1):17–21.

[9] Arnoldus, H. F. and Foley, J. T. (2004). The dipole vortex. Opt. Commun., 231(1):115 – 128.

[10] Arnoldus, H. F., Li, X., and Shu, J. (2008). Subwavelength displacement of the far-field image of a radiating dipole. Opt. Lett., 33(13):1446–1448.

[11] Aronov, A. G., Lyanda-Geller, Y. B., and Pikus, G. E. (1991). Spin polarization of electrons by an electric current. Sov. Phys. JETP, 73:537–541.

[12] Ashcroft, N. W., Mermin, N. D., et al. (1976). Sol. Stat. Phys. New York: Holt, Rinehart and Winston,.

[13] Avsar, A., Ochoa, H., Guinea, F., Özyilmaz, B., van Wees, B. J., and Vera-Marun, I. J. (2020). Colloquium: Spintronics in graphene and other two-dimensional materials. Rev. Mod. Phys., 92:021003.

[14] Barone, A. and Paterno, G. (1982). Physics and Applications of the Josephson Effect. John Wiley and Sons, Ltd.

[15] Barreda, A. I., Saiz, J. M., González, F., Moreno, F., and Albella, P. (2019). Recent advances in high refractive index dielectric nanoantennas: Basics and applications. AIP Advances, 9(4):040701.

[16] Barreda, Á. I., Saleh, H., Litman, A., González, F., Geffrin, J.-M., and Moreno, F. (2018). On the scattering directionality of a dielectric particle dimer of high refractive index. Scient. Rep., 8(1):1–12.

[17] Bel'kov, V. and Ganichev, S. (2008). Magneto-gyrotropic effects in semiconductor quantum wells. Semicond. Sci. Technol., 23(11):114003.

[18] Benítez, L. A., Torres, W. S., Sierra, J. F., Timmermans, M., Garcia, J. H., Roche, S., Costache, M. V., and Valenzuela, S. O. (2020). Tunable room-temperature spin galvanic and spin hall effects in van der waals heterostructures. Nat. Mater., 19(2):170–175.

[19] Berger, L. (1970). Side-jump mechanism for the hall effect of ferromagnets. Phys. Rev. B, 2:4559–4566.

[20] Bergeret, F. S. and Tokatly, I. V. (2014). Spin-orbit coupling as a source of long-range triplet proximity effect in superconductor-ferromagnet hybrid structures. Phys. Rev. B, 89:134517.

[21] Bergeret, F. S. and Tokatly, I. V. (2015). Theory of diffusive φ_0 josephson junctions in the presence of spin-orbit coupling. EPL, 110(5):57005.

[22] Beth, R. A. (1936). Mechanical detection and measurement of the angular momentum of light. Phys. Rev., 50:115–125.

[23] Bialynicki-Birula, I. and Bialynicka-Birula, Z. (2016). Gravitational waves carrying orbital angular momentum. New J. Phys., 18(2):023022.

[24] Bir, G., Aronov, A., and Pikus, G. (1976). Spin relaxation of electrons due to scattering by holes. JETP, 42:705.

[25] Bliokh, K. Y., Alonso, M. A., Ostrovskaya, E. A., and Aiello, A. (2010). Angular momenta and spin-orbit interaction of nonparaxial light in free space. Phys. Rev. A, 82:063825.

[26] Bliokh, K. Y., Ostrovskaya, E. A., Alonso, M. A., Rodríguez-Herrera, O. G., Lara, D., and Dainty, C. (2011). Spin-to-orbital angular momentum conversion in focusing, scattering, and imaging systems. Opt. Express, 19(27):26132–26149.

[27] Bliokh, K. Y., Rodríguez-Fortuño, F. J., Nori, F., and Zayats, A. V. (2015). Spin–orbit interactions of light. Nat. Photonics, 9(12):796–808.

[28] Bohren, C. F. and Huffman, D. R. (2008). Absorption and scattering of light by small particles. John Wiley & Sons.

[29] Bonod, N. and Kivshar, Y. (2020). All-dielectric mie-resonant metaphotonics. Comp. Rendus. Phys.

[30] Borge, J. and Tokatly, I. V. (2019). Boundary conditions for spin and charge diffusion in the presence of interfacial spin-orbit coupling. Phys. Rev. B, 99(24):241401.

[31] Born, M. and Wolf, E. (2013). Principles of optics: electromagnetic theory of propagation, interference and diffraction of light. Elsevier.

[32] Boross, P., Dóra, B., Kiss, A., and Simon, F. (2013). A unified theory of spin-relaxation due to spin-orbit coupling in metals and semiconductors. Scient. Rep., 3(1):1–5.

[33] Brataas, A., Mal'shukov, A. G., and Tserkovnyak, Y. (2007). Spin injection in quantum wells with spatially dependent rashba interaction. New J. Phys., 9(9):345–345.

[34] Bychkov, Y. A. and Rashba, É. I. (1984). Properties of a 2d electron gas with lifted spectral degeneracy. JETP lett, 39(2):78.

[35] Cai, W. and Shalaev, V. M. (2010). Opt. Metamat., volume 10. Springer.

[36] Calkin, M. G. (1965). An invariance property of the free electromagnetic field. Am. J. Phys., 33(11):958–960.

[37] Chappert, C., Fert, A., and Nguyen, F. (2010). The emergence of spin electronics in data storage, pages 147–157.

[38] Crichton, J. H. and Marston, P. L. (2000). The measurable distinction between the spin and orbital angular momenta of electromagnetic radiation. Elect. J. Diff. Eqs., 4:37–50.

[39] Darwin, C. G. (1932). Notes on the theory of radiation. Proceedings of the Royal Society of London. Series A, Containing Papers of a Mathematical and Physical Character, 136(829):36–52.

[40] Datta, S. and Das, B. (1990). Electronic analog of the electro-optic modulator. Appl. Phys. Lett., 56(7):665–667.

[41] Debye, P. (1909). Der lichtdruck auf kugeln von beliebigem material. Ann. Phys., 335(11):57–136.

[42] Dieny, B., Prejbeanu, I. L., Garello, K., Gambardella, P., Freitas, P., Lehndorff, R., Raberg, W., Ebels, U., Demokritov, S. O., Akerman, J., et al. (2020). Opportunities and challenges for spintronics in the microelectronics industry. Nat. Electron., 3(8):446–459.

[43] Doyle, W. T. (1989). Optical properties of a suspension of metal spheres. Phys. Rev. B, 39:9852–9858.

[44] Dresselhaus, G. (1955). Spin-orbit coupling effects in zinc blende structures. Phys. Rev., 100:580–586.

[45] Drude, P. (1900a). Zur elektronentheorie der metalle. Ann. Phys., 306(3):566–613.

[46] Drude, P. (1900b). Zur elektronentheorie der metalle; ii. teil. galvanomagnetische und thermomagnetische effecte. Ann. Phys., 308(11):369–402.

[47] D'yakonov, M. and Khaetskii, A. (1984). Relaxation of nonequilibrium carrier-density matrix in semiconductors with degenerate bands. Zh. Eksp. Teor. Fiz, 86:1843–1856.

[48] Dyakonov, M. and Perel, V. (1971). Current-induced spin orientation of electrons in semiconductors. Phys. Lett. A, 35(6):459 – 460.

[49] D'yakonov, M. I. and Kachorovskii, V. Y. (1986). Spin relaxation of two-dimensional electrons in non-centrosymmetric semiconductors. Sov. Phys. Semicond., 20(1):110–112.

[50] Dyakonov, M. I. and Khaetskii, A. V. (2017). Spin physics in semiconductors, volume 157. Springer.

[51] D'Yakonov, M. I. and Perel', V. I. (1971). Spin Orientation of Electrons Associated with the Interband Absorption of Light in Semiconductors. Sov. J. Exp. Theor. Phys., 33:1053.

[52] D'Yakonov, M. I. and Perel', V. I. (1972). Spin relaxation of conduction electrons in noncentrosymmetric semiconductors. Sov. Phys. Sol. Stat., 13:3023.

[53] Edelstein, V. M. (1990). Spin polarization of conduction electrons induced by electric current in two-dimensional asymmetric electron systems. Sol. Stat. Commun., 73(3):233 – 235.

[54] Edmonds, A. R. (1996). Angular momentum in quantum mechanics. Princeton University Press.

[55] Elliott, R. J. (1954). Theory of the effect of spin-orbit coupling on magnetic resonance in some semiconductors. Phys. Rev., 96:266–279.

[56] Fabian, J., Matos-Abiague, A., Ertler, C., Stano, P., and Zutic, I. (2007). Semiconductor spintronics. arXiv preprint arXiv:0711.1461.

[57] Fernandez-Corbaton, I., Zambrana-Puyalto, X., and Molina-Terriza, G. (2012). Helicity and angular momentum: A symmetry-based framework for the study of light-matter interactions. Phys. Rev. A, 86:042103.

[58] Fernandez-Corbaton, I., Zambrana-Puyalto, X., Tischler, N., Vidal, X., Juan, M. L., and Molina-Terriza, G. (2013). Electromagnetic duality symmetry and helicity conservation for the macroscopic maxwell's equations. Phys. Rev. Lett., 111:060401.

[59] Fu, Q. and Sun, W. (2001). Mie theory for light scattering by a spherical particle in an absorbing medium. Appl. Opt., 40(9):1354–1361.

[60] Ganichev, S., Ivchenko, E., Bel'Kov, V., Tarasenko, S., Sollinger, M., Weiss, D., Wegscheider, W., and Prettl, W. (2002). Spin-galvanic effect. Nature, 417(6885):153–156.

[61] García-Etxarri, A., Gómez-Medina, R., Froufe-Pérez, L. S., López, C., Chantada, L., Scheffold, F., Aizpurua, J., Nieto-Vesperinas, M., and Sáenz, J. J. (2011). Strong magnetic response of submicron silicon particles in the infrared. Opt. Express, 19(6):4815–4826.

[62] Ghiasi, T. S., Kaverzin, A. A., Blah, P. J., and van Wees, B. J. (2019). Charge-to-spin conversion by the rashba–edelstein effect in two-dimensional van der waals heterostructures up to room temperature. Nano Letters, 19(9):5959–5966. PMID: 31408607.

[63] Gibson, G., Courtial, J., Padgett, M. J., Vasnetsov, M., Pas'ko, V., Barnett, S. M., and Franke-Arnold, S. (2004). Free-space information transfer using light beams carrying orbital angular momentum. Opt. Express, 12(22):5448–5456.

[64] Golub, L. and Ivchenko, E. (2011). Spin orientation by electric current in (110) quantum wells. Phys. Rev. B, 84(11):115303.

[65] Gomez-Medina, R., Garcia-Camara, B., Suarez-Lacalle, I., González, F., Moreno, F., Nieto-Vesperinas, M., and Saenz, J. J. (2011). Electric and magnetic dipolar response of germanium nanospheres: interference effects, scattering anisotropy, and optical forces. J. Nanophoton., 5(1):1 – 10.

[66] Gorini, C., Eckern, U., and Raimondi, R. (2015). Spin hall effects due to phonon skew scattering. Phys. Rev. Lett., 115(7):076602.

[67] Gorini, C., Schwab, P., Raimondi, R., and Shelankov, A. L. (2010). Non-abelian gauge fields in the gradient expansion: Generalized boltzmann and eilenberger equations. Phys. Rev. B, 82:195316.

[68] Gorini, C., Sheikhabadi, A. M., Shen, K., Tokatly, I. V., Vignale, G., and Raimondi, R. (2017). Theory of current-induced spin polarization in an electron gas. Phys. Rev. B, 95(20):205424.

[69] Guarcello, C., Citro, R., Durante, O., Bergeret, F. S., Iorio, A., Sanz-Fernández, C., Strambini, E., Giazotto, F., and Braggio, A. (2020). rf-squid measurements of anomalous josephson effect. Phys. Rev. Research, 2:023165.

[70] Haefner, D., Sukhov, S., and Dogariu, A. (2009). Spin hall effect of light in spherical geometry. Phys. Rev. Lett., 102:123903.

[71] Hall, E. H. et al. (1879). On a new action of the magnet on electric currents. Am. J. Mathemat., 2(3):287–292.

[72] He, H., Friese, M. E. J., Heckenberg, N. R., and Rubinsztein-Dunlop, H. (1995). Direct observation of transfer of angular momentum to absorptive particles from a laser beam with a phase singularity. Phys. Rev. Lett., 75:826–829.

[73] Hirsch, J. E. (1999). Spin hall effect. Phys. Rev. Lett., 83(9):1834.

[74] Hoque, A. M., Khokhriakov, D., Karpiak, B., and Dash, S. P. (2019). All-electrical creation and control of giant spin-galvanic effect in 1t-mote2/graphene heterostructures at room temperature. arXiv preprint arXiv:1908.09367.

[75] Huang, C., Tokatly, I. V., and Bergeret, F. S. (2018). Extrinsic spin-charge coupling in diffusive superconducting systems. Phys. Rev. B, 98(14):144515.

[76] Hulst, H. C. and van de Hulst, H. C. (1981). Light scattering by small particles. Courier Corporation.

[77] Humblet, J. (1943). Sur le moment d'impulsion d'une onde electromagnetique. Physica, 10(7):585–603.

[78] Inoue, J.-i., Bauer, G. E. W., and Molenkamp, L. W. (2004). Suppression of the persistent spin hall current by defect scattering. Phys. Rev. B, 70(4):041303.

[79] Isasa, M., Martínez-Velarte, M. C., Villamor, E., Magén, C., Morellón, L., De Teresa, J. M., Ibarra, M. R., Vignale, G., Chulkov, E. V., Krasovskii, E. E., et al. (2016). Origin of inverse rashba-edelstein effect detected at the cu/bi interface using lateral spin valves. Phys. Rev. B, 93(1):014420.

[80] Isshiki, H., Muduli, P., Kim, J., Kondou, K., and Otani, Y. (2020). Phenomenological model for the direct and inverse edelstein effects. Phys. Rev. B, 102:184411.

[81] Jackson, J. D. (1999). Classical electrodynamics, 3rd ed. Am. J. Phys., 67(9):841–842.

[82] Jedema, F., Heersche, H., Filip, A., Baselmans, J., and Van Wees, B. (2002). Electrical detection of spin precession in a metallic mesoscopic spin valve. Nature, 416(6882):713–716.

[83] Jedema, F. J., Filip, A., and Van Wees, B. (2001). Electrical spin injection and accumulation at room temperature in an all-metal mesoscopic spin valve. Nature, 410(6826):345–348.

[84] Josephson, B. (1962). Possible new effects in superconductive tunnelling. Physics Letters, 1(7):251 – 253.

[85] Karube, S., Kondou, K., and Otani, Y. (2016). Experimental observation of spin-to-charge current conversion at non-magnetic metal/bi2o3interfaces. App. Phys. Express, 9(3):033001.

[86] Kato, Y. K., Myers, R. C., Gossard, A. C., and Awschalom, D. D. (2004). Science, 306:1910.

[87] Kerker, M. (1969). The scattering of light and other electromagnetic radiation, academic. New York.

[88] Kerker, M., Wang, D.-S., and Giles, C. L. (1983). Electromagnetic scattering by magnetic spheres. J. Opt. Soc. Am., 73(6):765–767.

[89] Khokhriakov, D., Hoque, A. M., Karpiak, B., and Dash, S. P. (2020). Gate-tunable spin-galvanic effect in graphene-topological insulator van der waals heterostructures at room temperature. Nat. Commun., 11(1):1–7.

[90] Kim, J., Chen, Y.-T., Karube, S., Takahashi, S., Kondou, K., Tatara, G., and Otani, Y. (2017). Evaluation of bulk-interface contributions to edelstein magnetoresistance at metal/oxide interfaces. Phys. Rev. B, 96:140409.

[91] Kimura, T., Hamrle, J., and Otani, Y. (2005). Estimation of spin-diffusion length from the magnitude of spin-current absorption: Multiterminal ferromagnetic/nonferromagnetic hybrid structures. Phys. Rev. B, 72:014461.

[92] Kimura, T., Otani, Y., Sato, T., Takahashi, S., and Maekawa, S. (2007). Room-temperature reversible spin hall effect. Phys. Rev. Lett., 98:156601.

[93] Kondou, K., Yoshimi, R., Tsukazaki, A., Fukuma, Y., Matsuno, J., Takahashi, K., Kawasaki, M., Tokura, Y., and Otani, Y. (2016). Fermi-level-dependent charge-to-spin current conversion by dirac surface states of topological insulators. Nat. Phys., 12(11):1027–1031.

[94] Konschelle, F., Tokatly, I. V., and Bergeret, F. S. (2015). Theory of the spin-galvanic effect and the anomalous phase shift φ 0 in superconductors and josephson junctions with intrinsic spin-orbit coupling. Phys. Rev. B, 92(12):125443.

[95] Kuznetsov, A. I. et al. (2016). Optically resonant dielectric nanostructures. Science, 354(6314):aag2472.

[96] Landau, L. D. and Lifshitz, E. M. (2013). Quantum mechanics: non-relativistic theory, volume 3. Elsevier.

[97] Lesne, E., Fu, Y., Oyarzun, S., Rojas-Sánchez, J., Vaz, D., Naganuma, H., Sicoli, G., Attané, J.-P., Jamet, M., Jacquet, E., et al. (2016). Highly efficient and tunable spin-to-charge conversion through rashba coupling at oxide interfaces. Nat. Mater., 15(12):1261–1266.

[98] Li, L., Zhang, J., Myeong, G., Shin, W., Lim, H., Kim, B., Kim, S., Jin, T., Cavill, S., Kim, B. S., Kim, C., Lischner, J., Ferreira, A., and Cho, S. (2020). Gate-tunable reversible rashba–edelstein effect in a few-layer graphene/2h-tas2 heterostructure at room temperature. ACS Nano, 14(5):5251–5259. PMID: 32267673.

[99] Liu, L., Pai, C.-F., Li, Y., Tseng, H., Ralph, D., and Buhrman, R. (2012). Spin-torque switching with the giant spin hall effect of tantalum. Science, 336(6081):555–558.

[100] Logan, N. A. (1962). Early history of the mie solution. J. Opt. Soc. Am., 52(3):342–343.

[101] Lorenz, L. (1890). Lysbevægelsen i og uden for en af plane Lysbølger belyst Kugle. na.

[102] Luengo-Kovac, M., Huang, S., Del Gaudio, D., Occena, J., Goldman, R. S., Raimondi, R., and Sih, V. (2017). Current-induced spin polarization in ingaas and gaas epilayers with varying doping densities. Phys. Rev. B, 96(19):195206.

[103] Lyanda-Geller, Y. and Aronov, A. (1989). JETP Lett., 50:431.

[104] MacDonald, M. P., Paterson, L., Volke-Sepulveda, K., Arlt, J., Sibbett, W., and Dholakia, K. (2002). Creation and manipulation of three-dimensional optically trapped structures. Science, 296(5570):1101–1103.

[105] Manchon, A., Koo, H. C., Nitta, J., Frolov, S., and Duine, R. (2015). New perspectives for rashba spin–orbit coupling. Nat. Mater., 14(9):871–882.

[106] Manipatruni, S., Nikonov, D. E., Lin, C.-C., Gosavi, T. A., Liu, H., Prasad, B., Huang, Y.-L., Bonturim, E., Ramesh, R., and Young, I. A. (2019). Scalable energy-efficient magnetoelectric spin–orbit logic. Nature, 565(7737):35–42.

[107] Manipatruni, S., Nikonov, D. E., and Young, I. A. (2018). Beyond cmos computing with spin and polarization. Nat. Phys., 14(4):338–343.

[108] Mansuripur, M. (2011). Spin and orbital angular momenta of electromagnetic waves in free space. Phys. Rev. A, 84:033838.

[109] Maxwell, J. C. (1873). A treatise on electricity and magnetism, volume 1. Oxford: Clarendon Press.

[110] Mie, G. (1908). Beiträge zur optik trüber medien, speziell kolloidaler metallösungen. Ann. Phys., 330(3):377–445.

[111] Miron, I. M., Garello, K., Gaudin, G., Zermatten, P.-J., Costache, M. V., Auffret, S., Bandiera, S., Rodmacq, B., Schuhl, A., and Gambardella, P. (2011). Perpendicular switching of a single ferromagnetic layer induced by in-plane current injection. Nature, 476(7359):189–193.

[112] Mishchenko, E. G., Shytov, A. V., and Halperin, B. I. (2004). Spin current and polarization in impure two-dimensional electron systems with spin-orbit coupling. Phys. Rev. Lett., 93(22):226602.

[113] Nakayama, H., Kanno, Y., An, H., Tashiro, T., Haku, S., Nomura, A., and Ando, K. (2016). Rashba-edelstein magnetoresistance in metallic heterostructures. Phys. Rev. Lett., 117:116602.

[114] Nanz, S. (2016). Toroidal Multipole Moments in Classical Electrodynamics: An Analysis of Their Emergence and Physical Significance. Springer.

[115] Nieto-Vesperinas, M., Gomez-Medina, R., and Saenz, J. J. (2011). Angle-suppressed scattering and optical forces on submicrometer dielectric particles. J. Opt. Soc. Am. A, 28(1):54–60.

[116] Niimi, Y. and Otani, Y. (2015). Reciprocal spin hall effects in conductors with strong spin–orbit coupling: a review. Rep. Prog. Phys., 78(12):124501.

[117] Novotny, L. and Hecht, B. (2012). Principles of nano-optics. Cambridge university press.

[118] Olmos-Trigo, J., Abujetas, D. R., Sanz-Fernández, C., Sánchez-Gil, J. A., and Sáenz, J. J. (2020a). Optimal backward light scattering by dipolar particles. Phys. Rev. Research, 2:013225.

[119] Olmos-Trigo, J., Abujetas, D. R., Sanz-Fernández, C., Zambrana-Puyalto, X., de Sousa, N., Sánchez-Gil, J. A., and Sáenz, J. J. (2020b). Unveiling dipolar spectral regimes of large dielectric mie spheres from helicity conservation. Phys. Rev. Research, 2:043021.

[120] Olmos-Trigo, J., Sanz-Fernández, C., Abujetas, D. R., Lasa-Alonso, J., de Sousa, N., García-Etxarri, A., Sánchez-Gil, J. A., Molina-Terriza, G., and Sáenz, J. J. (2020c). Kerker conditions upon lossless, absorption, and optical gain regimes. Phys. Rev. Lett., 125:073205.

[121] Olmos-Trigo, J., Sanz-Fernández, C., Abujetas, D. R., García-Etxarri, A., Molina-Terriza, G., Sánchez-Gil, J. A., Bergeret, F. S., and Sáenz, J. J. (2019). Role of the absorption on the spin-orbit interactions of light with si nano-particles. J. Appl. Phys., 126(3):033104.

[122] Ol'ga, V. D. (2005). Spin-hall conductivity in a two-dimensional rashba electron gas. Phys. Rev. B, 71(24):245327.

[123] Onoda, M., Murakami, S., and Nagaosa, N. (2004). Hall effect of light. Phys. Rev. Lett., 93:083901.

[124] Padgett, M. and Bowman, R. (2011). Tweezers with a twist. Nat. Photonics, 5(6):343–348.

[125] Parker, J., Peterson, C. W., Yifat, Y., Rice, S. A., Yan, Z., Gray, S. K., and Scherer, N. F. (2020). Optical matter machines: angular momentum conversion by collective modes in optically bound nanoparticle arrays. Optica, 7(10):1341–1348.

[126] Pauli, W. (1927). Zur quantenmechanik des magnetischen elektrons. Zeitschrift für Physik, 43(9-10):601–623.

[127] Pham, V. T., Groen, I., Manipatruni, S., Choi, W. Y., Nikonov, D. E., Sagasta, E., Lin, C.-C., Gosavi, T. A., Marty, A., Hueso, L. E., Young, I. A., and Casanova, F. (2020). Spin–orbit magnetic state readout in scaled ferromagnetic/heavy metal nanostructures. Nat. Electron., 3(6):309–315.

[128] Poynting, J. H. (1909). The wave motion of a revolving shaft, and a suggestion as to the angular momentum in a beam of circularly polarised light. Proc. Royal Soc. London, 82(557):560–567.

[129] Raimondi, R., Gorini, C., Schwab, P., and Dzierzawa, M. (2006). Quasiclassical approach to the spin hall effect in the two-dimensional electron gas. Phys. Rev. B, 74(3):035340.

[130] Raimondi, R. and Schwab, P. (2005). Spin-hall effect in a disordered two-dimensional electron system. Phys. Rev. B, 71(3):033311.

[131] Raimondi, R. and Schwab, P. (2010). Interplay of intrinsic and extrinsic mechanisms to the spin hall effect in a two-dimensional electron gas. Physica E, 42(4):952 – 955. 18th International Conference on Electron Properties of Two-Dimensional Systems.

[132] Raimondi, R., Schwab, P., Gorini, C., and Vignale, G. (2012). Spin-orbit interaction in a two-dimensional electron gas: A su(2) formulation. Ann. Phys., 524(3-4).

[133] Rojas-Sánchez, J.-C., Oyarzún, S., Fu, Y., Marty, A., Vergnaud, C., Gambarelli, S., Vila, L., Jamet, M., Ohtsubo, Y., Taleb-Ibrahimi, A., Le Fèvre, P., Bertran, F., Reyren, N., George, J.-M., and Fert, A. (2016). Spin to charge conversion at room temperature by spin pumping into a new type of topological insulator: α-sn films. Phys. Rev. Lett., 116:096602.

[134] Safeer, C., Ingla-Aynés, J., Herling, F., Garcia, J. H., Vila, M., Ontoso, N., Calvo, M. R., Roche, S., Hueso, L. E., and Casanova, F. (2019). Room-temperature spin hall effect in graphene/mos2 van der waals heterostructures. Nano letters, 19(2):1074–1082.

[135] Safeer, C., Jué, E., Lopez, A., Buda-Prejbeanu, L., Auffret, S., Pizzini, S., Boulle, O., Miron, I. M., and Gaudin, G. (2016). Spin–orbit torque magnetization switching controlled by geometry. Nat. Nanotech., 11(2):143.

[136] Safeer, C. K., Ingla-Aynés, J., Ontoso, N., Herling, F., Yan, W., Hueso, L. E., and Casanova, F. (2020). Spin hall effect in bilayer graphene combined with an insulator up to room temperature. Nano Letters, 20(6):4573–4579. PMID: 32406693.

[137] Sagasta, E., Omori, Y., Isasa, M., Gradhand, M., Hueso, L. E., Niimi, Y., Otani, Y., and Casanova, F. (2016). Phys. Rev. B, 94:060412.

[138] Sánchez, J. C. R., Vila, L., Desfonds, G., Gambarelli, S., Attané, J. P., De Teresa, J. M., Magén, C., and Fert, A. (2013). Spin-to-charge conversion using rashba coupling at the interface between non-magnetic materials. Nat. Commun., 4:2944.

[139] Schmiegelow, C. T., Schulz, J., Kaufmann, H., Ruster, T., Poschinger, U. G., and Schmidt-Kaler, F. (2016). Transfer of optical orbital angular momentum to a bound electron. Nat. Commun., 7:12998.

[140] Seki, T., Hasegawa, Y., Mitani, S., Takahashi, S., Imamura, H., Maekawa, S., Nitta, J., and Takanashi, K. (2008). Giant spin hall effect in perpendicularly spin-polarized fept/au devices. Nat Mater, 7:125.

[141] Shen, K., Vignale, G., and Raimondi, R. (2014). Microscopic theory of the inverse edelstein effect. Phys. Rev. Lett., 112:096601.

[142] Shibanuma, T., Albella, P., and Maier, S. A. (2016). Unidirectional light scattering with high efficiency at optical frequencies based on low-loss dielectric nanoantennas. Nanoscale, 8:14184–14192.

[143] Sih, V., Myers, R. C., Kato, Y. K., Lau, W. H., Gossard, A. C., and Awschalom, D. D. (2005). Nat. Phys., 1:31.

[144] Simpson, N. B., Dholakia, K., Allen, L., and Padgett, M. J. (1997). Mechanical equivalence of spin and orbital angular momentum of light: an optical spanner. Opt. Lett., 22(1):52–54.

[145] Sinova, J., Valenzuela, S. O., Wunderlich, J., Back, C. H., and Jungwirth, T. (2015). Spin hall effects. Rev. Mod. Phys., 87(4):1213.

[146] Smit, J. (1958). The spontaneous hall effect in ferromagnetics ii. Physica, 24(1):39 – 51.

[147] Sommerfeld, A. (1928). Zur elektronentheorie der metalle auf grund der fermischen statistik. Zeitschrift für Physik, 47(1-2):1–32.

[148] Soumyanarayanan, A., Reyren, N., Fert, A., and Panagopoulos, C. (2016). Emergent phenomena induced by spin–orbit coupling at surfaces and interfaces. Nature, 539(7630):509–517.

[149] Stern, N. P., Ghosh, S., Xiang, G., Zhu, M., Samarth, N., and Awschalom, D. D. (2006). Current-induced polarization and the spin hall effect at room temperature. Phys. Rev. Lett., 97:126603.

[150] Stokes, G. G. (2009). On the Composition and Resolution of Streams of Polarized Light from different Sources, volume 3 of Cambridge Library Collection - Mathematics, page 233–258. Cambridge University Press.

[151] Strambini, E., Iorio, A., Durante, O., Citro, R., Sanz-Fernández, C., Guarcello, C., Tokatly, I. V., Braggio, A., Rocci, M., Ligato, N., et al. (2020). A josephson phase battery. Nat. Nanotech., 15(8):656–660.

[152] Stratton, J. (1941). Diffraction of a plane wave by a sphere. Stratton, JA: Electromagnetic theory, New York, McGraw-Hill Book Co, page 563.

[153] Takahashi, S. and Maekawa, S. (2003). Spin injection and detection in magnetic nanostructures. Phys. Rev. B, 67:052409.

[154] Thomas, L. H. (1926). The motion of the spinning electron. Nature, 117(2945):514–514.

[155] Tokatly, I. V. (2008). Equilibrium spin currents: Non-abelian gauge invariance and color diamagnetism in condensed matter. Phys. Rev. Lett., 101:106601.

[156] Tokatly, I. V. (2017). Usadel equation in the presence of intrinsic spin-orbit coupling: A unified theory of magnetoelectric effects in normal and superconducting systems. Phys. Rev. B, 96(6):060502.

[157] Tsai, H., Karube, S., Kondou, K., Yamaguchi, N., Ishii, F., and Otani, Y. (2018). Clear variation of spin splitting by changing electron distribution at non-magnetic metal/bi 2 o 3 interfaces. Scient. Rep., 8(1):1–8.

[158] Tsai, H., Kondou, K., and Otani, Y. (2019). Enhanced spin-to-charge current conversion at metal/oxide interfaces by lowering the temperature. Japanese J. Appl. Phys., 58(11):110907.

[159] Tserkovnyak, Y., Halperin, B. I., Kovalev, A. A., and Brataas, A. (2007). Boundary spin hall effect in a two-dimensional semiconductor system with rashba spin-orbit coupling. Phys. Rev. B, 76:085319.

[160] Tsymbal, E. Y. and Zutic, I. (2011). Handbook of spin transport and magnetism. CRC press.

[161] Uhlenbeck, G. E. and Goudsmit, S. (1925). Ersetzung der hypothese vom unmechanischen zwang durch eine forderung bezüglich des inneren verhaltens jedes einzelnen elektrons. Naturwissenschaften, 13(47):953–954.

[162] Valenzuela, S. O. and Tinkham, M. (2006). Direct electronic measurement of the spin hall effect. Nature, 442(7099):176.

[163] van de Groep, J. and Polman, A. (2013). Designing dielectric resonators on substrates: Combining magnetic and electric resonances. Opt. Express, 21(22):26285–26302.

[164] Vas'ko, F. (1979). Spin splitting in the spectrum of two-dimensional electrons due to the surface potential. JETP Lett, 30(9):541–544.

[165] Vaz, D. C., Noël, P., Johansson, A., Göbel, B., Bruno, F. Y., Singh, G., Mckeown-Walker, S., Trier, F., Vicente-Arche, L. M., Sander, A., et al. (2019). Mapping spin–charge conversion to the band structure in a topological oxide two-dimensional electron gas. Nat. Mater., 18(11):1187–1193.

[166] Vignale, G. (2010). Ten years of spin hall effect. J. Supercon. Nov. Magnet., 23(1):3–10.

[167] Villamor, E., Isasa, M., Hueso, L. E., and Casanova, F. (2013). Contribution of defects to the spin relaxation in copper nanowires. Phys. Rev. B, 87:094417.

[168] Volke-Sepulveda, K., Garcés-Chávez, V., Chávez-Cerda, S., Arlt, J., and Dholakia, K. (2002). Orbital angular momentum of a high-order bessel light beam. J. Opt. B, 4(2):S82–S89.

[169] Wang, J., Yang, J.-Y., Fazal, I. M., Ahmed, N., Yan, Y., Huang, H., Ren, Y., Yue, Y., Dolinar, S., Tur, M., et al. (2012). Terabit free-space data transmission employing orbital angular momentum multiplexing. Nat. Photonics, 6(7):488–496.

[170] Wu, M., Jiang, J., and Weng, M. (2010). Spin dynamics in semiconductors. Physics Reports, 493(2):61 – 236.

[171] Yafet, Y. (1963). Sol. Stat. Phys., volume 14. Academic Press.

[172] Yao, A. M. and Padgett, M. J. (2011). Orbital angular momentum: origins, behavior and applications. Adv. Opt. Photon., 3(2):161–204.

[173] Yurkin, M. and Hoekstra, A. (2007). The discrete dipole approximation: An overview and recent developments. J. of Quant. Spectros. and Rad. Transfer, 106(1):558 – 589. IX Conference on Electromagnetic and Light Scattering by Non-Spherical Particles.

[174] Zambrana-Puyalto, X. and Bonod, N. (2016). Tailoring the chirality of light emission with spherical si-based antennas. Nanoscale, 8:10441–10452.

[175] Zambrana-Puyalto, X., Fernandez-Corbaton, I., Juan, M. L., Vidal, X., and Molina-Terriza, G. (2013). Duality symmetry and kerker conditions. Opt. Lett., 38(11):1857–1859.

[176] Zhang, W., Jungfleisch, M. B., Jiang, W., Pearson, J. E., and Hoffmann, A. (2015). Spin pumping and inverse rashba-edelstein effect in nife/ag/bi and nife/ag/sb. J. Appl. Phys., 117(17):17C727.

[177] Zutić, I., Fabian, J., and Sarma, S. D. (2004). Rev. Mod. Phys., 76:323.